Numerical simulations of microphysical processes in pyro-convective clouds

Dissertation
zur Erlangung des Grades
"Doktor der Naturwissenschaften"

am Fachbereich Physik
der Johannes Gutenberg-Universität
in Mainz

Philipp Reutter

geboren in
Stuttgart

Tag der mündlichen Prüfung: Freitag, 13. November 2009

Well my house is on fire
Burning to the sky
I thought it would rain
But the clouds passed by

Bob Dylan

Abstract

Deep convection induced by vegetation fires is one of the most intense forms of atmospheric convection. The extreme cloud dynamics with high updraft velocities (up to $20\,\mathrm{m\,s^{-1}}$) already at the cloud base, high water vapor supersaturations (up to 1%), and high number concentrations of aerosol particles freshly emitted by the fire (up to $1 \cdot 10^5\,\mathrm{cm^{-3}}$) represent a particular setting for aerosol-cloud interactions.

A crucial step in the microphysical evolution of a convective cloud is the activation of aerosol particles to form cloud droplets. The activation process affects the initial number and size of cloud droplets, and can thus influence the evolution of the convective cloud and the formation of precipitation. The main parameters determining the initial number and size of cloud droplets are the number, size and hygroscopicity of aerosol particles available at the cloud base as well as the updraft velocity. To investigate the influence of these parameters under the conditions of pyro-convection, numerical simulations have been performed using a cloud parcel model with a detailed spectral description of cloud microphysics, including different Köhler model approaches for hygroscopic growth. The results can be classified into three regimes depending on the ratio between updraft velocity and aerosol number concentration (w/N_{CN}): (1) an aerosol-limited regime (high w/N_{CN}), (2) an updraft-limited regime (low w/N_{CN}) and (3) a transitional regime (intermediate w/N_{CN}). The results suggest that the variability in the initial cloud droplet number concentration in (pyro-) convective clouds is mostly dominated by the variability of updraft velocity and aerosol particle number concentration.

To investigate the microphysical processes within the smoky updraft region of a pyro-convective cloud with detailed spectral microphysics, the parcel model was initialized along a trajectory within the convective updraft as obtained from a 3-dimensional simulation of an idealized pyro-convective event with the model ATHAM. It is shown that the cloud droplet number concentration increases with increasing aerosol number concentration. On the other hand, the size of the cloud droplets decreases with increas-

ing aerosol concentration. This reduced broadening of the spectrum with increasing aerosol concentration is in agreement with measurements and supports the concept of suppression of rain formation in extremely polluted clouds.

Building upon a realistic parameterization of CCN activation derived from the parcel model activation study, ATHAM was used to investigate the dynamical and microphysical processes of pyro-convective clouds with 2- and 3-dimensional simulations. A state-of-the-art two-moment microphysical scheme has been implemented in order to study the influence of the aerosol concentration on the development of idealized pyro-convective clouds in US standard atmospheres for the mid-latitudes and the tropics. The results show that the aerosol concentration influences the formation of rain. For lower aerosol concentrations rain formation is rapidly formed by warm microphysical processes while for higher aerosol concentrations the ice phase is more important for the formation of rain. This leads to a delay of the onset of precipitation for more polluted atmospheres. It is also shown that the composition of the ice nuclei (IN) has a strong effect on the dynamical and microphysical structure of these clouds. For very efficient IN rain forms more rapidly. The investigation of the influence of the atmospheric background profile shows a small effect of meteorology on the sensitivity of the pyro-convective clouds on aerosol concentration. Compared to the mid-latitude US standard atmosphere the influence of the aerosol concentration is similar in a warmer and more humid atmosphere as represented by the tropical US standard atmosphere. Finally, it is shown that the amount of heat emitted by the fire has a significant impact upon the development and cloud top height of pyro-convective clouds.

In summary, this thesis investigated in detail the microphysics of pyro-convective clouds by performing idealized simulations of fire-induced deep convection with a bin-microphysical parcel model and with a 3D model with a two-moment bulk scheme. It is clearly shown that the extreme conditions in terms of updraft velocity and aerosol concentrations significantly impact upon cloud evolution, including activation at the cloud base and in particular rain formation within the clouds. Similar model studies for more realistic conditions both in the tropics and extratropics will be required to further quantify the relevance of the findings for pyro-convection in the real atmosphere.

Zusammenfassung

Hochreichende Konvektion über Waldbränden ist eine der intensivsten Formen von atmosphärischer Konvektion. Die extreme Wolkendynamik mit hohen vertikalen Windgeschwindigkeiten (bis $20\,\mathrm{m\,s^{-1}}$) bereits an der Wolkenbasis, hohen Wasserdampfübersättigungen (bis $1\,\%$) und die durch das Feuer hohen Anzahlkonzentration von Aerosolpartikeln (bis $1 \cdot 10^5\,\mathrm{cm^{-3}}$) bilden einen besonderen Rahmen für Aerosol-Wolken Wechselwirkungen.

Ein entscheidender Schritt in der mikrophysikalischen Entwicklung einer konvektiven Wolke ist die Aktivierung von Aerosolpartikeln zu Wolkentropfen. Dieser Aktivierungsprozess bestimmt die anfängliche Anzahl und Größe der Wolkentropfen und kann daher die Entwicklung einer konvektiven Wolke und deren Niederschlagsbildung beeinflussen. Die wichtigsten Faktoren, welche die anfängliche Anzahl und Größe der Wolkentropfen bestimmen, sind die Größe und Hygroskopizität der an der Wolkenbasis verfügbaren Aerosolpartikel sowie die vertikale Windgeschwindigkeit. Um den Einfluss dieser Faktoren unter pyro-konvektiven Bedingungen zu untersuchen, wurden numerische Simulationen mit Hilfe eines Wolkenpaketmodells mit detaillierter spektraler Beschreibung der Wolkenmikrophysik durchgeführt. Diese Ergebnisse können in drei unterschiedliche Bereiche abhängig vom Verhältnis zwischen vertikaler Windgeschwindigkeit und Aerosolanzahlkonzentration (w/N_{CN}) eingeteilt werden: (1) ein durch die Aerosolkonzentration limitierter Bereich (hohes w/N_{CN}), (2) ein durch die vertikale Windgeschwindigkeit limitierter Bereich (niedriges w/N_{CN}) und (3) ein Übergangsbereich (mittleres w/N_{CN}). Die Ergebnisse zeigen, dass die Variabilität der anfänglichen Anzahlkonzentration der Wolkentropfen in (pyro-) konvektiven Wolken hauptsächlich durch die Variabilität der vertikalen Windgeschwindigkeit und der Aerosolkonzentration bestimmt wird.

Um die mikrophysikalischen Prozesse innerhalb der rauchigen Aufwindregion einer pyro-konvektiven Wolke mit einer detaillierten spektralen Mikrophysik zu untersuchen, wurde das Paketmodel entlang einer Trajektorie innerhalb der Aufwindregion ini-

tialisiert. Diese Trajektore wurde durch dreidimensionale Simulationen eines pyro-konvektiven Ereignisses durch das Model ATHAM berechnet. Es zeigt sich, dass die Anzahlkonzentration der Wolkentropfen mit steigender Aerosolkonzentration ansteigt. Auf der anderen Seite verringert sich die Größe der Wolkentropfen mit steigender Aerosolkonzentration. Diese Reduzierung der Verbreiterung des Tropfenspektrums stimmt mit den Ergebnissen aus Messungen überein und unterstützt das Konzept der Unterdrückung von Niederschlag in stark verschmutzten Wolken.

Mit Hilfe des numerischen Models ATHAM wurden die dynamischen und mikrophysikalischen Prozesse von pyro-konvektiven Wolken, aufbauend auf einer realistischen Parametrisierung der Aktivierung von Aerosolpartikeln durch die Ergebnisse der Aktivierungsstudie, mit zwei- und dreidimensionalen Simulationen untersucht. Ein modernes zweimomenten mikrophysikalisches Schema wurde in ATHAM implementiert, um den Einfluss der Anzahlkonzentration von Aerosolpartikeln auf die Entwicklung von idealisierten pyro-konvektiven Wolken in US Standardamtosphären für die mittleren Breiten und den Tropen zu untersuchen. Die Ergebnisse zeigen, dass die Anzahlkonzentration der Aerosolpartikel die Bildung von Regen beeinflusst. Für geringe Aerosolkonzentrationen findet die rasche Regenbildung hauptsächlich durch warme mikrophysikalische Prozesse statt. Mit höheren Aerosolkonzentrationen wird die Eisphase wichtiger für die Bildung von Regen. Dies führt zu einem verspäteten Einsetzen von Niederschlag für verunreinigtere Atmosphären. Außerdem wird gezeigt, dass die Zusammensetzung der Eisnukleationspartikel (IN) einen starken Einfluss auf die dynamische und mikrophysikalische Struktur solcher Wolken hat. Bei sehr effizienten IN bildet sich Regen früher. Die Untersuchung zum Einfluss des atmosphärischen Hintergrundprofils zeigt eine ähnliche Auswirkung der Meteorologie auf die Sensitivität der pyro-konvektiven Wolken auf die Aerosolkonzentration. Zum Abschluss wird gezeigt, dass die durch das Feuer emittierte Hitze einen deutlichen Einfluss auf die Entwicklung und die Wolkenobergrenze von pyro-konvektive Wolken hat.

Zusammenfassend kann gesagt werden, dass in dieser Dissertation die Mikrophysik von pyro-konvektiven Wolken mit Hilfe von idealisierten Simulation eines Wolkenpaketmodell mit detaillierter spektraler Mikrophysik und eines 3D Modells mit einem zweimomenten Schema im Detail untersucht wurde. Es wird gezeigt, dass die extremen Bedingungen im Bezug auf die vertikale Windgeschwindigkeiten und Aerosolkonzentrationen einen deutlichen Einfluss auf die Entwicklung von pyro-konvektiven Wolken haben.

Contents

Chapter 1

Introduction

Clouds cover about 60% of the Earth's surface and have a strong influence on the global radiative balance, water cycle and climate (IAPSAG (2007), Solomon et al. (2007)). Deep convective clouds play an important role in the vertical redistribution of energy and moisture, especially in the tropics (Wang (2003); Jiang et al. (2004)). At mid-latitudes, deep convection is often associated with heavy rain events and severe weather. Hence, modifications of convective cloud properties can affect weather and climate on local and global scales (Rosenfeld (2006)). A crucial factor for the dynamical and microphysical evolution of clouds is the activation of aerosol particles as cloud condensation nuclei (CCN), i.e., their hygroscopic growth into aqueous droplets that can freely grow by condensation of water vapor. Enhancing the number of aerosol particles that can serve as CCN generally leads to more and smaller cloud droplets at cloud base. It is well established that for shallow clouds, the precipitation efficiency is reduced when the aerosol concentration increases (e.g. Rosenfeld and Woodley (2000), Penner et al. (2004), Andreae and Rosenfeld (2008)). For deep convective clouds, the consequences of enhanced aerosol concentration are nonlinear and depend strongly on meteorological parameters (e.g. Khain et al. (2008); Rosenfeld et al. (2008)).

Transport through deep convective clouds has been identified as a relevant source for upper tropospheric/lower stratospheric (UT/LS) aerosol (e.g. Andreae et al. (2001), Wang (2003), Luderer et al. (2006)). The number of aerosol particles released into the UT/LS region depends on the number of activated aerosol particles and on the microphysical evolution of deep convective clouds (nucleation and precipitation scavenging), which, in turn, is also modified by aerosol activation at cloud base. Pyro-convection, i.e., deep convective clouds that form above wildfires, is one of the most extreme forms of atmospheric deep convection. Observational and modeling studies have shown the

Figure 1.1: *Picture of a pyro-cumulus cloud forming over a deforestation fire in Brazil during the SMOCC campaign in 2002. Picture taken by M. Welling, MPI Mainz.*

extraordinary dynamical and microphysical properties of deep pyro-clouds (e.g. Fromm and Servranckx (2003), Fromm et al. (2005), Trentmann et al. (2006), Rosenfeld et al. (2007)) and their ability to transport substantial amounts of aerosol into the UT/LS (Fromm et al. (2005), Luderer et al. (2006)). However, the relevant processes in pyro-clouds, including CCN activation at the cloud base, are not yet fully characterized and understood.

1.1 Pyro-convective clouds

After the Glossary of Meteorology of the American Meteorological Society a pyro-cumulus cloud is a cloud formed by a rising thermal from a fire, or enhanced by buoyant

plume emissions from an industrial combustion process[1]. Other reasons for such clouds are volcanic eruptions or the detonation of a nuclear weapon.

Since the focus of this thesis is on pyro-cumulus clouds that form over active fires, these clouds can occur anywhere in the world with sufficient vegetation to produce enough heat for an air parcel to rise. During the ascent of an air parcel and the related expansion and cooling condensation starts and a cumulus cloud is forming. One of the first observations of a pyro-cumulus cloud was described by Ward (1898):

An interesting observation of the formation of small cumulus clouds over a fire was made by the writer on October 29 last, at the southern station of the Harvard College Observatory, at Arequipa, Peru (altitude 8,060 feet above sea level). At about 3:45 p.m. on that day there was observed behind the western flank of Mount Charchani (20,000 feet above sea level), and about 15 miles or so away, a column of smoke rising from a considerable fire of brushwood behind the mountain. The altitude above sea level of the fire was about 14,000 feet, judging by its relation to the height of the mountain. As the writer was looking at the smoke, which was rising to a considerable height, he noticed the formation of a small cumulus cloud directly over the smoke column, and approximately at a height of 17,000 or 18,000 feet above sea level, or 3,000 to 4,000 feet above the fire. The sky at this time was clear, except a trace of cirrus in the west and southwest. The wind at Arequipa was west about 16 miles an hour. The cloud was only a fragment, and disappeared very soon, drifting to the southeast. It was succeeded by another small cumulus, which again disappeared within five minutes. The smoke column was ascending apparently near vertically, but its top was blown somewhat toward the southeast. Successive cloudlets, rather fracto-cumulus than true cumulus formed over the smoke, none of them lasting more than three minutes, and most of them only one minute. Eight distinct cloudlets were seen thus to form and dissolve within the space of half an hour, at the end of which time the smoke had disappeared. At Arequipa the wind, as stated above, was west 15 miles. Where the smoke was (14,000 feet) it was nearly calm. At the level of the cirro-cumulus clouds there was a strong current from west-northwest. Although the smoke column was small, evidently the conditions were favorable for cloud formation. The whole thing, however, was on a miniature scale [...]

Ward has described in an interesting way the main mechanism that drives a pyro-cumulus cloud. In this case, the emission of sensible heat by the fire produced an upward motion of air. This ascending air reached its condensation level, where the

[1] http://amsglossary.allenpress.com/glossary, 2009

small cumulus cloud starts to form. Assumedly, the atmospheric conditions inhibited the development of deep convective clouds, which is indicated by the statement, that the "*sky at this time was clear, except a trace of cirrus in the west and southwest*". Because of this stable atmosphere, the cumulus clouds could not develop further and existed only a couple of minutes.

As it was shown in Luderer et al. (2006) the background meteorology is the basic requirement to allow the formation of deep pyro-convective clouds, that can even intersect the tropopause in extreme cases. Note that the sensible heat release by the fire is important to initialize the convection, but usually a fire can not destabilize the complete overlaying atmosphere. Therefore, the height of pyro-convective clouds depend strongly on the background meteorology.

In the last decade the study of pyro-convective clouds and their impact on the climate by transport of smoke and other traces gases attracted more notice. For example Fromm et al. (2000) showed an increase of tropospheric and stratospheric aerosols during the fire season in 1998 in the northern hemisphere. Again, Fromm and Servranckx (2003), Rosenfeld et al. (2007) and Trentmann et al. (2006) reported the injection of tropospheric aerosols into the stratosphere in case studies of the Chisholm pyro-cumulonimbus. This aerosol plume was observed for several months well within the stratosphere. Also, for this case an extremely continental microphysical structure was documented, which lead to an efficient suppression of precipitation formation within the updraft region. Sensitivity studies by Luderer et al. (2006) showed that the sensible heat release by the fire is the most important parameter influencing the Chisholm pyro-cumulonimbus, which is also consistent with other studies (Penner et al. (1986) and Lavoué et al. (2000)). When more sensible heat is available the cloud is reaching higher altitudes, thereby condensing and freezing more of the available water and releasing additional latent heat, thus give rise to a positive feedback. The sensitivity of the Chisholm pyro-cloud on the aerosol concentration showed that the updraft region is only weakly affected by the aerosol loading which stays in contrast to the findings of other studies, which reported a stronger convection with increasing aerosol concentration (Andreae et al. (2004), Koren et al. (2005), Wang (2005)). The reported invigoration of deep convection with increasing aerosol concentration is explained by Andreae et al. (2004) and Koren et al. (2005) by a delay in the formation of precipitation and the suppression of downdrafts and warm rain. Therefore the convection reaches higher releasing more latent heat.

Several other case studies were presented over the last years describing fires in

Canada (Fromm et al. (2005)) and Australia (Fromm et al. (2006)). Further studies were dealing with the role of fire-released moisture on the dynamics of pyro-cumulus clouds. Luderer et al. (2009) reported that the moisture release by the fire is of much less importance for the pyro-convective cloud than the release of sensible heat. This is in contrast to Potter (2005), who stated that the moisture released by wildland fires can be a dominant contributor to the water budget and the convection dynamics of pyro-clouds.

Recently, Cunningham and Reeder (2009) presented numerical simulations of a pyro-convective cloud and pyro-tornadogenesis for an Australian fire. This work addressed the influence of the role played by the heat of combustion in the development of the convection and the importance of the water produced during combustion in deepening the convection. Their findings are consistent with the hypothesis and results of Potter (2005), but appear to contradict the numerical results by Luderer et al. (2009).

Recently, Cammas et al. (2009) reported of in-situ measurements of biomass fire plumes injected into the lower stratosphere.

However, the focus in this thesis is on the influence of aerosol concentration on the dynamical and microphysical evolution of pyro-convective clouds using different model approaches.

1.2 Impact of aerosols on clouds and climate

Aerosol particles affect the cloud properties and hence the climate in many different ways. The exact quantitative effect on the Earth's radiation budget has large uncertainties, which is one reason why it is so difficult to estimate climate evolution. Figure 1.2, taken from the 2007 IPCC report, shows this uncertainty in the understanding of the influence of aerosol particles on the radiative forcing. It can be seen that the overall radiative forcing of aerosol particles is negative.

In the following the different direct and indirect aerosol effects and their influence on climate are summarized. For a review of the global direct and indirect effects see Haywood and Boucher (2000) andLohmann and Feichter (2005), respectivly.

1. Direct aerosol effect:

   The direct aerosol effect takes into account that the aerosol particles scatter and absorb solar radiation. Also they can scatter, absorb and emit thermal radiation, which leads to a warming of the atmosphere.

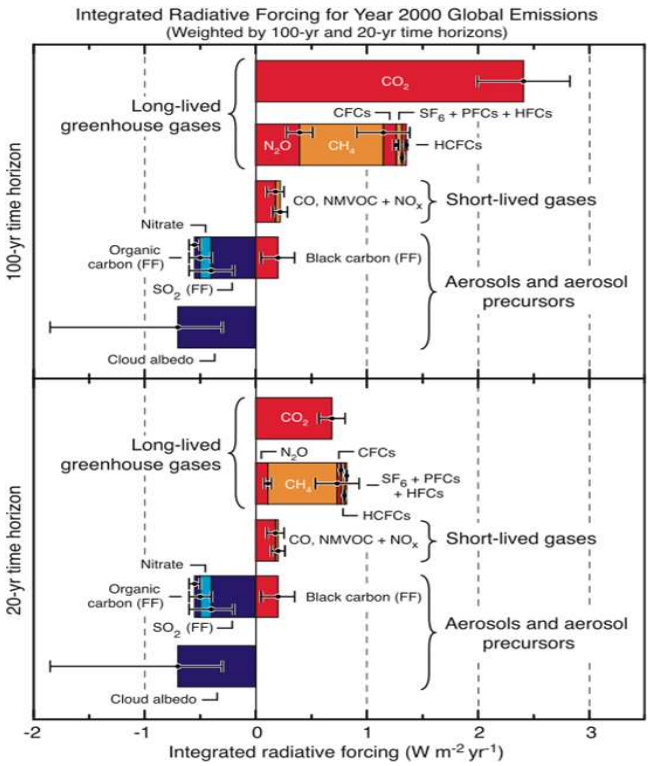

Figure 1.2: *Integrated radiative forcing of year 2000 emissions over two horizons, namely (top)* 100 *years and (bottom)* 20 *years based on numerous model simulations. The figure gives and indication of the future climate impact of current emissions. The values for aerosols and aerosol precursors are essentially equal for the two time horizons. The values given in the figure apply only to the global annual emissions. The thin black line attached to each colored bar represents the range of uncertainty for the respective value. Reddish colors denote a warming of the climate, bluish a cooling. From Solomon et al. (2007).*

2. Semi-direct effect:

   The absorption of solar radiation by tropospheric aerosols leads to heating of the troposphere, which changes the relative humidity and the stability of the troposphere. This has an influence on the cloud formation and lifetime (Johnson et al. (2004)).

3. Indirect aerosol effects:

   Higher number concentrations of CCN lead to more but smaller cloud droplets, which are reflecting more solar radiation. Such clouds will appear “whiter”. Also, the smaller cloud droplets are decreasing the precipitation efficiency and hence extending the cloud lifetime. Another effect is that the smaller cloud droplets delay the onset of freezing and therefore the release of latent heat, which has an

important effect on the dynamical evolution of clouds. On the other hand, the larger amount of ice nuclei is increasing the efficiency of freezing and therefore the precipitation efficiency.

1.3 Problem of different scales

The investigation of the influence of aerosol particles emitted by biomass burning on convective clouds involves a wide range of different length scales starting from around $1 \cdot 10^{-9}$ m (size of aerosol particles) to about $1 \cdot 10^{4}$ m (scale of convection). To study the aerosol-cloud interactions in full detail a numerical model would need to be extremely complex to capture all processes on all different length scales. Also the computational effort can be very high.

In the remaining of this section the main aspects of the CCN activation and convective clouds are presented.

1.3.1 CCN activation

The first step in the development of a cloud is the condensation of water vapor on particles, the so-called cloud condensation nuclei (CCN). This process is called heterogeneous nucleation whereas the term homogeneous nucleation denotes the process of the condensation of water vapor in pure air without any particles. The latter form of nucleation requires the formation of a very small droplet embryo consisting of only few water molecules. From theory it is known that the equilibrium vapor pressure over a curved surface is greater than over a flat surface, which is the so-called "Kelvin effect". For an extremely small droplet embryo the curvature is as large such that a supersaturation of up to $\sim 800\,\%$ is needed (Pruppacher and Klett (1997)).

In the atmosphere, such large supersaturations for nucleation are never reached because of the presence of aerosol particles, which are reducing the supersaturation required for the nucleation by the so-called "Raoult effect". This effect describes the fact, that the equilibrium water vapor pressure over a solution is lower than that over pure water. Hence, water vapor can condense on a soluble aerosol particle, because the Raoult effect opposes the Kelvin effect.

The "Köhler theory" describes the formation of cloud droplets including the Kelvin and Raoult effect based on the concept that every dry soluble particle size has its own "critical supersaturation" S_c. The corresponding "critical radius" r_{crit} denotes

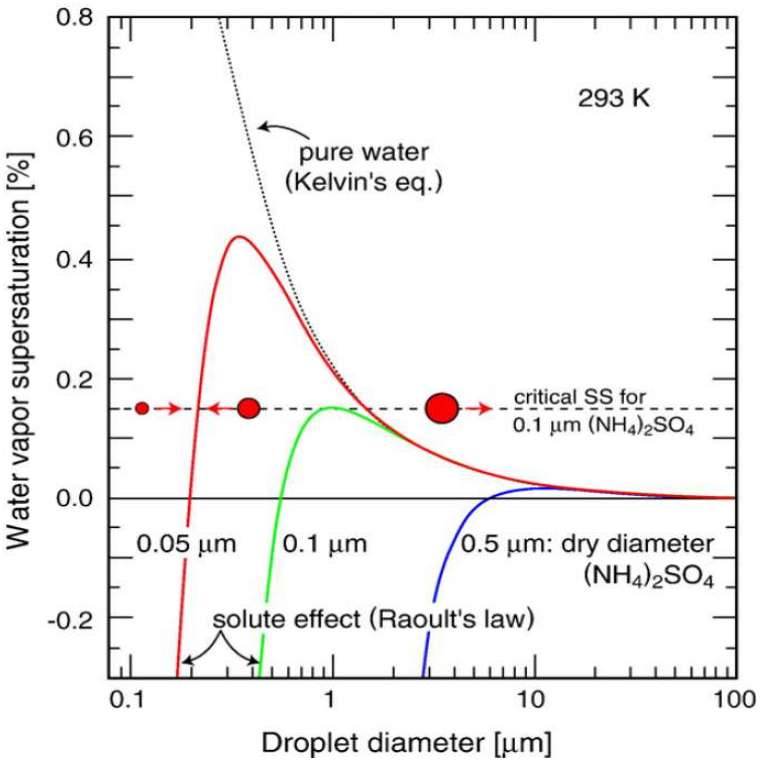

Figure 1.3: *Köhler curves showing the equilibrium water vapor supersaturations at 293 K for droplets of pure water (dotted curve) and for droplets containing various masses of dissolved* $(NH_4)_2SO_4$ *(solid curves) vs. diameter of the droplet (Seinfeld and Pandis (2006)). The water vapor supersaturation is defined as* $S(\%) = 100 \cdot (p/p_0 - 1)$*, where* p *is the partial pressure of the water vapor and* p_0 *is the saturated vapor pressure over a plane surface of water at this temperature. In the indicated example, an ambient water vapor supersaturation* s *of* $0.15\,\%$ *(dashed line) exceeds the critical value for all ammonium sulfate aerosols with dry diameter* $\geq 0.1\,\mu m$*. These aerosols will therefore activate and grow into cloud droplets, whereas smaller aerosols remain as unactivated haze particles. Droplets below their corresponding equilibrium curve will shrink by evaporation whereas those above will grow by condensation. From Andreae and Rosenfeld (2008).*

the size of a particle at which an infinitesimal small increase in the size will lead to a spontaneous growth into a cloud droplet (see Fig. 1.3). This growth is based on the fact, that the Kelvin effect decreases with increasing size of the droplet.

It can be concluded, that the critical supersaturation is decreasing with increasing particle size (Kelvin effect) or with increasing mass of soluble substances within the particle (Raoult effect).

The effect of increasing soluble mass on the critical supersaturation and radius can be seen in Fig. 1.4. Here the single hygroscopicity parameter description κ of Petters and Kreidenweis (2007) is used which is described in more detail in Chapter 2.2.2.

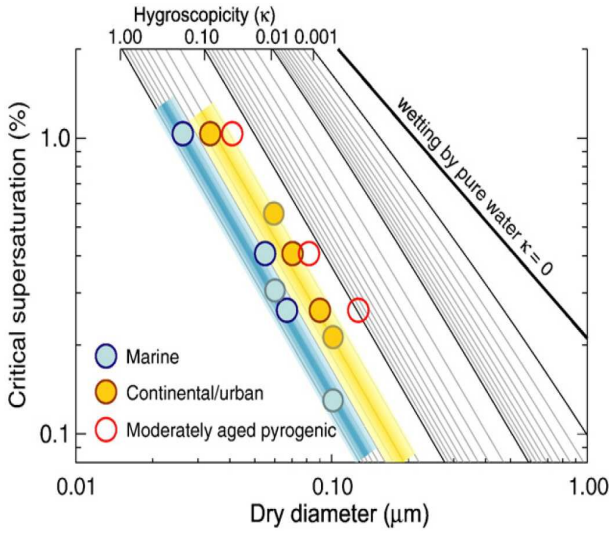

Figure 1.4: *Average relationships between aerosol dry diameter and critical supersaturation. The colored bands reflect polluted continental and clean marine data from Hudson (2007), the colored dots with colored borders are from Dusek (2006) and Andreae (unpublished data), and the colored dots with grey borders have been recalculated from Kandler and Schütz (2007). The lines of constant hygroscopicity, κ, are from Petters and Kreidenweis (2007). From Andreae and Rosenfeld (2008).*

According to this concept highly soluble particles like sodium chloride have κ values of around 1.3 and totally insoluble particles have a value of zero. Figure 1.4 shows that for higher κ values a given critical supersaturation, e.g. 1.0 %, is reached for smaller particles compared to more hydrophobic particles (low κ values).

1.3.2 Deep Convection

Deep convective clouds are an important mechanism for the vertical transport of moisture, trace gases and energy. In the Earth's atmosphere various forms of deep convection can be found:

- single cell convection, which usually consist of a single updraft and downdraft region and form under unstable conditions with a weak vertical wind shear;
- multicell storms, that form at atmospheric conditions with a moderate vertical wind shear. These storms consist of several interacting single cells;
- supercell storms consist of a single cell with a rotating updraft region, which can exist over a longer period than an ordinary single cell convection. Their formation requires large ambient wind shear.

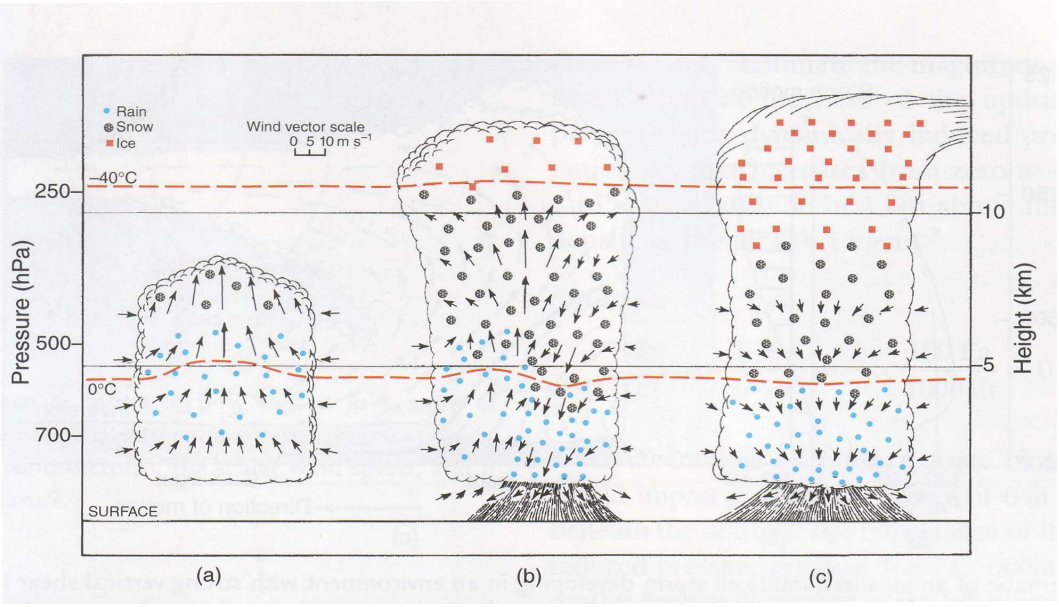

Figure 1.5: *Schematic of a typical single cell thunderstorm in three stages of its life cycle showing (a) cumulus stage, (b) mature stage, and (c) dissipating stage. The horizontal scale is compressed by about 30 % relative to the vertical scale in the figure. The* $0\,^{\circ}\mathrm{C}$ *and* $-40\,^{\circ}\mathrm{C}$ *isotherms are indicated in red. From Wallace and Hobbs (2006).*

The focus of this thesis is on single cell convection, which is induced by the sensible heat release of a biomass burning event. The different life cycles of a single convective cloud can be divided into three stages: the cumulus, mature and dissipating stage (see Fig. 1.5).

The cumulus stage is characterized by a warm, buoyant plume of rising air. In this early stage the cloud consists only of cloud and rain droplets, which may be supercooled. Because of the strong increase of the updraft velocity within the cloud, the cloud top rises up with a velocity of up to $10\,\mathrm{m\,s^{-1}}$. This also leads to a considerable entrainment through the lateral boundaries of the cloud.

In the mature stage of the deep convective cloud a vigorous downdraft circulation is formed, which coincides with the region of heaviest rain. This downward circulation is formed by the falling rain droplets, which evaporate below the cloud and in regions where unsaturated air is entrained into the cloud. The evaporation leads to a cooling of air and hence to a negative buoyancy of the downdraft air. On the other side, the cloud top is reaching the tropopause and starts to spread out horizontally and forms an anvil. In this stage, snowflakes and ice droplets forme and can be found even below the freezing level due to the strong downdrafts.

In the dissipating stage the downward circulation becomes more extensive by the precipitation until it covers most parts of the cloud. In this stage, cloud droplets can no longer grow because of the absence of supersaturated air created by an upward motion. As a consequence, the cloud is evaporating into the ambient air, while only parts of the anvil are left behind as a cirrus cloud.

1.4 Aims of this study

This study deals with the multi-scale problem of the influence of the high number concentration of CCN on the dynamical and microphysical evolution of deep convective clouds, which are induced by the sensible heat release of a biomass burning event.

For the best possible description of this multi-scale problem this thesis is divided into three parts. In Chapter 2 the activation of aerosol particles to cloud droplets at the cloud base for a wide range of constant updraft velocities ($w = 0.25 - 20\,\mathrm{m\,s^{-1}}$) and aerosol particle number concentration ($N_{CN} = 200 - 10^5\,\mathrm{cm^{-3}}$) is investigated with the detailed spectral microphysics of a parcel model. The knowledge of the exact number concentration of cloud droplets at the cloud base is very important for the further simulations of microphysical processes within pyro-convective clouds.

In a next step, the development of the microphysical properties within the updraft region of a pyro-convective cloud are studied in Chapter 3. Therefore a new model approach is introduced where the parcel model with detailed spectral microphysics from Chapter 2 is run along an ascending trajectory derived from 3D simulations of pyro-convective clouds. With this technique the processes within this updraft region characterized by high vertical velocities and high aerosol concentrations can be evaluated.

In Chapter 4 the results from the activation study in Chapter 2 are used for 2D and 3D simulations of idealized biomass burning events in the mid-latitudes and tropics. Sensitivity studies concerning the influence of the aerosol number concentration, ice nucleation ability, fire forcing and atmospheric profiles on the dynamical and microphysical evolution of pyro-convective clouds are conducted. These results, obtained with a realistic activation of cloud droplets, increase the understanding of the important mechanism for the evolution of pyro-convective clouds.

Chapter 2

Influence of particle number, size and hygroscopicity on the activation of cloud condensation nuclei (CCN)[1]

2.1 Introduction

The main parameters governing CCN activation and initial cloud droplet growth are the number, size and hygroscopicity of aerosol particles as well as the updraft velocity at the cloud base and the resulting water vapor supersaturation. In most earlier studies of cloud droplet formation, the number concentration of aerosol particles did not exceed $10^4\,\mathrm{cm}^{-3}$ (e.g. Hjelmfelt et al. (1978); Hegg (1999); Nenes et al. (2001); Lance et al. (2004); Ervens et al. (2005); Segal and Khain (2006); Kivekas et al. (2008); Cubison et al. (2008); Altaratz et al. (2008)). This is realistic for regions with low or moderate air pollution, but in biomass burning plumes the aerosol number concentration can reach up to $\sim 10^5\,\mathrm{cm}^{-3}$ (Andreae et al. (2004); Reid et al. (2005)).

To investigate and characterize the process of CCN activation in (pyro-)convective clouds, cloud parcel model simulations for a wide range of conditions, including the high updraft velocities and aerosol particle number concentrations observed over wildfires

[1]This Chapter is based on the manuscript "Aerosol- and updraft-limited regimes of cloud droplet formation: influence of particle number, size and hygroscopicity on the activation of cloud condensation nuclei (CCN)" by P. Reutter, J. Trentmann, H. Su, M. Simmel, D. Rose, S. S. Gunthe, H. Wernli, M. O. Andreae and U. Pöschl, published in Atmospheric Chemistry and Physics (Reutter et al. (2009))

($0.5 - 20\,\mathrm{m\,s^{-1}}$, 10^3 $-10^5\,\mathrm{cm^{-3}}$) have been performed. Moreover, the κ-Köhler model approach as an efficient and realistic new way of describing the CCN activity of aerosol particles with complex chemical composition as emitted from biomass burning (Petters and Kreidenweis (2007); Pöschl et al. (2009)), rather than using unrealistic surrogates species like sodium chloride (e.g., Segal and Khain (2006)), have been implemented and tested. In Section 2.2 the applied cloud parcel and Köhler models (hygroscopicity parameter and osmotic coefficient formalisms) is decscribed, and the results of test calculations performed for comparison and validation against an alternative cloud parcel model with spectral microphysics (Segal and Khain (2006)) are presented. In Section 2.3 the results of model calculations exploring the dependence of cloud droplet number concentration on updraft velocity and aerosol particle number concentration as well as particle size and hygroscopicity are presented and discussed.

2.2 Methods

2.2.1 Model description

The cloud parcel model used in this study has been developed by Simmel et al. (2002) and contains a detailed spectral description of cloud microphysics (Simmel and Wurzler (2006), Diehl et al. (2006), Diehl et al. (2007)). Based on a given dry aerosol size distribution, the model initially calculates the equilibrium aerosol size distribution at the relative humidity prescribed for the simulation start. As the air parcel rises with a prescribed vertical velocity, the model simulates the expansion and cooling of air as well as the resulting changes in relative humidity and the related hygroscopic growth of aerosol particles and further condensational growth of cloud droplets. Collision-coalescence and entrainment processes were not included in this simulations which are focused on CCN activation and initial growth of cloud droplets at the cloud base. Model test runs including collision-coalescence showed that coagulation can indeed be neglected at the early stages of cloud evolution investigated in this study (relative deviations $\leq 1\,\%$).

Particle growth rates were calculated according to the following equation (Pruppacher and Klett (1997), Simmel and Wurzler (2006)):

$$\frac{\mathrm{d}m}{\mathrm{d}t} = \frac{4\pi r(s_\infty - s_{eq})}{\frac{L_v}{R_v T} - 1\frac{L_v}{K^* T} + \frac{R_v T}{e_{s,w}(T) D^*}} \tag{2.1}$$

m is the particle mass, t the simulation time, L_v the latent heat of condensation ($2.50078 \cdot 10^6 \mathrm{J\,kg^{-1}}$), R_v the gas constant for water vapor ($461.5 \mathrm{J\,kg^{-1}\,K^{-1}}$), K^* the modified thermal conductivity of air ($\mathrm{W\,m^{-1}\,K^{-1}}$), $e_{s,w}$ the saturation water vapor pressure, D^* the modified diffusion coefficient for water vapor in air ($\mathrm{m^2\,s^{-1}}$), s_∞ the saturation ratio of the surrounding air and s_{eq} the equilibrium water vapor saturation ratio at the particle/air interface. For more details and parameterizations of K^* and D^* see Simmel and Wurzler (2006).

Both aerosol particle and cloud droplet size and growth are described on a common spectral grid. The simulations presented here were carried out using 264 logarithmically equidistant bins between 1 nm and 3.5 mm and a time step of $\mathrm{d}t = 0.01\,\mathrm{s}$. The weighting coefficient for the redistribution of mass between the size bins after each time step was set to $a = 0.6$ (Simmel and Wurzler (2006)). The prognostic parameters include liquid water mass and particle number for each size bin.

The input parameters required to initialize the simulations are: (1) the initial meteorological conditions (temperature, pressure, relative humidity); (2) the updraft velocity of the air parcel; (3) the dry aerosol particle number size distribution; and (4) a set of parameters characterizing the hygroscopicity of the particle material according to Köhler theory (effective hygroscopicity parameter,κ, or a combination of stoichiometric dissociation coefficient and osmotic coefficient, $\nu_s \Phi_s$; see Sect. 2.2.2).

All model simulations were initialized with a temperature of 285.20 K, a pressure of 950 hPa, and a relative humidity of 95 % (Simmel and Wurzler (2006)). They were carried through with a constant vertical velocity w, and stopped upon reaching a liquid water content (LWC) of $0.8\,\mathrm{g\,kg^{-1}}$. In different runs the vertical velocity w, initial aerosol particle number concentration N_{CN}, size distribution, and hygroscopicity parameter were varied as detailed below.

The highest value of the water vapor supersaturations calculated in the course of each simulation ($S = (s_\infty - 1) \cdot 100\,\%$) was reported as the maximum supersaturation S_{max} (for an exemplary profile of S see Fig. 2.1). The cloud droplet number concentrations N_{CD} and activated particle fractions N_{CD}/N_{CN} reported below were determined from the model at the end of the simulation. Particles were counted as cloud droplets when the diameter is equal or larger than the critical droplet diameter corresponding to the water vapor saturation ratio in the modeled air parcel ($s = 1 + S/(100\,\%)$) of each parcel model run (Seinfeld and Pandis (2006), $D_{wet,c} = \frac{2A}{3\,ln\,s_c}$ with $A = \frac{4\sigma_{sol} M_w}{RT\,\rho_w}$ using $s_c = s$, $D_{wet,c}$ is the critical droplet diameter, s_c is the critical water vapor supersaturation ratio, σ_{sol} is the surface tension of solution droplet, M_w is the molar mass

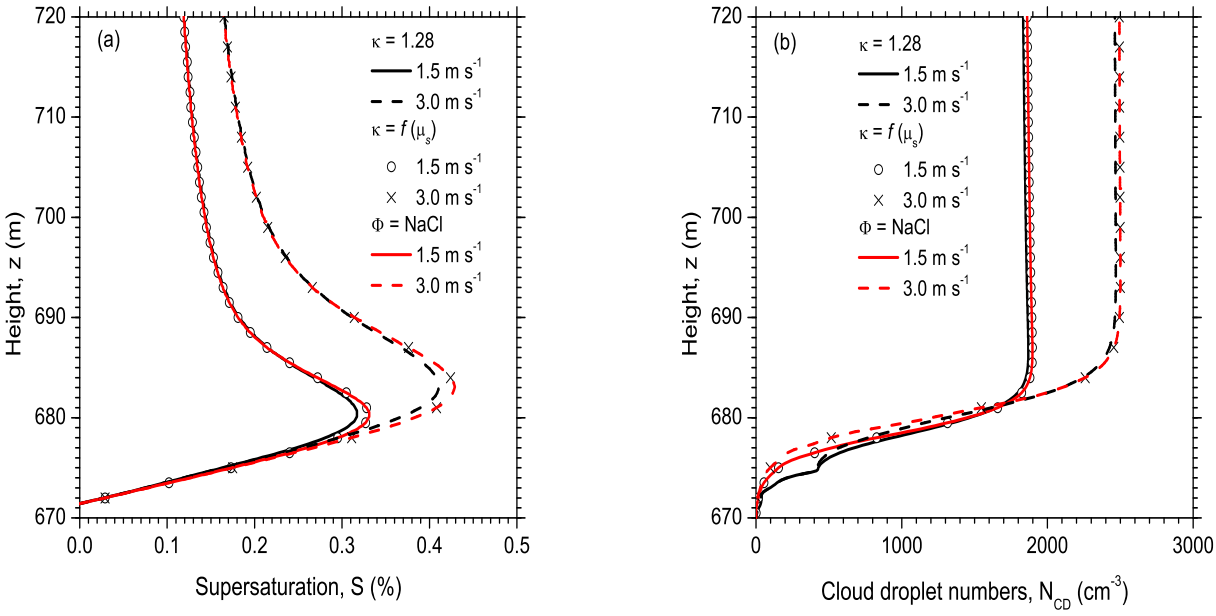

Figure 2.1: *Exemplary vertical profiles of (a) water vapor supersaturation (S, %) and (b) cloud droplet number concentration (N_{CD}, cm^{-3}) simulated with different Köhler model approaches: osmotic coefficient model (red lines), κ-Köhler model with constant κ (black lines) and κ- Köhler model with μ_s dependent κ (open circle and cross). The updraft velocity was set to $w = 1.5\,\mathrm{m\,s}^{-1}$ (solid lines or open circle) or $w = 3.0\,\mathrm{m\,s}^{-1}$ (dashed lines or cross), and the initial aerosol particle number concentration was set to $N_{CN} = 3,000\,\mathrm{cm}^{-3}$ with particle properties as specified by Segal and Khain (2006).*

of water and ρ_w is the density of pure water). Under the model conditions investigated in this study (constant updraft, no entrainment, no coagulation), the results are the same when using the maximum value or the final value of supersaturation for the calculation of $D_{wet,c}$. Different approaches of cloud droplet counting are required and will be discussed in follow-up studies including coagulation, entrainment and variable updraft velocities.

2.2.2 Köhler models

According to Köhler theory, the equilibrium water vapor saturation ratio s_{eq} is given by

$$s_{eq} = a_w \cdot Ke \tag{2.2}$$

where a_w denotes the water activity or Raoult term, and Ke is the Kelvin term. In this study two different approaches have been tested of describing the influence of aerosol

chemical composition and hygroscopicity on : an effective hygroscopicity parameter (κ) Köhler model (Petters and Kreidenweis (2007), Kreidenweis et al. (2009), Pöschl et al. (2009)) and an osmotic coefficient (OS) reference model which is more accurate but also more complex as detailed by Rose et al. (2008a). In the OS Köhler model, a_w is given by

$$a_w = \exp(-\nu_s \Phi_s \mu_s M_w) \tag{2.3}$$

where ν_s, Φ_s and μ_s are the stoichiometric dissociation number, osmotic coefficient and molality of the aerosol particle material (solute), respectively, and M_w is the molar mass of water. In the test simulations for sodium chloride particles (Sect. 2.2.3),$\nu_s = 2$ and the parameterization of Pitzer and Mayorga (1973) for Φ_s (OS1 model of Rose et al. (2008a)) have been used.

In the κ-Köhler model a_w is given by

$$a_w = \left(1 + \kappa \frac{V_s}{V_w}\right)^{-1} \tag{2.4}$$

where κ and V_s are the effective hygroscopicity parameter and the volume of dry particulate matter ($V_s = \frac{4}{3}\pi r_s^3$, with r_s the radius of the particles), and V_w is the volume of water in the aqueous particle/droplet ($V_w = \frac{4}{3}\pi r_w^3$, with r_w the radius of the wet fraction). Characteristic values of κ are 0 for completely insoluble particles, 0.6 for $(NH_4)_2SO_4$ and 1.28 for NaCl (Petters and Kreidenweis (2007); Rose et al. (2008a)). The hygroscopicity parameters of biomass burning aerosols range from 0.01 for freshly emitted smoke containing mostly soot particles to 0.55 for aerosol from grass burning, and the average value of κ in polluted continental air is 0.3 ± 0.1 (Andreae and Rosenfeld (2008); Rose et al. (2008b); Pöschl et al. (2009)).

In test simulations for sodium chloride particles (Sect. 2.2.3), $\kappa = 1.28$ and $\rho_s = 2165\,\mathrm{kg\,m^{-3}}$ (EH1 model of Rose et al. (2008a)) have been used. For the simulation of real atmospheric aerosols (rural and biomass burning) $\kappa = 0.2$ and $\rho_s = 1300\,\mathrm{kg\,m^{-3}}$ have been used. The Kelvin term was described by

$$Ke = \exp\left(\frac{2\sigma}{R_v T \rho_w r_{wet}}\right) \tag{2.5}$$

where σ and r_w are the surface tension and radius of the aqueous particle/droplet respectively. $R_v = 461.5\,\mathrm{J\,kg^{-1}\,K^{-1}}$ and $\rho_w = 1000\,\mathrm{kg\,m^{-3}}$ are the specific gas constant and density of water and T is the temperature. In the test simulations for sodium chloride particles (Sect. 2.2.3) using the OS Köhler model, σ was calculated by a

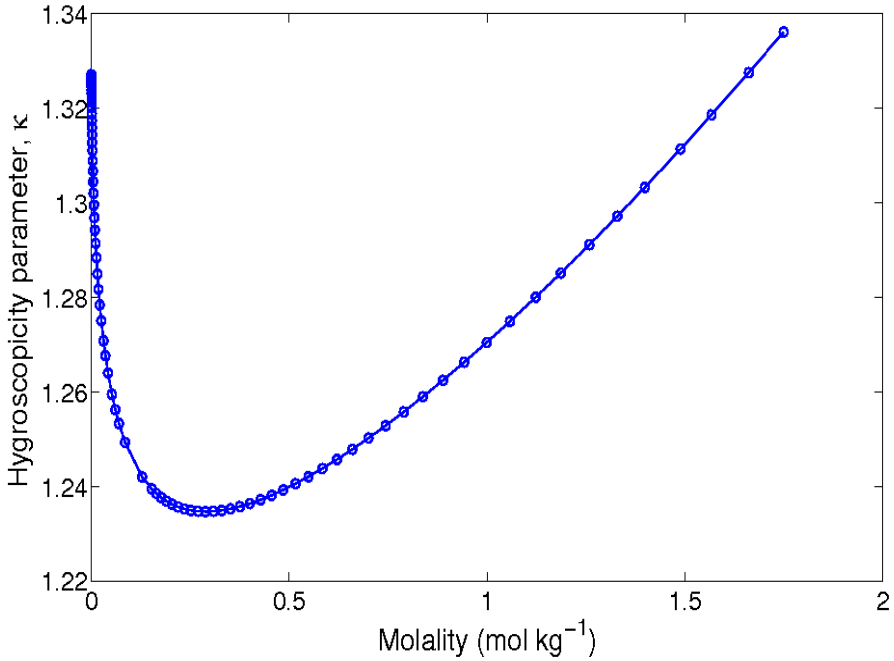

Figure 2.2: *Dependence of hygroscopicity parameter κ as a function of solute (NaCl) molality. The expression $\kappa = f(\mu_s)$ can be found in eq (2.6).*

parameterization (Pruppacher and Klett (1997)). In all simulations using the κ-Köhler model, σ was set to $0.072\,\mathrm{J\,m^{-2}}$ (Petters and Kreidenweis (2007)).

2.2.3 Model evaluation

To validate the cloud parcel model after implementation of the κ-Köhler approach, simulations with the OS Köhler model have been compared against the results of an alternative cloud parcel model using sodium chloride particles as a surrogate for atmospheric aerosols (Segal and Khain (2006)).

The influence of the different Köhler model approaches was evaluated in test simulations for two cloud base updraft velocities ($w = 1.5\,\mathrm{m\,s^{-1}}$ and $3.0\,\mathrm{m\,s^{-1}}$) with a total aerosol particle number concentration of $N_{CN} = 3000\,\mathrm{cm^{-3}}$ and a log-normal size distribution as specified by Segal and Khain (2006) with a geometric mean diameter of 60 nm and a standard deviation of $\sigma = 1.35$. Figure 2.1 shows that the maximum supersaturations S_{max} as well as the cloud droplet number concentrations N_{CD} determined with the κ-Köhler model were slightly lower than with the OS reference model. The differences were caused by the different approaches of a_w calculations. To make a_w the same, i.e. $a_w(OS) = a_w(\kappa)$, the expression of κ as a function of μ_s, eq (2.6) is

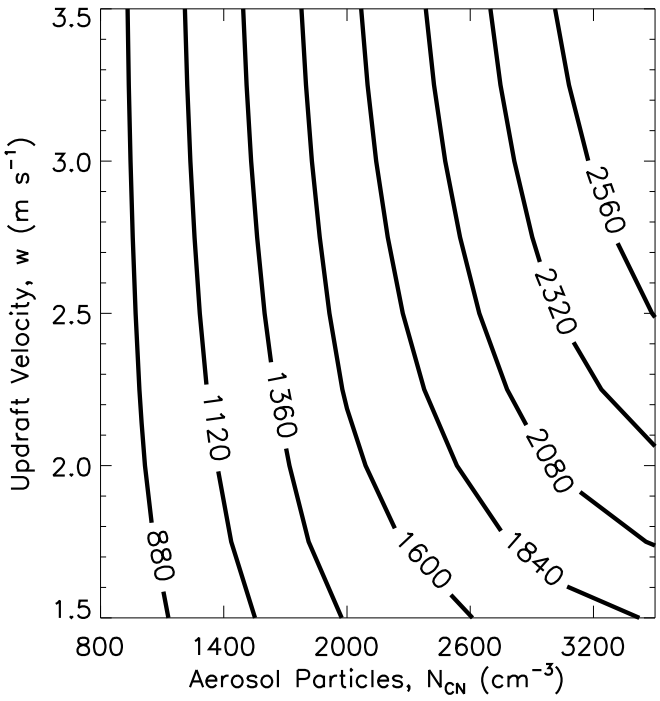

Figure 2.3: *Cloud droplet number concentrations (N_{CD}, cm^{-3}; isolines) calculated as a function of updraft velocity (w, $\mathrm{m\,s}^{-1}$) and initial aerosol particle number concentration (N_{CN}, cm^{-3}) with particle properties as specified by Segal and Khain (2006).*

obtained. Fig. 2 showed the dependence of κ on μ_s for sodium chloride.

$$\kappa = f(\mu_s) = (\exp(\nu_s \Phi_s \mu_s M_w) - 1)\frac{V_w}{V_s} \tag{2.6}$$

After implementing $\kappa = f(\mu_s)$, eq (2.6), the κ-Köhler model produced the exact same results as the OS reference model (Fig. 2.1), demonstrating the equivalence of the two model formulations. Additional tests with typical particle size distributions of urban aerosols (Su et al. (2009)) showed similar deviations in S_{max} and N_{CD} for constant $\kappa = 1.28$ and no deviations with $\kappa = f(\mu_s)$.

The validity of the cloud parcel model with the κ-Köhler approach was also confirmed by further model simulations with $N_{CN} = 800 - 3600\,\mathrm{cm} - 3$ and $w = 0.5 - 3.5\,\mathrm{m\,s}^{-1}$ with a κ of 1.28 representing $NaCl$. The resulting cloud droplet concentrations shown in Fig. 2.3 are in fair agreement with the results of Segal and Khain (2006, Fig. 6f) who investigated CCN activation with an alternative air parcel model with spectral description of warm cloud microphysics. At low N_{CN}, the cloud droplet number concentrations were up to $\sim 15\,\%$ higher in this model, but at high N_{CN} they

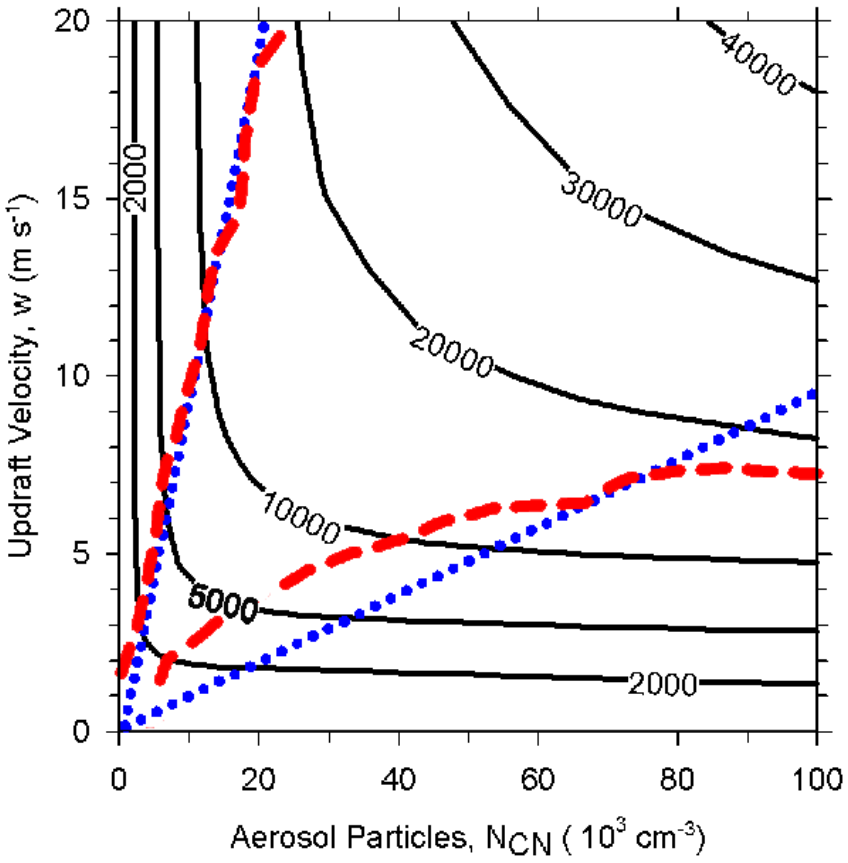

Figure 2.4: *Cloud droplet number concentrations (N_{CD}, cm^{-3}; isolines) calculated as a function of updraft velocity (w, $\mathrm{m\,s}^{-1}$) and initial aerosol particle number concentration (N_{CN}, cm^{-3}) on a normal scale. Red dashed lines indicate the exact borders determined by $S(N_{CN})/S(w) = 4$ or 1/4, between different regimes. Blue dotted lines indicate approximate borders defined by w/N_{CN} ratio between different regimes.*

were essentially the same as in Segal and Khain (2006, Fig. 6f).

2.3 Results and Discussion

2.3.1 Different regimes of CCN activation

To probe and characterize the influence of aerosol particle number concentration and updraft velocity on CCN activation and droplet formation at the base of pyro-convective clouds, cloud parcel model simulations assuming a mono-modal particle size distribution characteristic for young biomass burning aerosols have been performed. The dry particle size distribution is determined by an accumulation mode with a count me-

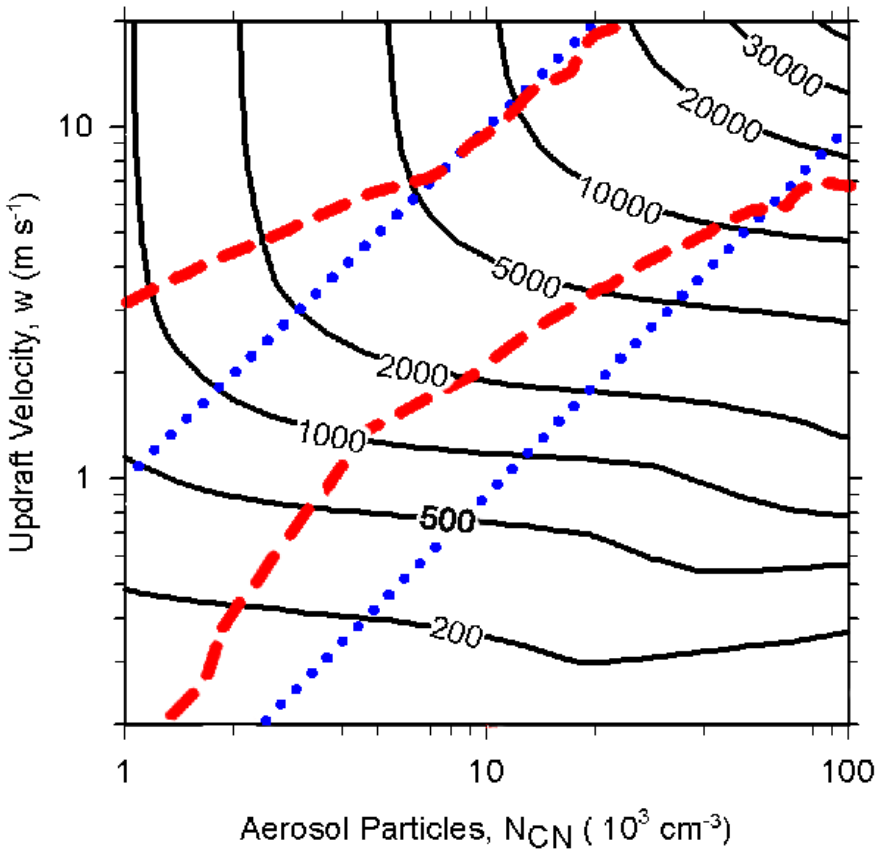

Figure 2.5: *Same as 2.4 but with a log-log scale.*

dian or geometric mean diameter of $D_g = 120\,\mathrm{nm}$, a geometric standard deviation of $\sigma_g = 1.5$ (Reid et al. (2005)), and the hygroscopic properties are described by an effective hygroscopicity parameter of 0.2 (Andreae and Rosenfeld (2008), Rose et al. (2008b), Pöschl et al. (2009)). The effects of variations in hygroscopicity will be addressed below (Sect. 2.3.2). In a series of 961 model runs the updraft velocity and the initial number concentration of aerosol particles have been varied systematically over the range of $w = 0.25 - 20\,\mathrm{m\,s^{-1}}$ and $N_{CN} = 0.2 - 100 \cdot 10^3\,\mathrm{cm^{-3}}$.

Figure 2.4 and 2.5 show the number concentration of cloud droplets, N_{CD}, that are formed at the cloud base as a function of w and N_{CN}. Note, that N_{CN} as used in this study effectively corresponds to $N_{CN,30}$, i.e. the number of aerosol particles larger than 30 nm. The corresponding activated fractions of aerosol particles and the maximum water vapor supersaturations reached in the ascending air masses S_{max} are shown in Figs. 2.6 and 2.7, respectively.

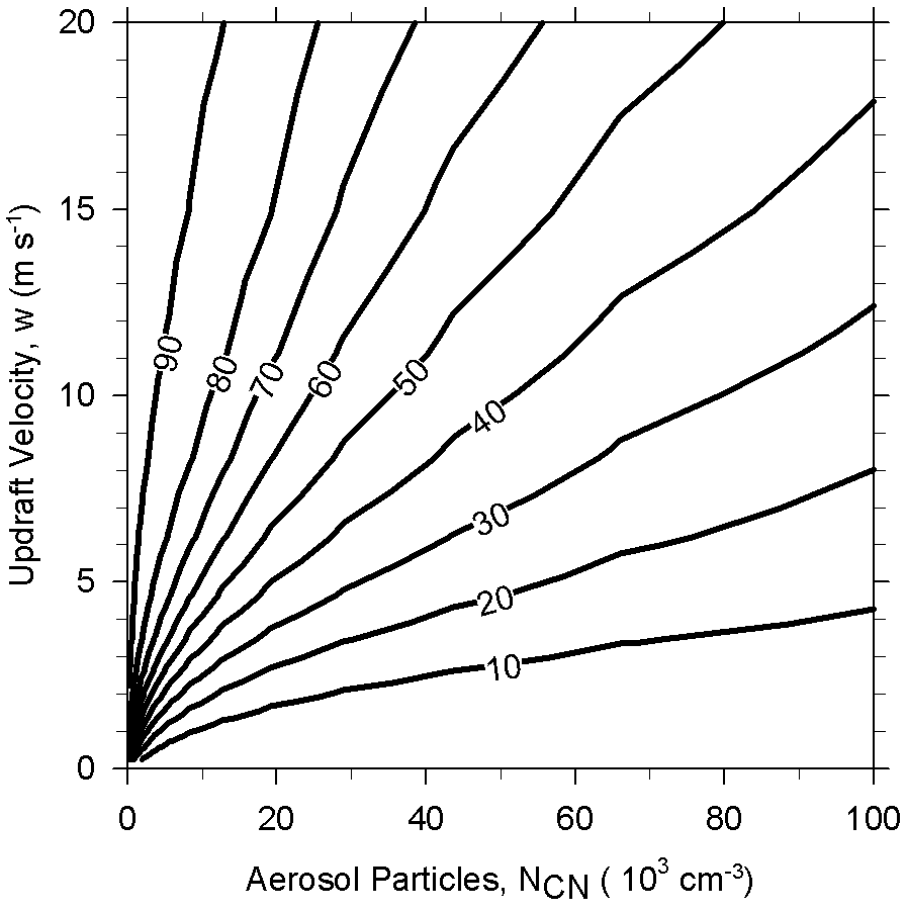

Figure 2.6: *Fraction of activated aerosol particles (N_{CD}/N_{CN}, %, isolines) calculated as a function of updraft velocity (w, $\mathrm{m\,s^{-1}}$) and initial aerosol particle number concentration (N_{CN}, $\mathrm{cm^{-3}}$).*

The N_{CD} isolines (isopleths) shown in Fig. 2.4 and 2.5 exhibit three distinctly different regimes of CCN activation and cloud droplet formation: (1) an aerosol-limited regime in the upper left sector of the plot; (2) an updraft-limited regime in the lower right sector; and (3) an aerosol- and updraft-sensitive regime (transitional regime) along the diagonal from the lower left to the upper right corner (ridge of N_{CD} isopleths). Note that the appearance of the cloud droplet isopleth plot is similar to that of the ozone isopleth plots which are widely used in atmospheric chemistry to distinguish and describe the so-called NO_x- and VOC-limited regimes of ozone production and concentration (Seinfeld and Pandis (2006), p. 236).

The aerosol-limited regime of CCN activation is characterized by a relatively high ratio between the updraft velocity and particle number concentration ($w/N_{CN} > 10^{-3}\,\mathrm{m\,s^{-1}\,cm^3}$), Fig. 2.4 and 2.5), by a high activated fraction of aerosol particles ($N_{CD}/N_{CN} > 90\,\%$, Fig. 2.6), and by high maximum values of water vapor super-

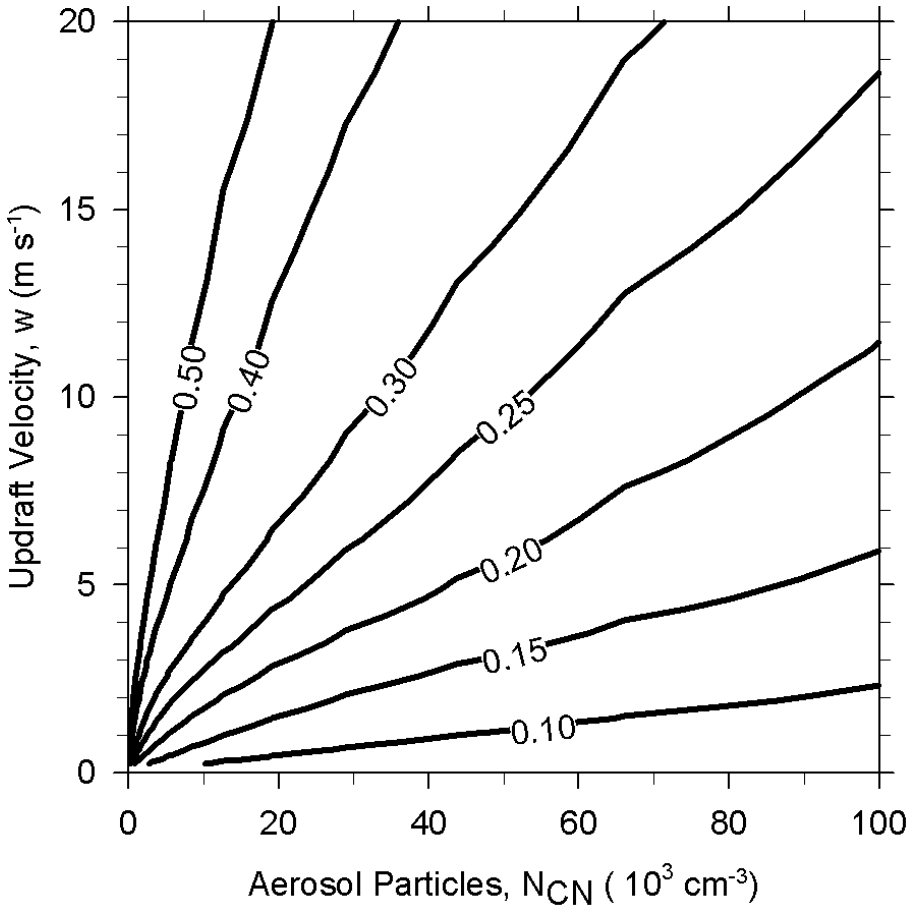

Figure 2.7: *Maximum supersaturation (S_{max}, %, isolines) calculated as a function of updraft velocity (w, $\mathrm{m\,s^{-1}}$) and initial aerosol particle number concentration (N_{CN}, $\mathrm{cm^{-3}}$).*

saturation ($S_{max} > 0.5\,\%$, Fig. 2.7). In this regime, N_{CD} is directly proportional to N_{CN} ($\partial N_{CD}/\partial N_{CN} \approx 1$) and practically independent of w (isolines parallel to y axis; $N_{CD}/w \approx 0$). The high updraft velocities lead to maximum supersaturations large enough to activate nearly all aerosol particles except very small ones at the lower end of the size-distribution (critical dry diameter of CCN activation < 60 nm).

The updraft-limited regime is characterized by a relatively low ratio between the updraft velocity and particle number concentration ($w/N_{CN} < 10^{-4}\,\mathrm{m\,s^{-1}\,cm^3}$, Fig. 2.4 and 2.5), by a low activated fraction of aerosol particles ($N_{CD}/N_{CN} < 20\,\%$, Fig. 2.6), and by low maximum values of water vapor supersaturation ($S_{max} < 0.2\,\%$, Fig. 2.7). In this regime N_{CD} exhibits a linear dependence on w ($\partial N_{CD}/\partial w \approx 2 \cdot 10^3\,\mathrm{cm^{-3}\,m^{-1}s}$) and a very weak dependence on N_{CN} (small slope of isolines; $N_{CD}/N_{CN} \approx 0.02$). Due to the relatively low updraft velocities and high aerosol concentrations, the maximum supersaturations are so small that only large particles in the upper half of the size

distribution are activated (critical dry diameter > 120 nm). Under extremely low w/N_{CN} conditions, water would be taken up by aerosol particles, the supersaturation would be quenched and N_{CD} would drop to zero. E.g. for $w = 0.1\,\mathrm{m\,s^{-1}}$, N_{CD} would still be increased by adding more particles up to $N_{CN} \approx 1 \cdot 10^5\,\mathrm{cm^{-3}}$, but would drop to zero at $N_{CN} > 2 \cdot 10^5\,\mathrm{cm^{-3}}$. This "supersaturation-quenched regime" where an increase in N_{CN} would lead to a reduction of N_{CD}, can be regarded as a special sub-regime of the updraft limited-regime of CCN-activation. Note that a comparable sub-regime is also known in ozone chemistry: the NO_x titration subregime in the VOCs-limited regime. In that sub-regime, increasing NO_x leads to a decrease of ozone concentration. These similarities show the true color of nature beneath the complicated decoration, i.e., the similar principles underlying different physico-chemical processes in our environment.

The aerosol- and updraft-sensitive regime (transitional regime) is characterized by intermediate values of the ratio between the updraft velocity and particle number concentration ($w/N_{CN} \approx 0.5 \cdot 10^{-3}\,\mathrm{m\,s^{-1}\,cm^3}$), Fig. 2.4 and 2.5), of the activated fraction of aerosol particles ($N_{CD}/N_{CN} \approx 20 - 90\,\%$, Fig. 2.6), and of the maximum values of water vapor supersaturation ($S_{max} \approx 0.2 - 0.5\,\%$, Fig. 2.7). In this regime N_{CD} exhibits non-linear dependences on both w and N_{CN} (strong curvature of isolines; $\partial N_{CD}/\partial w \approx (0 - 2) \cdot 10^3\,\mathrm{m\,s^{-1}\,cm^3}$; $\partial N_{CD}/\partial N_{CN} \approx 0.4 - 1$). Depending on the maximum supersaturations, the critical dry diameter for CCN activation ranges from well below up to the maximum of the aerosol particle size distribution ($\sim 60 - 120$ nm).

In the discussions above and based on Fig. 2.4, the borders between the three regimes were approximately defined by a constant w/N_{CN} ratio. More generally and more accurately, the borders between the regimes can be defined by the relative sensitivities of N_{CD} against changes in w and N_{CN}, $\partial \ln N_{CD}/\partial \ln w \approx (\Delta N_{CD}/N_{CD})/(\Delta w/w)$ and $\partial \ln N_{CD}/\partial \ln N_{CN} \approx (\Delta N_{CD}/N_{CD})/(\Delta N_{CN}/N_{CN})$. From model results, the relative sensitivity ratio $RS = (\partial \ln N_{CD}/\partial \ln w)\ /(\partial \ln N_{CD}/\partial \ln N_{CN})$ can be calculated and used as a general parameter to quantitatively define and distinguish the different regimes of CCN activation.

For a wide range of pyro-convective conditions, the approximate borderlines ($w/N_{CN} \approx 10^{-3}$ or $10^{-4}\,\mathrm{m, s^{-1}cm^{-3}}$) are in fair agreement with the borderlines determined by the general method using $RS = 4 or 1/4$, respectively (Fig. 2.4). At low updraft velocities, however, the influence of w is stronger than indicated by the approximate borderlines, i.e., the approximate borders of the transition regime deviated towards updraft limited regime (Fig. 2.5).

In an earlier study, Twomey (1977) described the roles of updraft and aerosol number concentration by an analytical approximation of $N_{CD} \propto N_{CCN,1}^{2/(alpha+2)} w^{3\alpha/(2\alpha+4)}$ where $N_{CCN,1}$ is the cumulative CCN concentration at 1 % supersaturation, w is the updraft velocity and α is the slope of CCN supersaturation spectrum in the log-log scale. For a fixed size distribution, $N_{CCN,1}$ is proportional to N_{CN} used in this study. According to the analytical approximation, the N_{CD} isolines (isopleths) should be linear in a log-log plot. Thus the N_{CD} isolines on a log-log scale as shown in Fig. 2.5 have been also plotted. For either aerosol-limited or updraft-limited regimes, the isolines can be approximated by linear lines with different slope. However, over the whole range of $N_{CCN,1}$ and w, the isoline is obviously non-linear. This means the Twomey approximation with fixed α is not applicable over the whole investigated range of conditions.

The key features of the three regimes of CCN activation illustrated in Figs. 2.4-2.7 are not specific for young biomass burning aerosols and pyro-convective conditions but likely to apply also for other types of aerosols and meteorological conditions.

This is due to the fairly similar CCN properties of aerosols in most regions of the world (Andreae and Rosenfeld (2008),Rose et al. (2008a), Gunthe et al. (2009b)) and confirmed by sensitivity studies with different aerosol size distributions (not shown) and effective hygroscopicities (Sect. 2.3.2). This was confirmed by sensitivity studies with different aerosol size distributions ($D_g = 60 - 200$nm; $\sigma_g = 1.2 - 2.0$). Moreover, Su et al. (2009) found the same type of regimes over w and N_{CN} in their simulations based on measured particle size distribution and κ values from mega-city Beijing and the same applied for pristine rainforest aerosols (Gunthe et al. (2009b)). Under these different conditions, the levels of isolines change but the shape stays the same. Just like in ozone chemistry, the existence of NO_x- and VOCs- limited regimes relations have to be adjusted to different conditions.

In the atmosphere, aerosol-limited conditions of CCN activation with high updraft velocities and low aerosol concentrations may occur in deep convection of clean air over tropical oceans and remote continental regions, as well as in thunderstorms in maritime air over land with strong vertical forcing of clean air masses (Murphey et al. (2006)). Updraft-limited CCN activation with low updraft velocities and high aerosol concentrations is likely to occur in shallow convection of polluted air over locations or regions with strong sources of aerosols such as biomass burning and fossil fuel combustion in agricultural regions and mega-cities (Mönkkönen et al. (2005), Molina et al. (2007), Zhang et al. (2008), Rose et al. (2008b), Wiedensohler et al. (2009)).

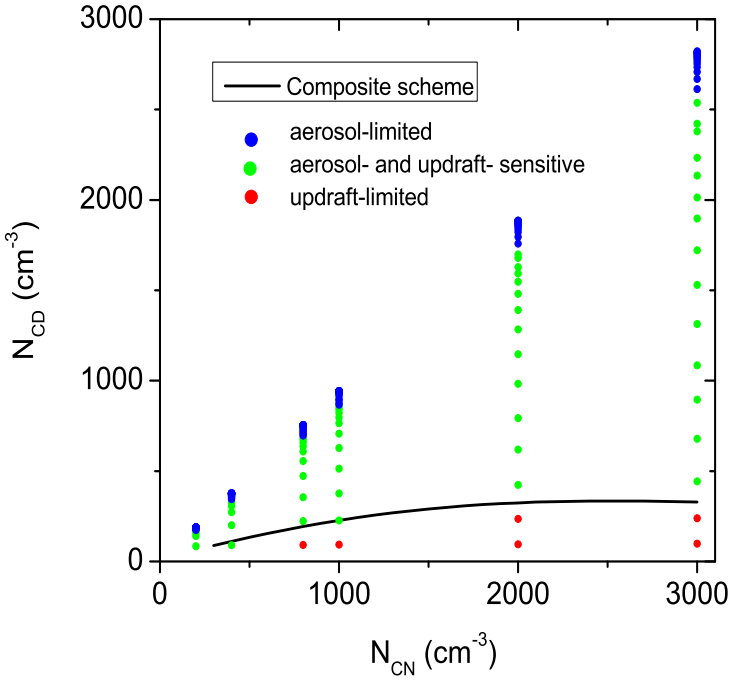

Figure 2.8: *The thick line labeled "Composite scheme" is obtained from a composite theoretical parameterization that fits the INDOEX aircraft data for the Arabian Sea (Ramanathan et al. (2001a) and equations for the line can be foind in the Appendix A of Ramanathan et al. (2001b)). The colored points are obtained from the same cloud parcel model simulations as shown in Fig. 2.4 and 2.5. The colors indicate the regimes determined by the w/N_{CN} ratio.*

Aerosol- and updraft-sensitive (transitional) conditions of CCN activation can occur in a wide range of regions and meteorological situations with low/moderate updraft velocities and aerosol concentrations (shallow convection in moderately polluted continental air), as well as in the very high updraft velocities and aerosol concentrations typical for pyro-convection.

In comparison to this model results, the observed aerosol-cloud droplet relations reported by Ramanathan et al. (2001a)) would lie at the border between updraft-limited and transitional regimes of CCN activation (Fig. 2.8), corresponding to updraft velocities around $\approx 0.5\,\mathrm{m\,s^{-1}}$. Note, however, that the reported relations are characteristic for marine rather than pyro-convective conditions, which may limit the comparability. Model investigations using typical marine aerosol properties are under way and will be presented and discussed elsewhere (Gunthe et al. (2009a)). Nevertheless, first results indicate that the regimes are not very different.

For pyro-convective clouds with $w \approx 5 - 20\,\mathrm{m\,s^{-1}}$ and $N_{CN} \approx 10^4 - 10^5\,\mathrm{cm^{-3}}$, this model results indicate very high droplet number concentrations at the cloud base ($N_{CD} \approx (0.5{-}4){\cdot}10^4\,\mathrm{cm^{-3}}$; Fig. 2.4 and 2.5). The corresponding maximum water vapor supersaturations and activated fractions of aerosol particles are in the range of $0.2 - 0.5\,\%$ and $20 - 80\,\%$, respectively (Figs. 2.6 and 2.7). The activated particle fractions are substantially higher than assumed in earlier model studies of pyro-convective clouds (5 %, Trentmann et al. (2006)). On the other hand, the linear extrapolation of this results to extreme pyro-convective conditions ($N_{CN} = 4 \cdot 10^5\,\mathrm{cm^{-3}}$, $w = 20\,\mathrm{m\,s^{-1}}$) is consistent with the results of Chuang et al. (1992): $\mathrm{S}_{max} = 0.15$, $N_{CD}/N_{CN} = 16\,\%$).

When an aerosol particle is activated to a cloud droplet it is also scavenged from the atmosphere (nucleation scavenging). The remaining fraction of the aerosol particles is transported as interstitial aerosol in the pyro-cloud and, unless they are scavenged by impaction with hydrometeors, they will be released into the atmosphere in the outflow region of the pyro-cloud, which can be as high as the upper troposphere or the lower stratosphere (e.g., Fromm et al. (2005)) To quantify the number of aerosol particles in the outflow region of pyro-clouds, full three-dimensional simulations of pyro-clouds are required that take into account the interaction of aerosol particles and hydrometeors. Combining pyro-convective modeling activities (e.g., Trentmann et al. (2006), Luderer et al. (2006)) with the investigation of aerosol-cloud interactions in convective clouds (e.g., Ekman et al. (2008)) should help to better quantify the amount of aerosol deposited in the UT/LS region by pyro-convection.

2.3.2 Aerosol particle hygroscopicity and size distribution

To probe and characterize the influence of aerosol particle hygroscopicity on CCN activation at the base of pyro-convective clouds, additional cloud parcel simulations for exemplary points in the three different regimes of CCN activation (aerosol-limited; updraft-limited; aerosol- and updraft-sensitive; Fig. 2.4 and 2.5) have been performed.

First the relative importance of the particle size distribution and hygroscopicity is adressed. After that hygroscopicity effects in more detail are investigated and discussed.

Relative sensitivities

Based on cloud parcel model simulations, Feingold proposed a linear regression method to calculate the relative sensitivity of one parameter (i.e. cloud-top effective radius) against the other parameters (variables). McFiggans et al. (2006) have also used this

	Aerosol-limited regime ($S_{max} > 0.5\%$)	Transitional regime ($S_{max} = 0.2 - 0.5\%$)	Updraft-limited regime ($S_{max} < 0.2\%$)
D_g	0.39	0.45	0.32
σ_g	-0.50	-0.91	-0.92
κ	0.15	0.17	0.13

Table 2.1: *Average relative sensitivities of N_{CD} on X_i, $S(X_i) = \partial \ln N_{CD}/\partial \ln X_i$ (where X_i is one of D_g, σ_g and κ. The three regimes are (a) aerosol-limited regime ($w = 15\,\mathrm{m\,s^{-1}}$ and $N_{CN} = 1 \cdot 10^4\,\mathrm{cm^{-3}}$); (b) transitional regime ($w = 10\,\mathrm{m\,s^{-1}}$ and $N_{CN} = 5 \cdot 10^4\,\mathrm{cm^{-3}}$); (c) updraft-limited regime ($w = 5\,\mathrm{m\,s^{-1}}$ and $N_{CN} = 8 \cdot 10^4\,\mathrm{cm^{-3}}$). The ranges of X_i are $D_g = 60 - 200\,\mathrm{nm}$, $\sigma_g = 1.2 - 2.0$, hygroscopicity $\kappa = 0.005 - 0.6$.*

method to calculate the sensitivities of cloud droplet concentrations on other parameters, defining sensitivity $S(X_i) = \partial \ln N_{CD}/\partial \ln X_i$ where X_i is the investigated parameter affecting N_{CD}, i.e., N_{CN}, D_g, σ_g, w or the mass fraction of ammonium sulphate ϵ as a proxy of particle hygroscopicity. To calculate, for example, $S(N_{CN})$ they plotted all values of $N_{CD}(N_{CN}, D_g, \sigma_g, w, \epsilon)$, i.e., N_{CD} calculated as a function of variable values of N_{CN}, D_g, σ_g, w and ϵ against N_{CN} on a log-log scale. Then a linear regression was applied, and the slope of the fit line was taken as $S(N_{CN})$.

When this method was applied in the supersaturation-quenched regime where N_{CD} approaches zero (in case of very high N_{CN} and/or D_g values), $\ln N_C D$ values approaching $-\infty$ can strongly influence and distort the slope of the linear fit. To avoid this problem, a modified method in which all values of N_{CD} calculated at a given value of X_i were averaged prior to fitting was used. Then the averaged values of N_{CD} were plotted against X_i on a log-log scale and linearly fitted. Since this method gives averaged values of relative sensitivities, it is denoted $\overline{S}(N_{CN})$.

In the sensitivity studies, the same model setup and input parameters as detailed above (Section 2.3.1) was used to investigate three cases in different regimes, i.e. one in updraft –limited regime ($w = 5\,\mathrm{m,\ s^{-1}}$, $N_{CN} = 8 \cdot 10^4 \mathrm{cm^{-3}}$), one in aerosol-limited regime ($w = 15\,\mathrm{m,\ s^{-1}}$, $N_{CN} = 1 \cdot 10^4 \mathrm{cm^{-3}}$) and another one in the transitional regime ($w = 10\,\mathrm{m,\ s^{-1}}$, $N_{CN} = 5 \cdot 10^4 \mathrm{cm^{-3}}$). For each of the three investigated combinations of w and N_{CN} the size distribution and hygroscopicity parameters were varied as follows: $D_g = 60 - 200\,\mathrm{nm}$, $\sigma_g = 1.2 - 2.0$, and $\kappa = 0.005 - 0.6$.

As shown in Tab. 2.1, $\overline{S}(X_i)$ is positive for D_g and κ in all the regimes. This is because larger particles or more hygroscopic particles have a lower critical supersatura-

tion. Across all regimes of CCN activation, the sensitivity of N_{CD} against particle size, $\overline{S}(D_g)$, is two to three times higher than the sensitivity against chemical composition, $\overline{(S)}(\kappa)$. This is consistent with the relative sensitivity of s_c on D_g and κ, in which $(\partial \ln s_c/\partial D_g)/(\partial \ln s_c/\partial \kappa) = 3$. The sign of $\overline{S}(\sigma_g)$ is negative because the tail of the distribution at large sizes results in activation of larger droplets, reducing supersaturation and N_{CD} values. For both $\overline{S}(D_g)$ and $\overline{S}(\kappa)$ the deviations between the aerosol-limited, transitional and updraft limited scenarios agreed to within $+/-15\,\%$. In contrast, $\overline{S}(\sigma_g)$ in the aerosol-limited scenario was by a factor of 1.8 lower than in the transitional and updraft-limited scenarios. The sensitivities determined in this case study for the aerosol limited regime are very similar to the values reported by McFiggans et al. (2006) for their polluted case ($3000\,\mathrm{cm}^{-3} > N_{CN} > 1000\,\mathrm{cm}^{-3}$).

As N_{CD} is a function of five parameters (N_{CN}, D_g, σ_g, w and κ), $\overline{S}(X_i) = \partial \ln N_{CD}/\partial \ln X_i$ can also be influenced by each of the parameters. As mentioned above, the sensitivities calculated in this section represent just an average sensitivity estimate. In the following section it is explored how the relatively low average sensitivity against κ varies under different conditions.

Hygroscopicity effects

The chemical effects on N_{CD}, i.e. $S(\kappa)$, in different aerosol chemical composition conditions (different κ conditions) for the three regimes were studied. The same model setup and input parameters are used as detailed above (Section 2.3.1) and only κ was varied from 0.005 to 0.6, covering the full range of effective hygroscopicity parameters reported for CCN in continental air (Sect. 2.2, Andreae and Rosenfeld (2008) and references therein).

Figure 2.9a shows the model results of N_{CD} and S_{max} for exemplary conditions in the aerosol-limited regime ($w = 15\,\mathrm{m,\ s}^{-1}$, $N_{CN} = 1 \cdot 10^4 \mathrm{cm}^{-3}$). Under these conditions and for aerosol particles of medium or high hygroscopicity ($\kappa \geq 0.2$), the cloud droplet number concentration is practically independent of κ (plateau level in Fig. 2.9a). The relative sensitivities $S(\kappa) = \partial \ln N_{CD}/\partial \ln \kappa \approx (\Delta N_{CD}/N_{CD})/(\Delta \kappa)/\kappa)$ is ≤ 0.06 i.e., a$\sim 50\,\%$ difference in κ would change N_{CD} by less than $3\,\%$ (Tab. 2.2). For aerosol particles with low hygroscopicity ($0.05 < \kappa < 0.2$), the dependence of N_{CD} on κ is still modest, with relative sensitivities $S(\kappa)$ in the range of $0.06 - 0.2$. Only for particles with very low hygroscopicity ($\kappa < 0.05$), N_{CD} depends strongly on κ. The relative sensitivities $S(\kappa)$ are ≥ 0.2, i.e., a $\sim 50\,\%$ difference in κ would change N_{CD} by more

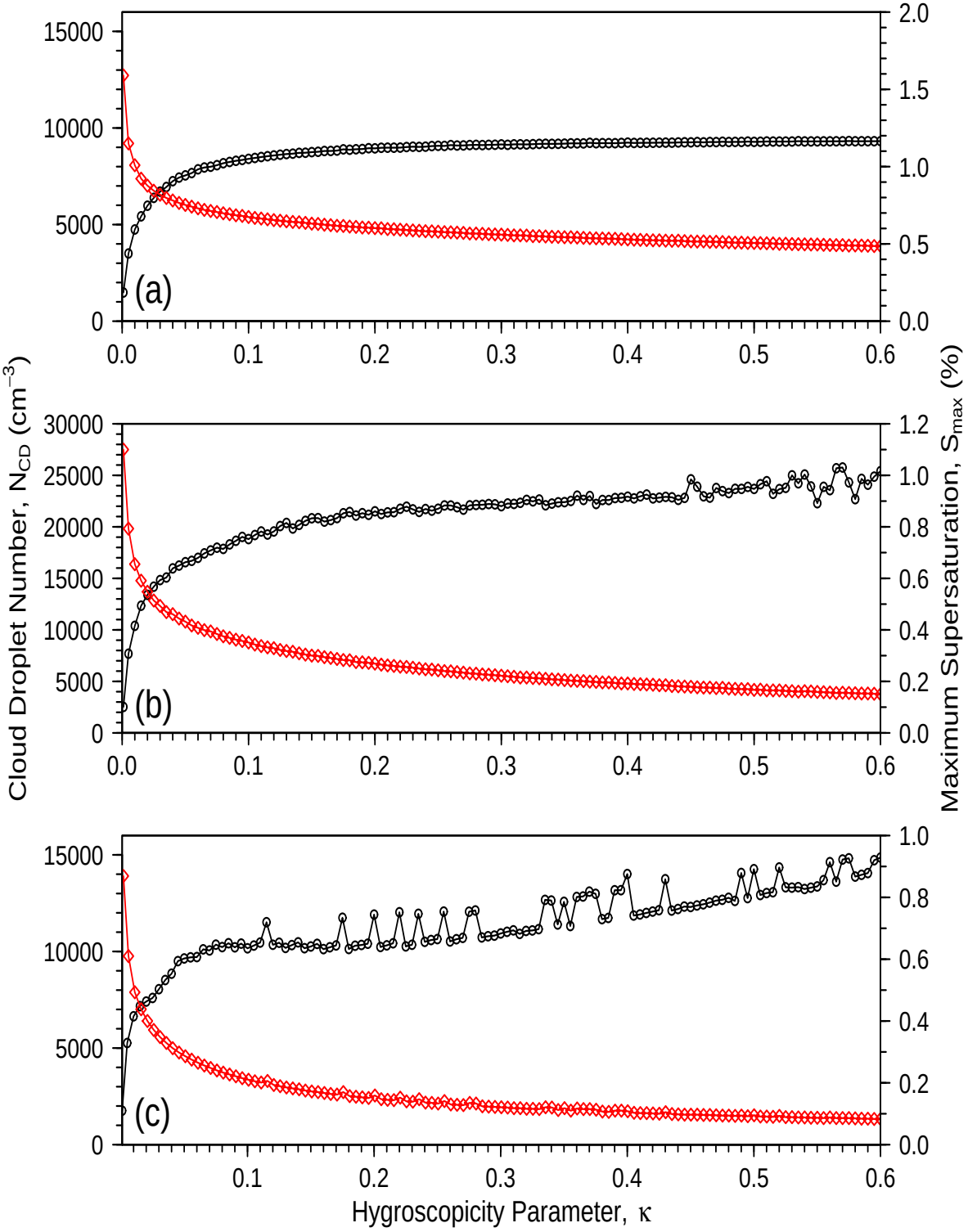

Figure 2.9: *Dependence of cloud droplet number concentrations (N_{CD}, cm^{-3}, black) and maximum supersaturations (S_{max}, %, red) on aerosol particle hygroscopicity ($\kappa = 0.005 - 0.6$): (a) aerosol-limited regime ($w = 15\,\mathrm{m\,s}^{-1}$ and $N_{CN} = 1 \cdot 10^4\,\mathrm{cm}^{-3}$); (b) aerosol- and updraft-sensitive regime ($w = 10\,\mathrm{m\,s}^{-1}$ and $N_{CN} = 5 \cdot 10^4\,\mathrm{cm}^{-3}$); (c) updraft-limited regime ($w = 5\,\mathrm{m\,s}^{-1}$ and $N_{CN} = 8 \cdot 10^4\,\mathrm{cm}^{-3}$).*

κ	Aerosol-limited regime ($S_{max} > 0.5\%$)		Transitional regime ($S_{max} = 0.2 - 0.5\%$)		Updraft-limited regime ($S_{max} < 0.2\%$)	
	N_{CD} , $10^3\,\mathrm{cm}^{-3}$	$\frac{R_{N_{CD}}}{R_\kappa}$	N_{CD} , $10^3\,\mathrm{cm}^{-3}$	$\frac{R_{N_{CD}}}{R_\kappa}$	N_{CD} , $10^3\,\mathrm{cm}^{-3}$	$\frac{R_{N_{CD}}}{R_\kappa}$
0.025	6.0	0.50	14.0	0.50	8.0	0.50
0.05	7.5	0.23	16.5	0.22	9.6	0.10
0.1	8.4	0.12	19.0	0.21	10.2	0.06
0.2	8.9	0.06	21.0	0.10	10.5	0.10
0.3	9.1	0.03	22.0	0.08	11.0	0.22
0.4	9.2	0.02	23.0	0.11	13.0	0.30
0.5	9.3	0.02	24.0	0.14	13.3	0.41

Table 2.2: *Relative differential quotients $\frac{R_{N_{CD}}}{R_\kappa}$ with $R_{N_{CD}} = \frac{\Delta N_{CD}}{N_{CD}}$ and $R_\kappa = \frac{\Delta \kappa}{\kappa}$ characterizing the dependence of cloud droplet number concentration (N_{CD}) on aerosol particle hygroscopicity (κ) in the aerosol limited, aerosol- and updraft-sensitive, and updraft-limited regimes of CCN activation. Numerical values correspond to the exemplary scenarios illustradet in Fig 2.9.*

than 10 % (Tab. 2.2).

Figure 2.9b shows the model results for exemplary conditions in the transitional regime ($w = 10\,\mathrm{m,\ s}^{-1}$, $N_{CN} = 5 \cdot 10^4 \mathrm{cm}^{-3}$). The dependence of N_{CD} on κ is qualitatively similar to the aerosol-limited regime (Fig. 2.9a), but the relative sensitivities $S(\kappa)$ are larger, i.e., differences in κ result in larger differences in N_{CD} (Tab. 2.2). Note that at $\kappa > 0.4$ the maximum supersaturation dropped below 0.2 %, indicating a changeover into the updraft limited regime. At $\kappa > 0.45$ strong wiggles/outliers in the curve of N_{CD} vs. κ indicate that the model resolution becomes a limiting factor under these conditions (low S, high N_{CN}).

Figure 2.9c shows the model results for exemplary conditions in the updraft-limited regime ($w = 5\,\mathrm{m,\ s}^{-1}$, $N_{CN} = 8 \cdot 10^4 \mathrm{cm}^{-3}$). Again the dependence of N_{CD} on κ is qualitatively similar to the aerosol-limited regime (Fig. 2.9a), but the relative sensitivities $S(\kappa)$ are smaller for particles with low hygroscopicity ($0.05 < \kappa < 0.2$) and larger for particles with medium or high hygroscopicity ($\kappa \geq 0.2$, Tab. 2.2). Note, however, that at $\kappa \approx 0.12$ the maximum supersaturations drop already below 0.2 % and strong wiggles/outliers in the curve of N_{CD} vs. κ indicate that the model resolution becomes a limiting factor.

Overall, the results summarized in Tab. 2.2 and Fig. 2.9 show that within the range of effective hygroscopicity parameters that is characteristic for continental atmospheric aerosols ($\kappa \approx 0.05 - 0.6$), N_{CD} does not strongly depend on the actual value of κ. Only for aerosols with very low average hygroscopicity ($\kappa < 0.05$, all regimes) and in the updraft-limited regime also for aerosols with higher than average hygroscopicity ($\kappa > 0.3$, $S_{max} < 0.2\,\%$) did the relative sensitivities $S(\kappa)$ exceed values of ~ 0.2, indicating that a 50 % difference in κ would change N_{CD} by more than 10 %. At $\kappa < 0.03$ and in the updraft-limited regime at $\kappa > 0.5$ ($S_{max} \leq 0.1\,\%$) the relative sensitivities $S(\kappa)$ exceeded values of ~ 0.4, indicating that a 50 % difference in κ would change N_{CD} by more than 20 %. These findings are consistent with earlier studies investigating the influence of aerosol chemical composition on CCN activation in cloud parcel models (e.g., Lance et al. (2004), Rissmann et al. (2007), Ervens et al. (2005), Feingold and Siebert (2009)).

In another set of model simulations a coarse particle mode with $D_{g,c} = 5\,\mu$m and $\sigma_{g,c} = 1.3$ was added, and different fractions of N_{CN} to this mode ($f_{N,c} = 10^{-5}$ to 10^{-3}; Reid et al. (2005), Liu et al. (2009), Janhäll et al. (2009)) were assigned. With $f_{N,c} = 10^{-5}$ and in the aerosol-limited regime, the coarse particle mode had practically no influence on N_{CD} ($\Delta N_{CD}/N_{CD} \approx 0$). In the transitional sensitive regime $\Delta N_{CD}/N_{CD}$ increased with decreasing S_{max} up to $\sim$ 10 % for $f_{N,c} = 10^{-4}$ and $\sim$ 30 % for $f_{N,c} = 10^{-3}$, respectively. At $S_{max} < 0.1\,\%$ in the updraft-limited regime $\Delta N_{CD}/N_{CD}$ exceeded $\sim$ 20 % for $f_{N,c} = 10^{-4}$ and $\sim$ 70 % for $f_{N,c} = 10^{-3}$, respectively.

Overall, the sensitivity studies show that the calculated relative changes in N_{CD} exceeded more than 20 % only in the updraft limited regime. Since pyro-convective clouds are mostly outside the updraft-limited regime and because the model setup is sensitive to small changes at very low supersaturations,the influence of coarse mode particles on CCN activation in the updraft limited regime have not been investigated furthermore. Nevertheless, it is suggested to investigate this aspect further with model studies and observational data for polluted mega-city regions, which are often in the updraft limited regime. For this purpose, it is also suggested to apply models that enable assigning different hygroscopic properties to accumulation mode and coarse mode particles, as the latter are likely to be less hygroscopic. Moreover, potential kinetic limitations of water vapor uptake at the interface and into the bulk of aerosol particles have not been considered in the present study but need to be further explored and clarified (Nenes et al. (2001), Laaksonen et al. (2005), McFiggans et al. (2006),

Pöschl et al. (2007), Engelhart et al. (2008), Ruehl et al. (2008), Asa-Awuku et al. (2009), Mikhailov et al. (2009), Pöschl et al. (2009), and references therein).

2.4 Conclusions

Based on cloud parcel model simulations, it was found that CCN activation and cloud droplet formation can be classified into three regimes roughly depending on the ratio between updraft velocity and particle number concentration (w/N_{CN}): (1) an aerosol-limited regime (high w/N_{CN}), (2) an updraft-limited regime (low w/N_{CN}) and (3) a transitional regime (intermediate w/N_{CN}). The relative sensitivity ratio $RS = (\partial \ln N_{CD}/\partial \ln w)\ /(\partial \ln N_{CD}/\partial \ln N_{CN})$ of 4 : 1 and 1 : 4 can used as a general parameter to quantitatively define and distinguish the different regimes of CCN activation.

Overall, the model results suggest that the variability of initial cloud droplet number concentration in convective clouds is mostly dominated by the variability of updraft velocity and aerosol particle number concentration in the accumulation mode. Coarse mode particles and the variability of particle composition expressed through the hygroscopicity parameter κ appear to play important roles only at very low supersaturation in the updraft-limited regime of CCN activation (in particular at $S \leq 0.1\,\%$).

These conclusions are consistent with field measurements demonstrating that CCN number concentrations in pristine as well as in highly polluted continental air can be efficiently predicted with a constant average hygroscopicity parameter, whereby the relative deviations between modeled and measured CCN concentrations exceeded 50 % only at very low supersaturations ($\leq 0.1\,\%$; Rose et al. (2008b); Gunthe et al. (2009b)). Thus, it is suggested that further experimental and theoretical studies of CCN activation and cloud droplet formation should be focused primarily on the updraft-limited regime, low water vapor supersaturations and potential kinetic limitations of CCN activation.

Chapter 3

Coupling the parcel model to ATHAM

3.1 Introduction

In the previous section the focus was on the activation of aerosol particles to cloud droplets at the vicinity of the cloud base. To investigate the further development of the cloud droplets in the center of an updraft region of a pyro-convective cloud a new model approach will be introduced. The parcel model from Chapter 2 was adjusted to a representative vertical velocity and temperature profile within the highly polluted updraft region of a pyro-convective cloud, which was obtained by a 3D model (ATHAM, Chapter 4). In a previous study by Diehl et al. (2006) describing the situation in clouds over a region with biomass burning the parcel model was initialized without exact knowledge of the vertical velocity and temperature anomaly between the updraft region and the environment. Therefore the new approach of adjusting the parcel model to the conditions within the updraft region of a pyro-convective cloud will lead to a more realistic description of the microphysical processes in this region.

3.2 Methods

3.2.1 Model description

For the present simulations of the microphysical evolution within the updraft region of a pyro-convective cloud, the parcel model presented in Chapter 2 will be used in a different setup. In contrast to the CCN activation setup where no entrainment and

coagulation of droplets were taken into account, the parcel model is used in the original configuration to describe a rising bubble of air, which is affected by the entrainment of ambient air. The entrainment and the release of latent heat by microphysical processes determine the updraft velocity of the air parcel. The advantage of using the parcel model with this setup instead of a 3D model with a more simplified microphysical scheme is that the microphysical processes can be simulated in more detail with the sophisticated microphysical scheme of the parcel model. However, this approach is limited in the description of cloud dynamics and precipitation. Hence, the parcel model simulations will be stopped when the updraft velocity of the air parcel is equal to zero or hydrometeors are falling out of the parcel. Nevertheless, the results from Chapter 2 suggest that the high cloud droplet number concentrations N_{CD} in pyro-convective conditions result in small cloud droplets and therefore the formation of precipitation is suppressed.

The parcel model version for this investigation includes warm and cold cloud microphysics. The warm cloud microphysics contains the hygroscopic growth and shrinking of aerosol particles and cloud droplets (Chapter 2), impaction scavenging and collision and coalescence (coagulation). For the hygroscopic growth of the particles the osmotic coefficient (OS) model described in Section 2.2.2 was used for the calculations in this chapter. The cold microphysical processes include immersion and contact freezing. Due to the high concentration of ice nuclei in pyro-convective conditions, homogeneous freezing as well as deposition freezing can be neglected, because immersion and contact freezing will be the dominant freezing processes (Simmel and Wurzler (2006), Diehl et al. (2006), Diehl et al. (2007)).

Due to the higher computational time resulting from the longer parcel ascent and the complex collision calculations the spectral resolution of the model was reduced to 66 logarithmically equidistant bins between 2 nm and 7 mm compared to the setup in Chapter 2.

The aerosol particles within the air parcel are characterized by a young biomass burning aerosol (Reid et al. (2005)) with a mean diameter of 130 nm and a standard deviation of $\sigma = 1.75$. In the environment aerosol particles are characterized by a haze biomass burning aerosol (Reid et al. (2005)) with a mean diameter of 200 nm and a geometric standard deviation of $\sigma = 1.6$. The concentration of aerosol particles in the environment was set to 10 % compared to the concentration of the aerosol particles within the fire. Due to technical reasons, all particles are assumed to be ammonium sulphate which corresponds to $\kappa = 0.6$ in contrast to $\kappa = 0.2$, which was assumed in

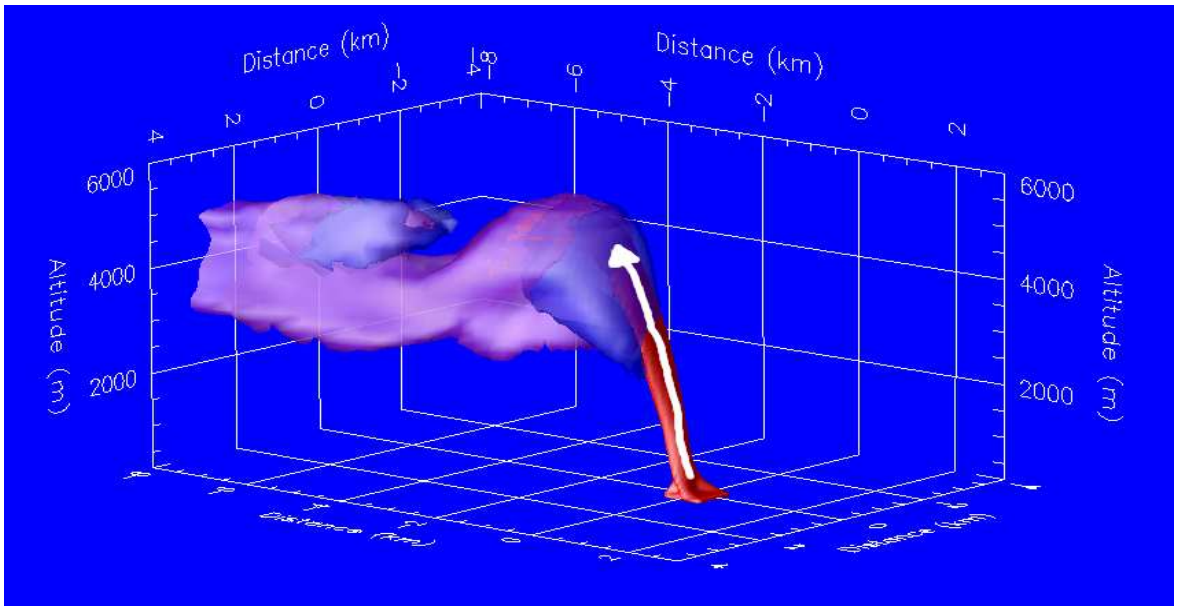

Figure 3.1: *3D model output (ATHAM) of a Brazilian fire after 40 minutes of model integration. The white arrow denotes the updraft region of the pyro-convective cloud, which was used for the adjustment of the parcel model. The iso surfaces represent (red) aerosol particles, (blue) cloud droplets and (violet) rain droplets.*

Chapter 2. The initialization of the parcel model is described in the following section.

3.2.2 Coupling with 3D model

For the initialization of the model runs vertical profiles of the temperature, pressure and relative humidity representing the atmospheric conditions of a Brazilian fire during the SMOCC campaign[1] are used as the background profile for the 3D model ATHAM (Active Trace High Resolution Atmospheric Model) and for the parcel model.

First, the 3D model is used to simulate the general microphysical and dynamical structure of a pyro-convective cloud. Figure 3.1 shows the result of the pyro-convective cloud after a model integration of 40 minutes. At this time a quasi steady-state is reached within the updraft region of the pyro-cloud. Hence, these results are used to obtain a characteristic vertical profile within the updraft region over the fire at this time. The mean updraft velocity at each altitude is derived as the average of all positive vertical velocities in this altitude weighted with the aerosol mass emitted by the fire. Typical vertical profiles within the smoky updraft region of the pyro-convective cloud

[1] http://www.mpch-mainz.mpg.de/smocc/, 23rd Sep 2009)

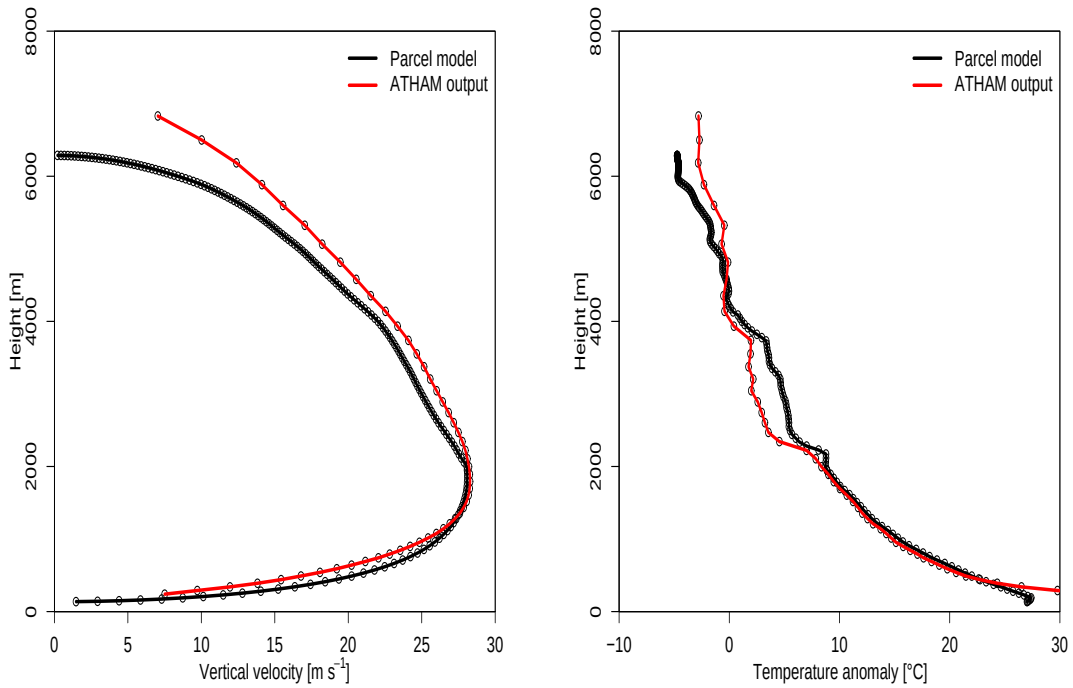

Figure 3.2: *Vertical profile of (left) the updraft velocity and (right) the temperature anomaly (deviation from ambient temperature) for (black) the adjusted parcel model and (red) the 3D model.*

were derived for the vertical wind and the temperature difference between the air parcel and the environment. The updraft region is indicated by the white arrow in Fig. 3.1. On the left side of Fig. 3.2 the averaged profile of the vertical velocity calculated from the 3D model (red) can be seen. On the right side the temperature anomaly, which describes the deviation from the ambient temperature, calculated from the 3D model output (red) is shown.

In a second step, the parameters of the parcel model have to be chosen in such a way that the vertical wind profile and the temperature anomaly profile of the parcel model fit the averaged profiles from ATHAM as closely as possible. This can be achieved by tuning the following parameters in the cloud parcel model:

1. Temperature anomaly at the ground

   The temperature difference between the air parcel and the environment at the ground determines the initial buoyancy of the air parcel. Hence, the warmer the temperature within the air parcel the larger the buoyancy. This means that the temperature anomaly at the ground determines the initial acceleration of the ascending air parcel.

2. Entrainment

   The entrainment determines how much environmental air is mixed into the parcel and how much ambient air is detrained out of the parcel. When cold air from the environment is mixed into the air parcel, the temperature anomaly between the air parcel and the environment is reduced. Therefore, the buoyancy and hence the vertical updraft velocity is decreased. Also the humidity and the number of aerosols is changed by mixing environmental air into the air parcel. The entrainment parameter can be set variable with height.

The temperature anomaly at the ground and the entrainment parameter are varied until good agreement between the parcel model and the ATHAM output is achieved. To obtain the parcel model ascent indicated by the black curves in Fig. 3.2 the temperature anomaly at the ground was set to $\Delta T = 27\,\mathrm{K}$. After several attempts to find the best setup the entrainment parameter was varied with height and was set to $7.5 \cdot 10^{-4}\,\mathrm{m}^{-1}$ below 2000 m, $1.0 \cdot 10^{-3}\,\mathrm{m}^{-1}$ between 2000 and 4000 m and $1.13 \cdot 10^{-3}\,\mathrm{m}^{-1}$ above 4000 m. With these settings for the initial temperature anomaly and the entrainment simulations with different aerosol concentrations have been conducted and presented in the next section.

3.3 Results and Discussion

Figure 3.3 shows the profiles of the number of cloud droplets for different initial aerosol number concentrations in the fire plume. It can be clearly seen that the number of cloud droplets is directly correlated to the number of aerosol particles in accordance with the results from Chapter 2. Note that due to technical reasons here a different aerosol size distribution with a different hygroscopicity is used than in Chapter 2, therefore the fraction of activated cloud droplets at the cloud base is lower in this case of the Brazilian fire than in the simulations from Chapter 2. Nevertheless, the number of cloud droplets at the cloud base is increasing with the number of aerosol particles.

While the air parcel is rising the cloud droplet concentration is decreasing. Detraining of cloud droplets is one reason for the decreasing number of cloud droplets with height. Another reason for the reduction of the number of cloud droplets with height is the collision of cloud droplets and the following coalescence forming a new and larger cloud droplet.

The process of coagulation is more effective for larger cloud droplets. This can be

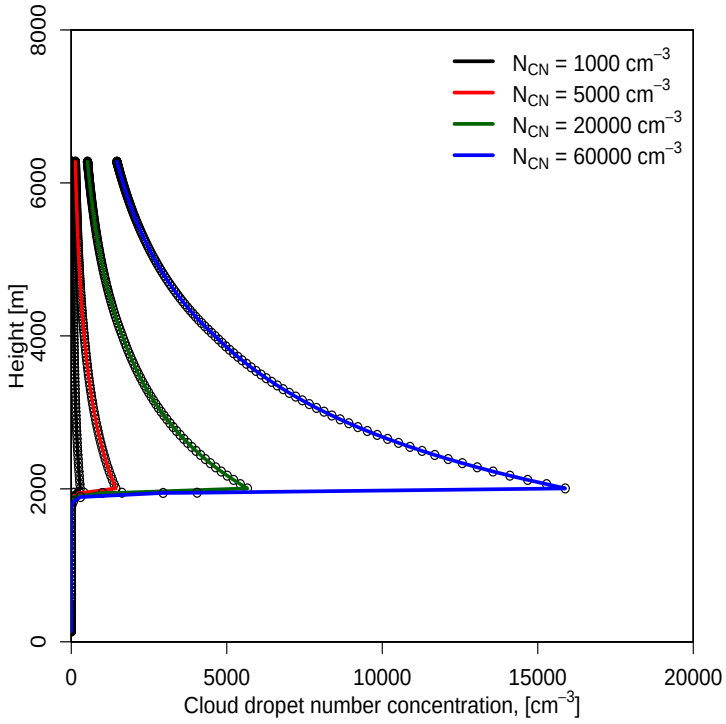

Figure 3.3: *Vertical profiles of the cloud droplet number concentration* (cm^{-3}) *for fire-emitted aerosol concentration of (black)* $N_{CN} = 1000\,\mathrm{cm}^{-3}$, *(red)* $N_{CN} = 5000\,\mathrm{cm}^{-3}$, *(green)* $N_{CN} = 20000\,\mathrm{cm}^{-3}$ *and (blue)* $N_{CN} = 60000\,\mathrm{cm}^{-3}$.

nicely seen in Fig. 3.4, where the evolution of the cloud droplet size distribution with height is shown for clean ($N_{CN} = 1000\,\mathrm{cm}^{-3}$), intermediate ($N_{CN} = 20000\,\mathrm{cm}^{-3}$) and strongly polluted ($N_{CN} = 60000\,\mathrm{cm}^{-3}$) conditions. It can be seen that the cloud droplet size distribution is broadening with height. For the clean case the largest particles have a diameter of about 30 μm in the vicinity of the cloud base. During the ascent of the air parcel the cloud droplets are growing and the largest droplets are around 90 μm near the top of the cloud.

In the intermediate case the spectrum broadening is strongly reduced compared to the clean case. At the cloud base the largest droplets are around 10 μm and at the top of the cloud around 40 μm. This behaviour is also visible in the strongly polluted case, where the spectrum broadening is even more reduced. Because of the high number concentration of the cloud droplets the sizes at the cloud base are the smallest from all three cases (8 μm) and grow only to around 30 μm at the cloud

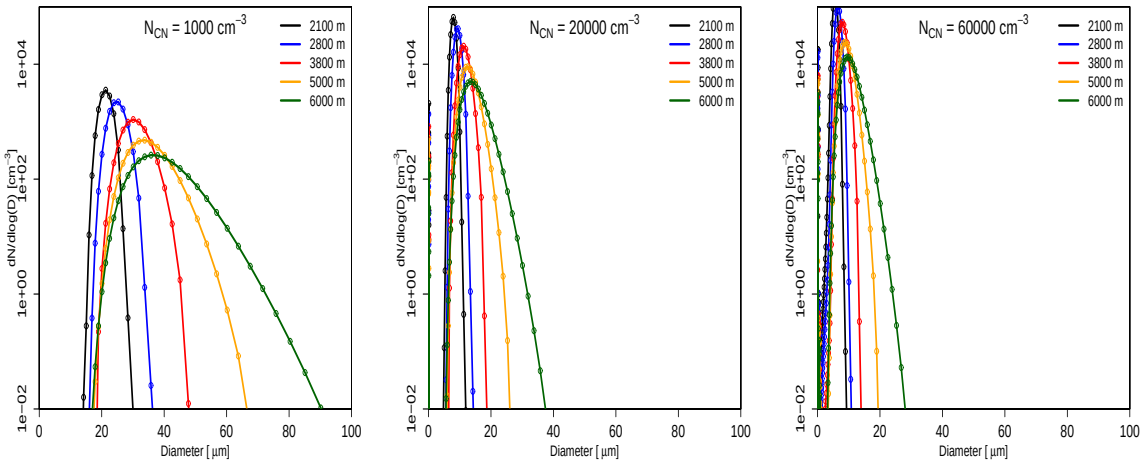

Figure 3.4: *Developing number size distributions of cloud droplets with height for (left) an aerosol concentration of* $N_{CN} = 1000\,\mathrm{cm}^{-3}$*, (center)* $N_{CN} = 20000\,\mathrm{cm}^{-3}$ *and (right)* $N_{CN} = 60000\,\mathrm{cm}^{-3}$*. The different colors denote different heights, namely (black)* 2100 m*, (blue)* 2800 m*, (red)* 3800 m*, (orange)* 5000 m *and (green)* 6000 m*.*

top. This reduced spectrum broadening with increasing aerosol concentration is also reported from measurements (Andreae et al. (2001)). This has also been modeled by Diehl et al. (2007). However, they showed this spectrum broadening only for aerosol number concentrations up to $N_{CN} = 10000\,\mathrm{cm}^{-3}$ and for hazy atmospheric conditions during the biomass burning season in Indonesia. In contrast, the results of this chapter are obtained with higher aerosol number concentrations (up to $N_{CN} = 60000\,\mathrm{cm}^{-3}$) and with the extreme dynamical conditions in the updraft region of a pyro-convective cloud. Therefore, compared to the more simplified bulk microphysics in the 3D model, the new model approach introduced in this chapter is a useful tool for the detailed investigation of the microphysical processes in intense dynamical regions of pyro-convective clouds.

Note that in this case the cloud reached temperatures below 0° C (cloud top temperature −7° C) but no freezing of cloud droplets occurred, because the available aerosol particles start to act as ice nuclei (IN) at lower temperatures. These warm clouds play an important role during the biomass burning season when the ambient atmosphere inhibits the evolution of deep pyro-convective clouds, because they transport the aerosol particles to the middle troposphere. However, Diehl et al. (2007) showed with parcel model studies the strong influence of the IN efficiency on the updraft region of deep convective clouds forming in regions of intense biomass burning. Very efficient IN, e. g., biological particles, lead to an earlier and stronger latent heat release by freezing, which leads to a stronger updraft region. In Chapter 4.5.1 the influence of the IN

efficiency on pyro-convective clouds is investigated with 2D simulations.

3.4 Conclusions

In this chapter a newly developed model approach was presented where a parcel model with detailed spectral microphysics was run along an ascending trajectory derived from 3D model output.

It was shown that the number of cloud droplets within the updraft region of a pyro-convective cloud is increasing with increasing aerosol concentration. On the other hand, the size of the cloud droplets is decreasing with increasing aerosol concentration. Also, the growth to larger particles (spectrum broadening) is reduced when the aerosol concentration is increased. These results are in agreement with measurements. Therefore, this new model approach is a useful tool to study the development of size distributions within the intense updraft region of a pyro-convective cloud.

Chapter 4

Dynamical and microphysical interactions in pyro-convective clouds

4.1 Introduction

In Chapter 2 the dependency of the cloud droplet number concentration on the aerosol particle concentration, size and hygroscopicity at the cloud base was investigated. Chapter 3 showed that the size and the number of cloud droplets are changing with height. However, the effects of turbulence and formation of precipitation by recirculating particles are not covered by the previous studies using a dynamically simple parcel model. Therefore, the active tracer high resolution atmospheric model (ATHAM) is used now to study the influence of the aerosol particle concentration on a pyro-convective cloud taking all microphysical and dynamical processes into account.

In this Chapter the sensitivity of a pyro-convective cloud on the aerosol concentration for a mid-latitude atmospheric profile is investigated. Also, the influence of the ice nucleation ability on the evolution of the pyro-convective cloud is analyzed. Further sensitivity studies deal with the structure of the atmospheric profile and the influence of the sensible heat release by the fire.

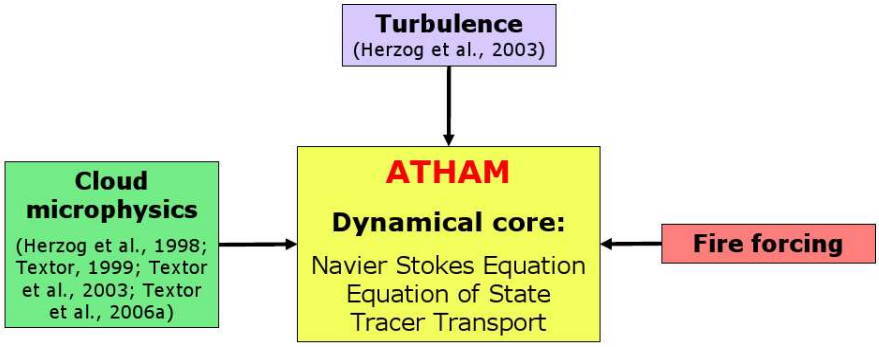

Figure 4.1: *Modular structure of the actvice tracer high resolution model ATHAM (after Luderer (2007)).*

4.2 Model description

The three-dimensional model ATHAM is able to simulate intense forms of atmospheric convection induced by volcanic eruptions or intense forest fires (Oberhuber et al. (1998), Graf et al. (1999), Herzog et al. (1998), Herzog et al. (2003)) and solves the complete Navier-Stokes equations including sound waves, which cannot be excluded due to possible supersonic flow around the vent of a volcano. The model also comprises the equations for tracer advection as well as the thermo- and hydrodynamic equations. These equations are solved with an implicit time stepping scheme on a staggered Arakawa C grid (Arakawa and Lamb (1977)). This grid allows stretching for the use of a higher spatial resolution in regions where strong gradients can occur, e. g., in the vicinity of the fire. This dynamical core of ATHAM takes the effects of active tracers into account. An active tracer in this framework is defined as a component that affects the density, heat capacity and the compressibility of the air in the model. In this studies, all hydrometeors as well as the aerosol particles are treated as active tracers. For the representation of sub-grid processes a prognostic turbulence scheme was implemented into ATHAM (Herzog et al. (2003)), which allows to differentiate between horizontal and vertical turbulent exchange processes when anisotropy in turbulence cannot be ignored.

The modular structure of ATHAM allows the inclusion of different and independent modules. From the existing pool of modules, namely dynamics, transport, turbulence, fire forcing, cloud microphysics, gas scavenging, radiation and chemistry, the first five have been used.

4.2.1 One- and two-moment schemes

The key point in this work is the interaction of the emitted smoke by biomass burning events with cloud microphysics. Until now, two different microphysical schemes are implemented into ATHAM: a one-moment Kessler scheme (Herzog et al. (1998)) and a two-moment scheme (Textor (1999), Textor et al. (2003), Textor et al. (2006)).

For studies of the microphysical evolution of clouds it would be desirable to have a spectral formulation similar to the cloud parcel model of Chapter 2. The disadvantage of this method is the high computational effort. Therefore a simplified description of the microphysical processes in form of a bulk parameterization is used in most two- and three-dimensional numerical models.

The first attempt to simplify the numerical description of clouds was done by Kessler (1969). In this warm cloud scheme it was distinguished for the first time between cloud and rain droplets. This approach made it possible to formulate different processes within and between these two classes in terms of time rates of mass density changes. Therefore, for every model time step, it is known how much water is transferred from one class to the other. The mass density is defined as the first moment of the number density size distribution function of droplets $f_w(x)$ with $k = 1$

$$M_w^k = \int_0^\infty x^k f_w(x) \mathrm{d}x, \tag{4.1}$$

where x denotes the particle mass. Because only one moment is used in this approach, it is often referred to as a *one-moment scheme*. In this framework the mean radius is unknown because of the missing information about the number concentration.

This can be avoided by additionally using the zeroth moment of the number density size distribution function of droplets $f_w(x)$ with $k = 0$ (see eq. 4.1). Such schemes are called *two-moment schemes*. Then the information of the number concentration in each class is given, which also implies that additional processes have to be introduced, e.g. the coagulation within one class, which changes the number density but not the mass density. In Fig. 4.2 the relevant processes in warm clouds are shown.

4.2.2 Reason for the implementation of a new two-moment scheme in ATHAM

The question arises why there is a need for a new two-moment microphysical scheme in ATHAM. The existing two-moment scheme was specially designed for volcanic eruptions with ash particles that are mostly of super-micron size and have been found to

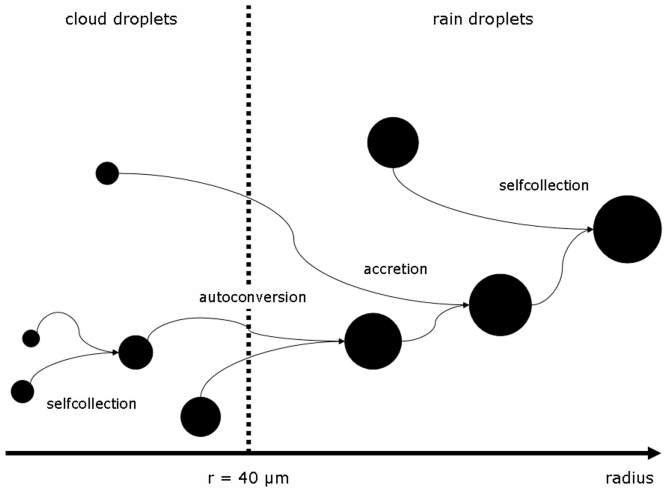

Figure 4.2: *Warm cloud microphysical processes in the framework of a two-moment scheme (after Seifert (2002)).*

be often coated with a layer of soluble salts (high κ values, see Chapter 2), which lowers the critical diameter (Textor (1999), Textor et al. (2003), Textor et al. (2006)). In contrast, for biomass burning events it is assumed that mostly small particles in the sub-micron range are emitted with a low to medium hygroscopicity. Also, in the existing two-moment scheme interactions of particles inside one class are ignored. This means that no selfcollection processes are taken into account, which is in strong contrast to the conceptual picture of the microphysical structure of clouds forming over biomass burning areas. In such polluted clouds the high number of emitted smoke particles produce a high number of small cloud droplets. In order to form rain droplets the selfcollection in the cloud droplet class plays an important role and can not be neglected.

Because of this situation a new two-moment scheme developed by Axel Seifert (Seifert (2002)), henceforth called *Seifert scheme*, has been implemented to study the interplay between aerosol particles and cloud microphysics.

4.3 Two-moment cloud microphysics parameterization

The two-moment Seifert scheme is a parameterization for microphysical processes within mixed-phase clouds, especially for mid-latitude deep convective clouds. It com-

prises the hydrometeor categories cloud water, rain water, cloud ice, snow, graupel and in the latest version also hail. For a detailed description of this scheme see Seifert (2002) and Seifert and Beheng (2006a).

Figure 4.3 shows a simplified schematic diagram of the interactions between the hydrometeor categories that have to be taken into account in order to represent the full microphysical evolution of a cloud.

4.3.1 Nucleation

The process in the Seifert scheme that connects the results from the activation study in Chapter 2 with ATHAM is the *nucleation*. The transition from water vapor to the cloud droplet category in the Seifert scheme is done by a lookup-table. This lookup-table is based on the results from Fig. 2.4, which are based on an aerosol size distribution with a mean diameter of 120nm, a geometric standard deviation of $\sigma_g = 1.5$ and an effective hygroscopicity parameter of 0.2 (see Section 2.3.1). In the version of the Seifert scheme that is implemented in the weather prediction model COSMO, a lookup-table based on the results of Segal and Khain (2006) is implemented.

The requested parameters for the lookup-table are the updraft velocity w and the number of aerosol particles N_{CN}. Therefore for each grid point at the cloud base the updraft velocity is estimated. The cloud base is detected when following criteria are fulfilled: (1) the updraft velocity w has to be larger than $0.1\,\mathrm{m\,s^{-1}}$, the supersaturation S has to be larger than $0\,\%$ and the maximum supersaturation at the lower model level has to be smaller than the actual supersaturation. Most likely this updraft velocity is not the exact value used in the lookup-table, hence a linear interpolation is conducted. The interpolation shows better results with an increasing number of elements in the table. In the model version used for these studies, the lookup-table has entries for nine updraft velocities (1, 2.5, 5, 7, 10, 12, 15, 17 and $20\,\mathrm{m\,s^{-1}}$).

For the evaluation of the aerosol particle concentration N_{CN} two different approaches can be used. The first and simple approach is to use a fixed value of N_{CN} for all grid points where the nucleation is calculated. The advantage of this method is that an exact number of N_{CN} can be prescribed, which is useful for example for sensitivity studies. The disadvantage of this approach is that the natural variability of the aerosol concentration due to the transport within the updraft region can not be considered.

In contrast, the second and more sophisticated approach calculates the aerosol number concentration of the emitted smoke from the fire. At each grid point, where

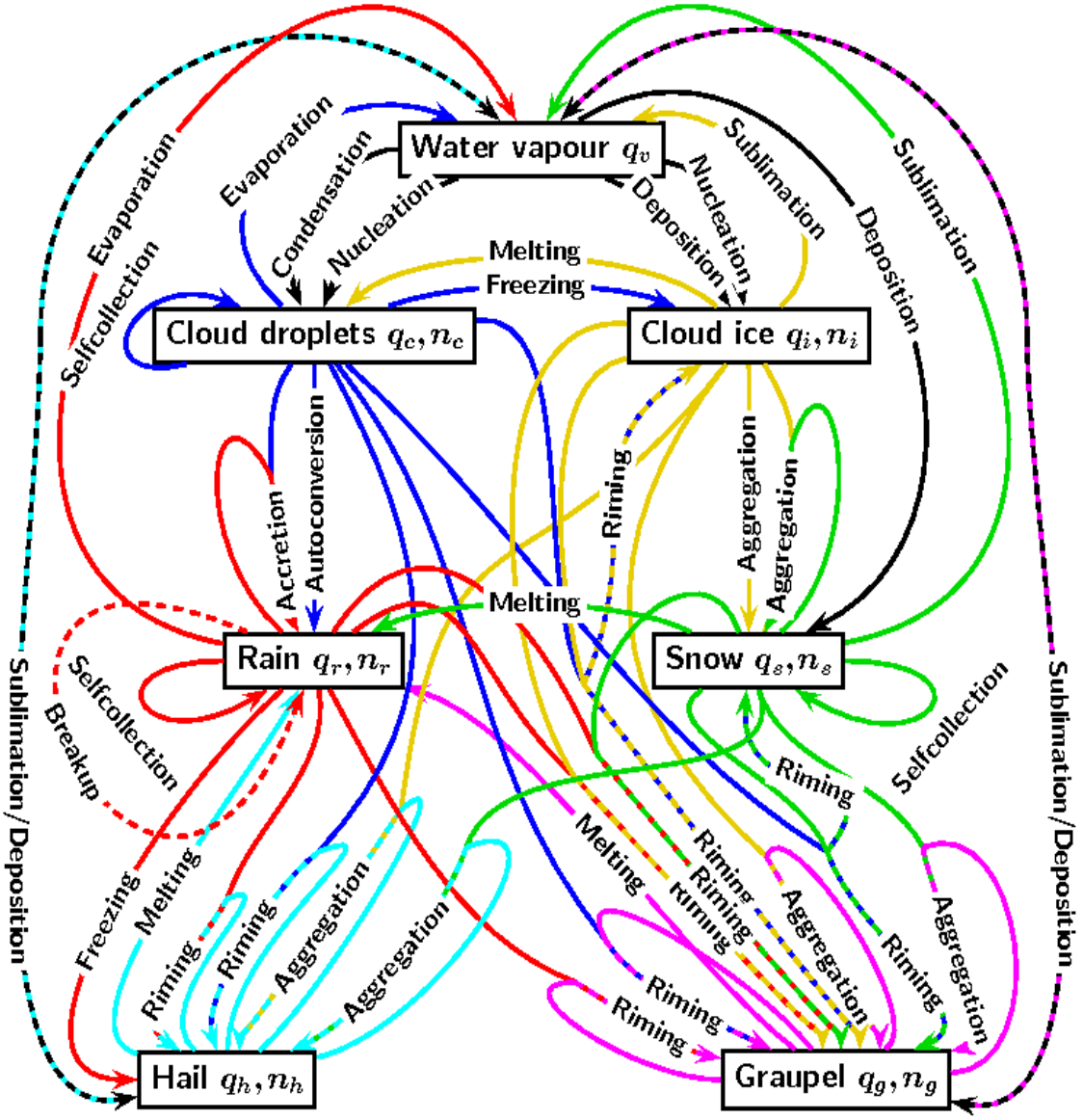

Figure 4.3: *Simplified schematic diagram of the microphysical interactions in the two-moment Seifert scheme with respect to the particle classes cloud- and rain droplets, cloud ice, snow, graupel and hail (from U. Blahak, private communication).*

nucleation comes into play, the aerosol concentration is defined as

$$N_{CN} = M_{smoke} \left(\frac{\pi}{6} \frac{\rho_{aerosol}}{\rho_{air}} D^3 exp\left(\frac{9}{2} \sigma^2 \right) \right)^{-1}, \tag{4.2}$$

with M_{smoke} the mass of the emitted aerosol by the fire, $\rho_{aerosol}$ the density of the emitted aerosol , ρ_{air} the density of the surrounding air, D the mean diameter and σ the geometric standard deviation of the emitted aerosol distribution. For the consistency of the results it is important that the values of the mean diameter and the geometric standard deviation are the same for both the calculation of the number concentration and the lookup-table. Again, it is most likely that the calculated aerosol concentration does not match with one of the values of the lookup-table. Therefore, a linear interpolation is conducted, as it is done in the case of the updraft velocity. The lookup-table has eleven elements for the aerosol concentration (200, 400, 800, 1000, 5000, 10000, 20000, 40000, 60000, 80000 and 100000 cm^{-3}).

Figure 4.4 shows a schematic diagram of the procedure of using the lookup-table for the case of the calculated aerosol concentration through the aerosol mass. With the use of the lookup-table, ATHAM is now able to determine the number of cloud droplets that are activated at the cloud base.

The fact that the cloud parcel model can be used to calculate lookup-tables with different aerosol properties provides the possibility for a novel and potentially powerful combination of the cloud parcel model and ATHAM. It is now possible to investigate the influence of different kinds of biomass burning events, ranging from small savannah fires with higher κ values to intense boreal forest fires with lower κ values but higher emissions of aerosol, heat and water vapor, on the dynamical and microphysical evolution of pyro-clouds.

4.3.2 Other parameterized microphysical processes

Here, a brief overview on the other microphysical processes in the Seifert scheme is given. For a detailed description see Seifert (2002) and Seifert and Beheng (2006a).

- **Condensation / evaporation of cloud droplets:**
  The condensational growth is realized by saturation adjustment. This adjustment is done at the end of each time step, after calculating all other microphysical processes. The remaining supersaturation is then added to the cloud droplet

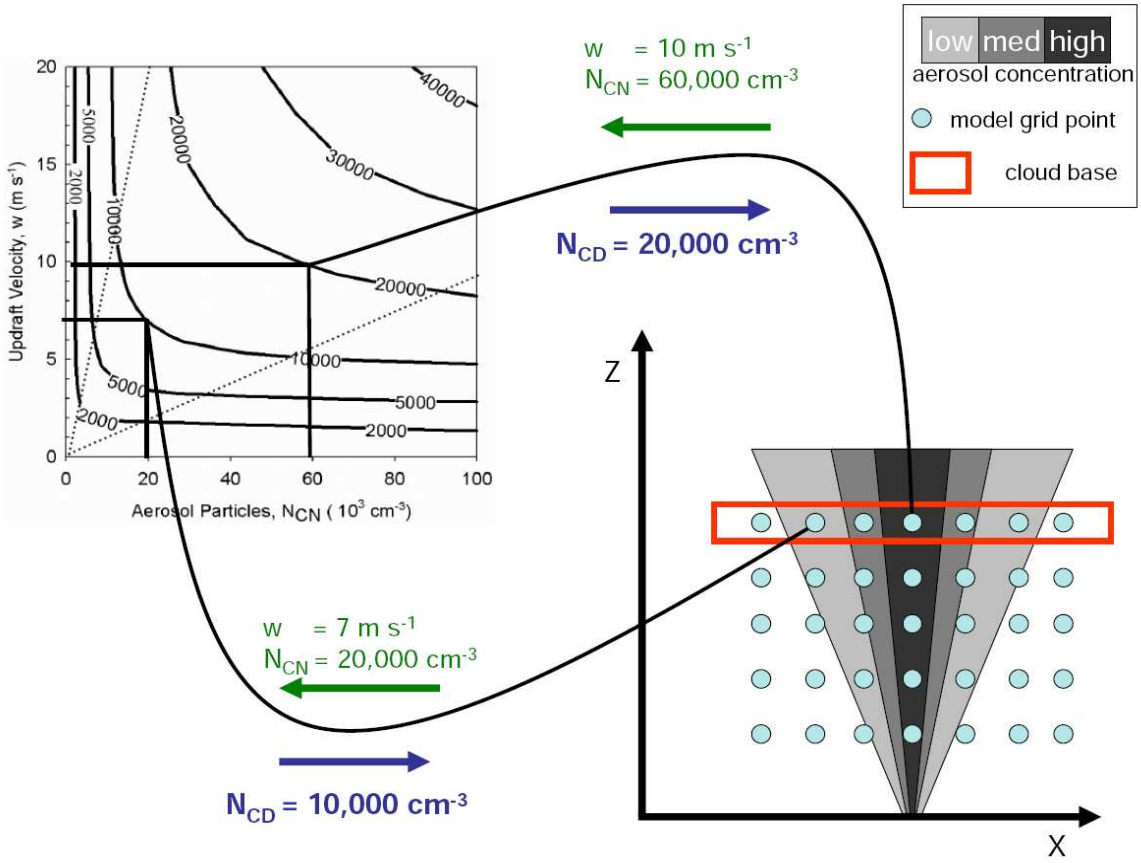

Figure 4.4: *Schematic diagram of the implementation of the lookup-table. In the lower right the schematic model domain of ATHAM including the model grip points (circles) is shown. The grey-shaded areas show different aerosol concentrations of the smoke plume and the grid points within the red box are representing the cloud base. In the upper left the results from the activation studies (see Chapter 2, Fig. 2.4) can be seen. The green arrows denotes the parameters needed for the evaluation of the nucleated cloud droplets with exemplary values of* $w = 10\,\mathrm{m\,s^{-1}}$ *and an aerosol concentration of* $N_{CN} = 60000\,\mathrm{cm^{-3}}$ *in the center of the updraft region and* $w = 7\,\mathrm{m\,s^{-1}}$ *and an aerosol concentration of* $N_{CN} = 20000\,\mathrm{cm^{-3}}$ *in the exterior part of the plume. In blue the cloud droplet concentration, obtained from the lookup-table are shown:* $N_{CD} = 20000\,\mathrm{cm^{-3}}$ *for the more polluted part in the center of the plume and* $N_{CD} = 10000\,\mathrm{cm^{-3}}$ *in the exterior part of the updraft region.*

class. If in contrast subsaturation occurs the cloud droplets are evaporated until a relative humidity of 100 % is reached.

- **Evaporation of rain droplets:**
  The evaporation of rain droplets depends on the size of their rain droplet, its terminal velocity, the Reynolds number and the ventilation factor.

- **Deposition:**
  This process describes the effect of growth of cloud ice, snow, graupel and hail by water vapor deposition and is calculated by a general growth equation.

- **Selfcollection, autoconversion and accretion (aggregation)**
  Selfcollection denotes the process when two particles of the same class form a new larger droplet which remains in the same class that leads to a change in the number concentration of this class. If two cloud droplets form a rain droplet the term autoconversion is used. When a cloud and a rain droplet (snow and cloud ice particle) form a larger rain droplet (snow particle) the term accretion (aggregation) is used.

  For all these processes the particles first have to collide and then stick together (coalescence). This process is called coagulation. For particles with the same size, the collision efficency is reduced due to the same terminal velocity. Hence, the coagulation efficiency is also reduced.

- **Sublimation:**
  This term denotes the process of the transition of water from the solid phase to the gas phase.

- **Freezing:**
  The freezing of water drops is based on a stochastical model by Bigg (1953) using ice nucleation abilities $B_{h,i}$ ($B_{h,i} = 0$ for homogeneous freezing as it is set in the research model WRF, $B_{h,i} = 1 \cdot 10^{-1}\,\mathrm{cm}^{-3}$ for leaf litter as ice nuclei). The homogeneous freezing of rain droplets is not implemented, since rain droplets freeze rapidly by heterogenous freezing before they reach the level of homogeneous freezing.

- **Melting:**
  The melting of all ice particle classes is treated in the same way. Evaporation from the liquid surface is then calculated for a temperature of $T = 273.16\,\mathrm{K}$.

4.3.3 Plausibility test with the implemented lookup-table

After the implementation of the new lookup-table with the data from Chapter 2 first model runs have been conducted to validate the implementation. Therefore, two different cases are considered, a clean case with an aerosol concentration of $N_{CN} = 500\,\mathrm{cm}^{-3}$ and a polluted case with an aerosol concentration of $N_{CN} = 500000\,\mathrm{cm}^{-3}$. The 2D model runs were initialized for a domain with a horizontal dimension of 20000 m realized by 150 grid points and a vertical extension of 25000 m realized by 80 grid points. The fire forcing was set to $9\,\mathrm{kg\,m}^{-2}$ biomass burned with a combustion heat of $1.87 \cdot 10^7\,\mathrm{J\,kg}^{-1}$.

Figures 4.5 and 4.6 show the liquid water content after ten minutes of model integration for the clean and the polluted case, respectively. The first supersaturated grid point was found after 4 minutes for this setting. It can be clearly seen that the cloud water content is distributed almost identically for the two cases. This is expected because the amount of liquid water in a cloud at this stage is independent of the number of CCN. The existing supersaturation is reduced by condensation on the available particles, which leads to a difference in the cloud droplet concentration but not in the liquid water mass.

The difference in the cloud droplet number concentration for the clean and the polluted case is shown in Figs. 4.7 and 4.8, respectively. Note that the color coding differs for the two plots. It can be clearly seen that the number concentration of cloud droplets is lower for the clean case compared to the polluted case. Interestingly, the number of CCN differs by two orders of magnitude ($N_{CN} = 500\,\mathrm{cm}^{-3}$ against $N_{CN} = 50000\,\mathrm{cm}^{-3}$) while the maximum cloud droplet concentration only differs by one order of magnitude ($N_{CD} = 500\,\mathrm{cm}^{-3}$ against $N_{CD} = 5500\,\mathrm{cm}^{-3}$). The fact that in some areas of the clean cloud the number of cloud droplets exceeds the amount of aerosol particles (see Fig. 4.7) is due to transport of particles by turbulence.

Figure 4.9 shows the amount of rain water for the clean cloud, while Fig. 4.10 presents the amount of rain water for the polluted cloud. The comparison of these results shows distinct differences (note the different scales of the color coding). In the clean case the rain water content reaches values up to $0.12\,\mathrm{g\,kg}^{-1}$ whereas in the polluted case the maximum value is only about $2 \cdot 10^{-5}\,\mathrm{g\,kg}^{-1}$. This is expected because the high number concentration of aerosol particles and hence the high number concentration of cloud droplets is suppressing the rain forming processes. Due to the large number of equally small cloud droplets the probability of colliding with another

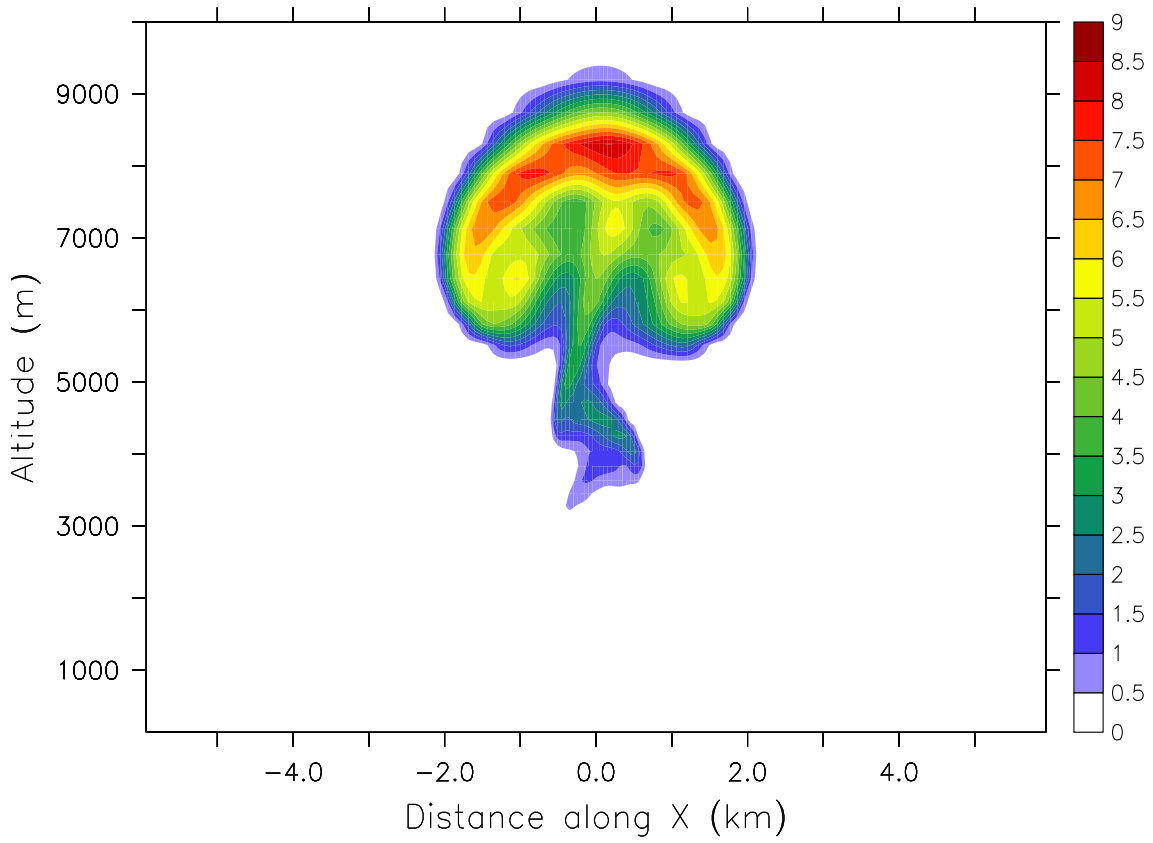

Figure 4.5: *X-Z cross section of the liquid water content in* $\mathrm{g\,kg^{-1}}$ *calculated with the Seifert scheme for clean conditions with* $N_{CN} = 500\,\mathrm{cm^{-3}}$.

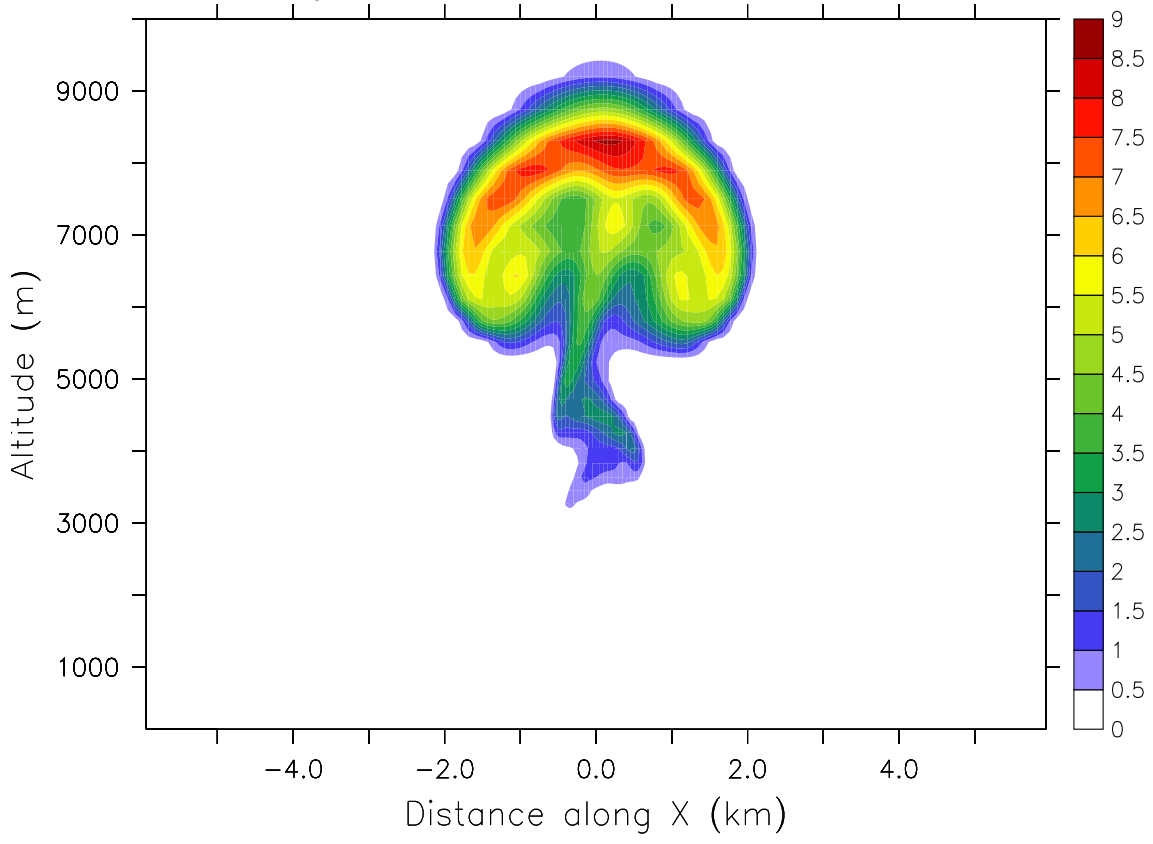

Figure 4.6: *X-Z cross section of the liquid water content in* $\mathrm{g\,kg^{-1}}$ *calculated with the Seifert scheme for polluted conditions with* $N_{CN} = 50000\,\mathrm{cm^{-3}}$.

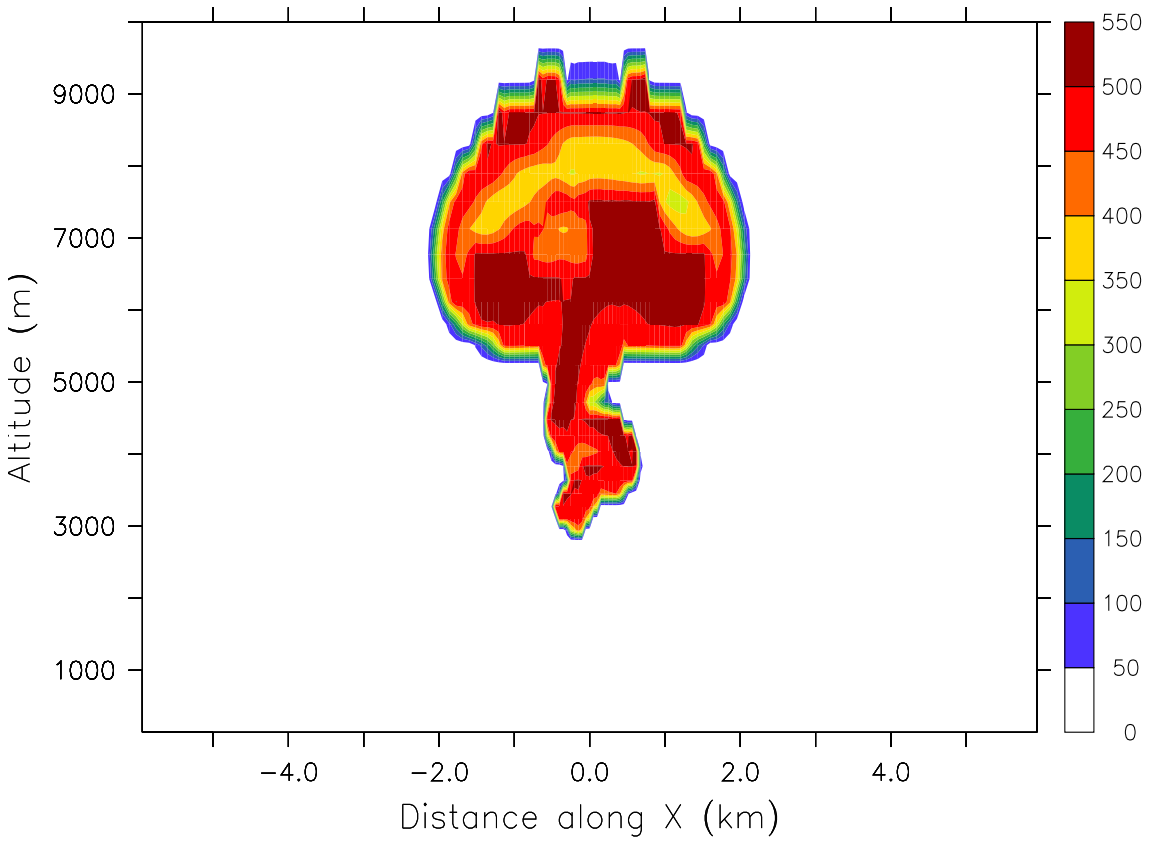

Figure 4.7: *X-Z cross section of the cloud droplet number concentration in* cm^{-3} *calculated with the Seifert scheme for clean conditions with* $N_{CN} = 500\,\mathrm{cm}^{-3}$.

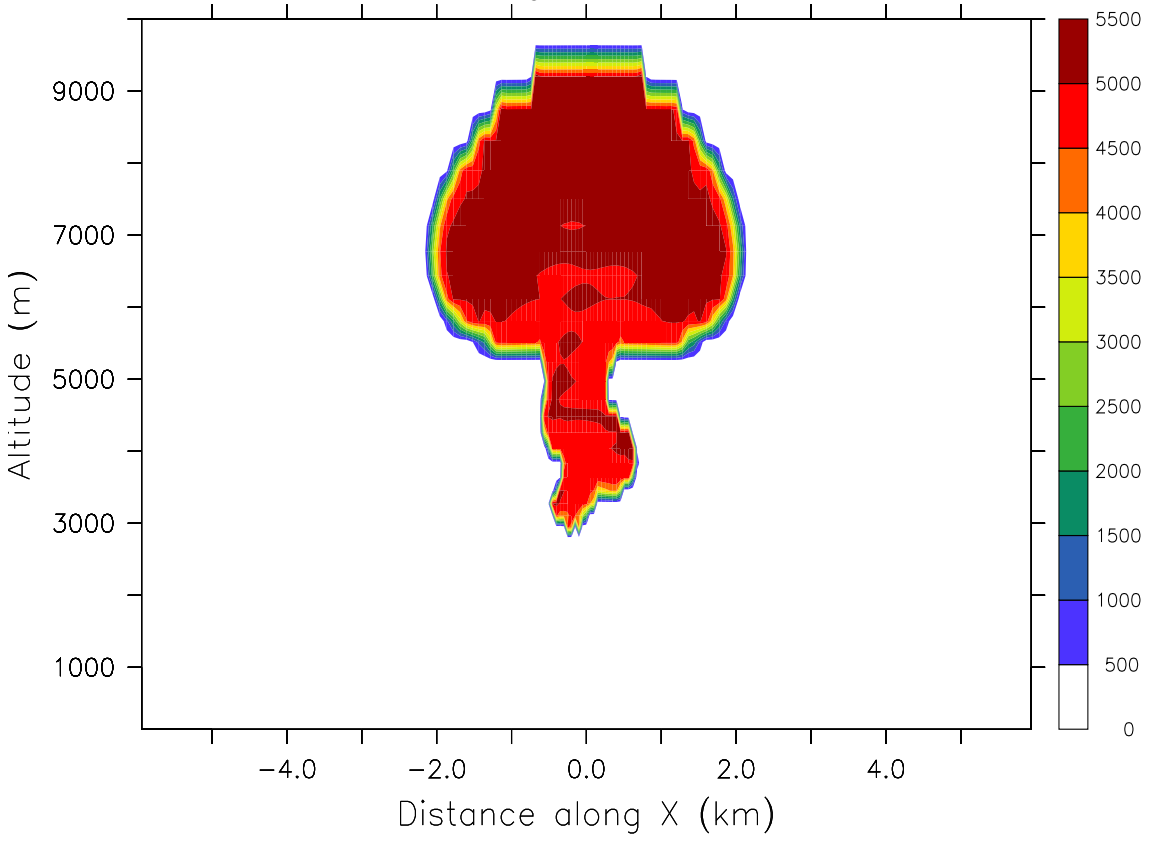

Figure 4.8: *X-Z cross section of the cloud droplet number concentration in* cm^{-3} *calculated with the Seifert scheme for polluted conditions with* $N_{CN} = 50000\,\mathrm{cm}^{-3}$.

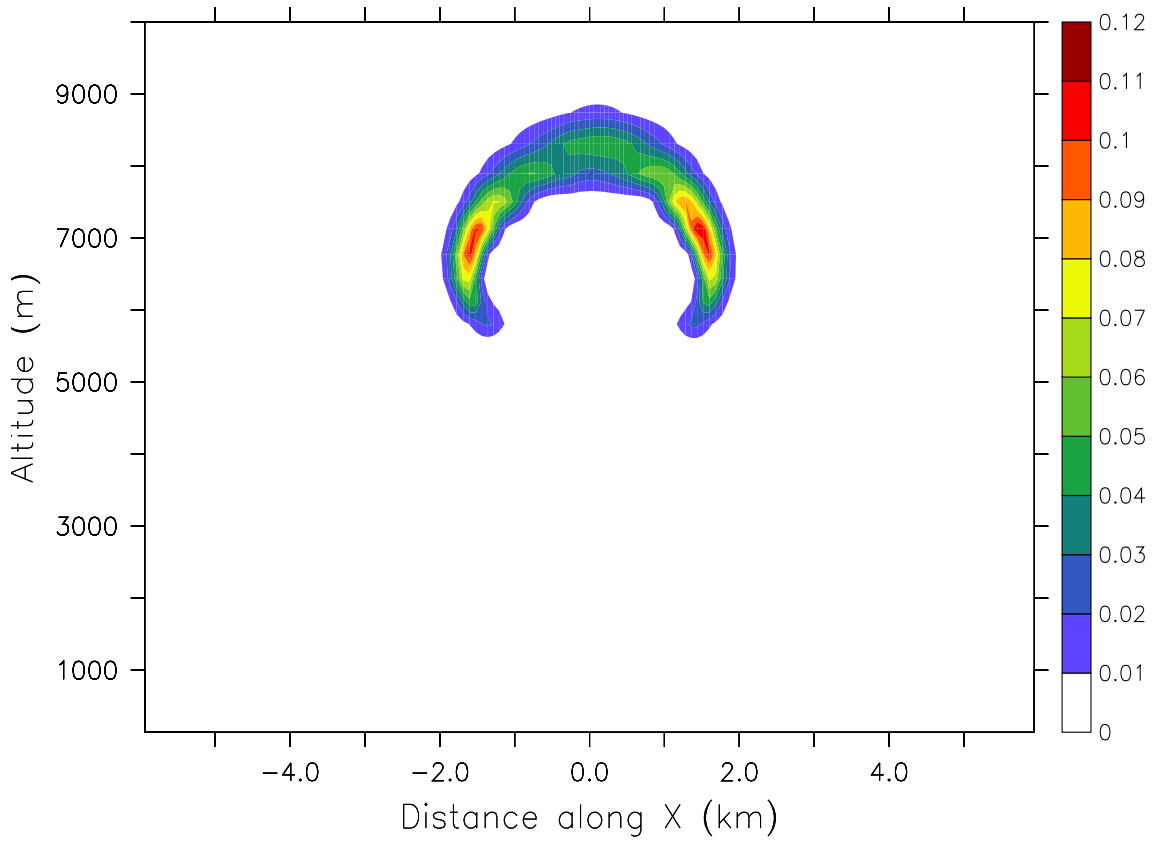

Figure 4.9: *X-Z cross section of the rain water content in* $\mathrm{g\,kg^{-1}}$ *calculated with the Seifert scheme for clean conditions with* $N_{CN} = 500\,\mathrm{cm^{-3}}$.

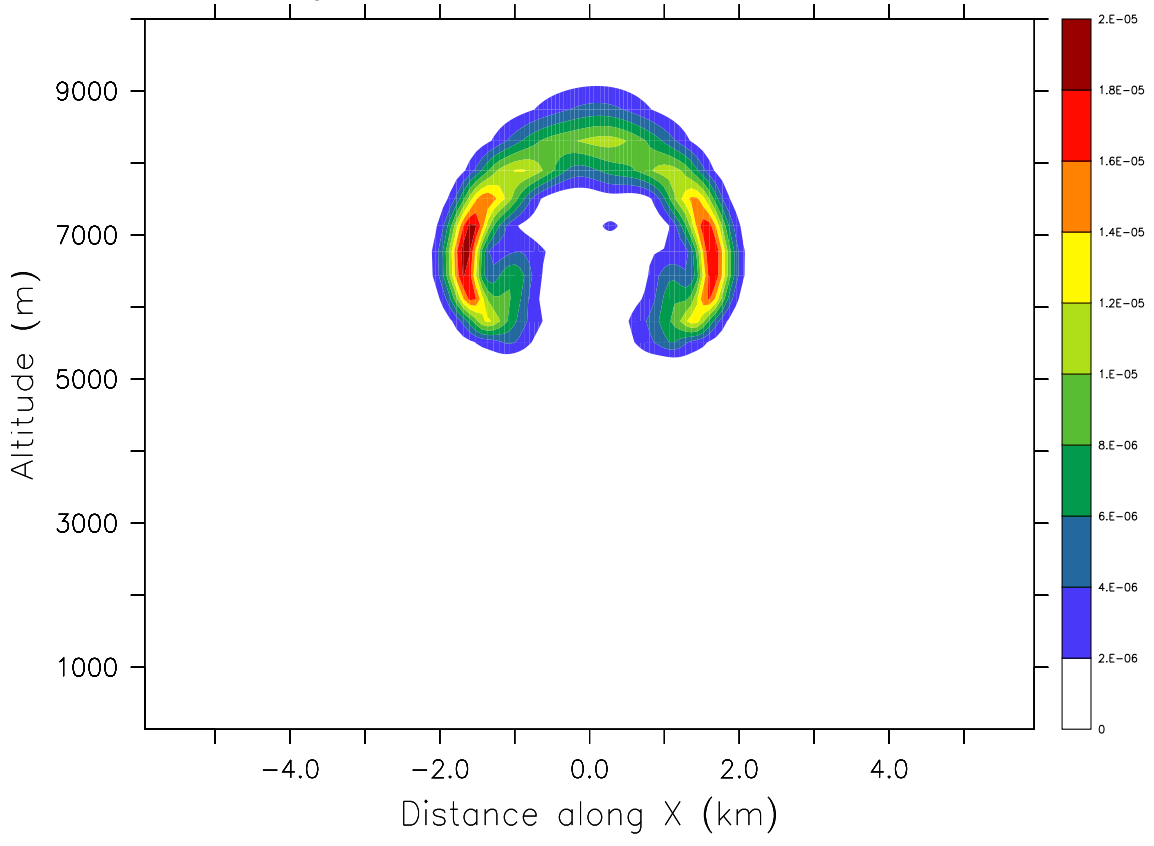

Figure 4.10: *X-Z cross section of the rain water content in* $\mathrm{g\,kg^{-1}}$ *calculated with the Seifert scheme for polluted conditions with* $N_{CN} = 50000\,\mathrm{cm^{-3}}$.

cloud particle is relatively low. Because all cloud droplets have almost the same fall velocity, the velocity relative to each other is almost zero and hence collisions are very rare. Since the effects of collision and coalescence are the governing factors for the formation of rain droplets, the rain water content is drastically lower in the polluted case compared to the clean case.

4.4 2D simulations of the influence of aerosol concentration

In this section the effect of changing the aerosol concentration on the dynamical and microphysical evolution of a pyro-cloud originating over an idealized fire is investigated using ATHAM simulations. The look-up table approach is used to describe the activation of aerosol particles (see Section 4.3). Due to the high computational costs of 3D simulations the following sensitivity studies are conducted with a 2D setup of ATHAM. Nevertheless, in Section 4.6 3D simulations are presented to support the findings of the 2D simulations.

4.4.1 Model setup

The 2D model runs were initialized with a mid-latitude US standard atmosphere (see Fig. 4.25 left). The model domain was set to 40 km x 20 km with 110 x 55 grid boxes in the x-z-directions, respectively. The minimum horizontal grid box size was set to 50 m and the minimum vertical grid box size to 100 m. Due to the stretched grid, the size of the grid boxes increases towards the borders of the model domain.

The length of the fire front was set to 300 m. The energy release from the fire was calculated based on a fuel loading of $4.5\,\mathrm{kg\,m^{-2}}$ and a value of $18700\,\mathrm{kJ\,kg^{-1}}$ for the heat combustion. This converts to a fire forcing of $378\,\mathrm{kW\,m^{-2}}$.

For the following studies the aerosol number concentration was varied between $N_{CN} = 1000\,\mathrm{cm^{-3}}$ and $60000\,\mathrm{cm^{-3}}$. The variability induced by the vertical velocity is not considered. The results are discussed on the basis of three case, namely a clean case with $N_{CN} = 1000\,\mathrm{cm^{-3}}$, an intermediate case with $N_{CN} = 20000\,\mathrm{cm^{-3}}$ and a strongly polluted case with $N_{CN} = 60000\,\mathrm{cm^{-3}}$. The time step was set automatically between 0.5 s and 1.5 s in order to fulfill the Courant-Friedrichs-Levy criterion.

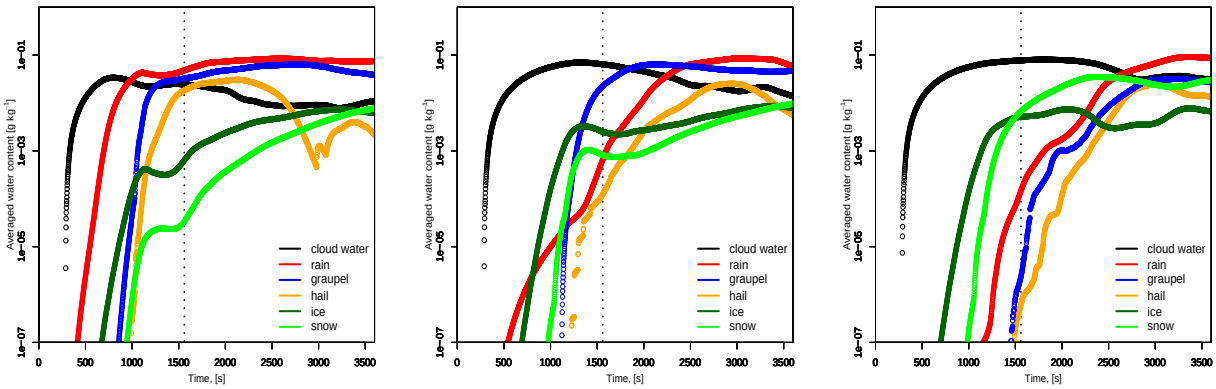

Figure 4.11: *Temporal evolution of the averaged water content in* $\mathrm{g\,kg^{-1}}$ *in the model domain for the six hydrometeor classes (black) cloud water, (red) rain water, (blue) graupel, (orange) hail, (dark green) ice and (green) snow for (left) the clean case with* $N_{CN} = 1000\,\mathrm{cm^{-3}}$*, (middle) the intermediate case with* $N_{CN} = 20000\,\mathrm{cm^{-3}}$ *and (right) the strongly polluted case with* $N_{CN} = 60000\,\mathrm{cm^{-3}}$*. The black dashed line denotes the results after 26 minutes, the time axis ends after 60 minutes.*

4.4.2 Results

Figure 4.11 shows the temporal evolution of the water content in $\mathrm{g\,kg^{-1}}$ averaged over the whole model domain for the six hydrometeor classes. This figure shows that the order of appearance of the six hydrometeor classes cloud droplets, rain, ice particles, snow, graupel and hail is different for the three cases.

In the clean case ($N_{CN} = 1000\,\mathrm{cm^{-3}}$) the formation of rain droplets by autoconversion is the first process after the activation of cloud droplets. Then cloud ice is formed, after that graupel, snow and hail are produced almost at the same time. At the end of the simulation, rain and graupel are the dominant hydrometeor classes regarding the water mass within the pyro-convective cloud, followed by snow, cloud ice and cloud water. After 60 minutes the hail water content is decreasing because it is removed from the atmosphere by precipitation.

In the intermediate case ($N_{CN} = 20000\,\mathrm{cm^{-3}}$) the activation of cloud droplets is also followed by the formation of rain droplets, but soon the ice amount exceeds the rain amount. In the following, snow, graupel and hail are formed. Compared to the clean case the amount of cloud ice and snow is larger after 26 minutes in the intermediate case, while the amount of rain is significantly lower. The graupel formation is in the same order of magnitude throughout the 60 minutes of model integration. On the other side, hail formation is delayed compared to the results of the clean case, but is decreasing again in the same way. At the end, the compositions of the clean and

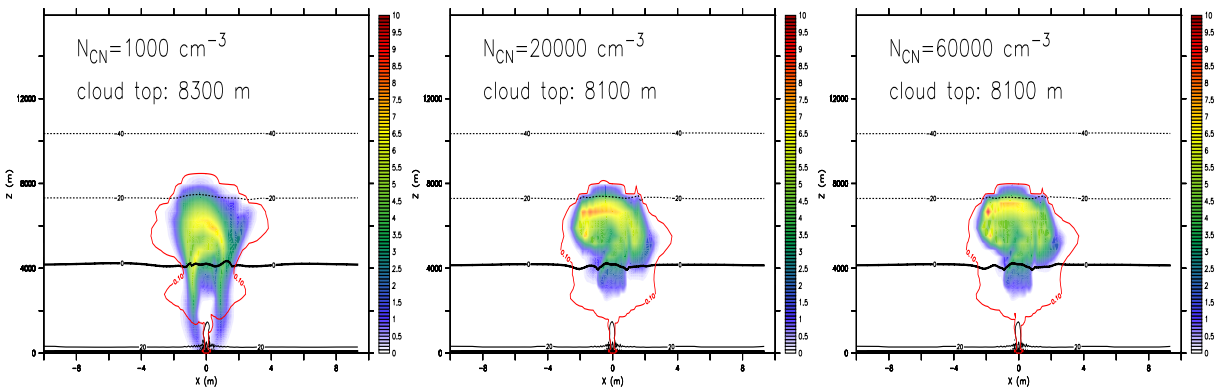

Figure 4.12: *X-Z cross section of the total hydrometeor water content after 26 minutes of the simulation in* $\mathrm{g\,kg^{-1}}$ *for (left)* $N_{CN} = 1000\,\mathrm{cm^{-3}}$*, (middle)* $N_{CN} = 20000\,\mathrm{cm^{-3}}$ *and (right)* $N_{CN} = 60000\,\mathrm{cm^{-3}}$*. The black lines denote the* 0° C, −20° C *and* −40° C *isotherms, respectively. The red line shows the* $0.1\,\mu\mathrm{g\,kg^{-1}}$ *isoline of the interstitial aerosol, which describes the shape of the smoke plume.*

intermediate polluted clouds are very similar with rain and graupel dominating the composition of the cloud.

The strongly polluted case ($N_{CN} = 60000\,\mathrm{cm^{-3}}$) shows a distinctly different behaviour. After their activation, the cloud droplets freeze and are transferred to the ice particle class. Thereafter snow is formed, which becomes the dominant hydrometeor in the developing stage of the cloud. Significant amounts of rain water are formed later compared to the previous cases and also the formation of graupel and hail is much delayed. Interestingly, at the end of the simulation the composition of the strongly polluted cloud is also very similar to the previous cases except the larger amount of hail, which was not removed, and snow.

Figure 4.11 shows that the composition of a pyro-convective cloud after 60 minutes of model integration is very similar for different aerosol emissions, but the cloud evolution takes different ways. In the following, the composition of the cloud is discussed in more detail for two time steps.

Results after 26 minutes of model simulation

Figure 4.12 shows the total hydrometeor water content after 26 minutes of model integration for the three different aerosol concentrations considered here ($N_{CN} = 1000\,\mathrm{cm^{-3}}$, $N_{CN} = 20000\,\mathrm{cm^{-3}}$ and $N_{CN} = 60000\,\mathrm{cm^{-3}}$). The results show that the aerosol concentration has a small influence on the dynamical evolution and the distribution of water within the cloud, which leads to differences of the shape of the clouds.

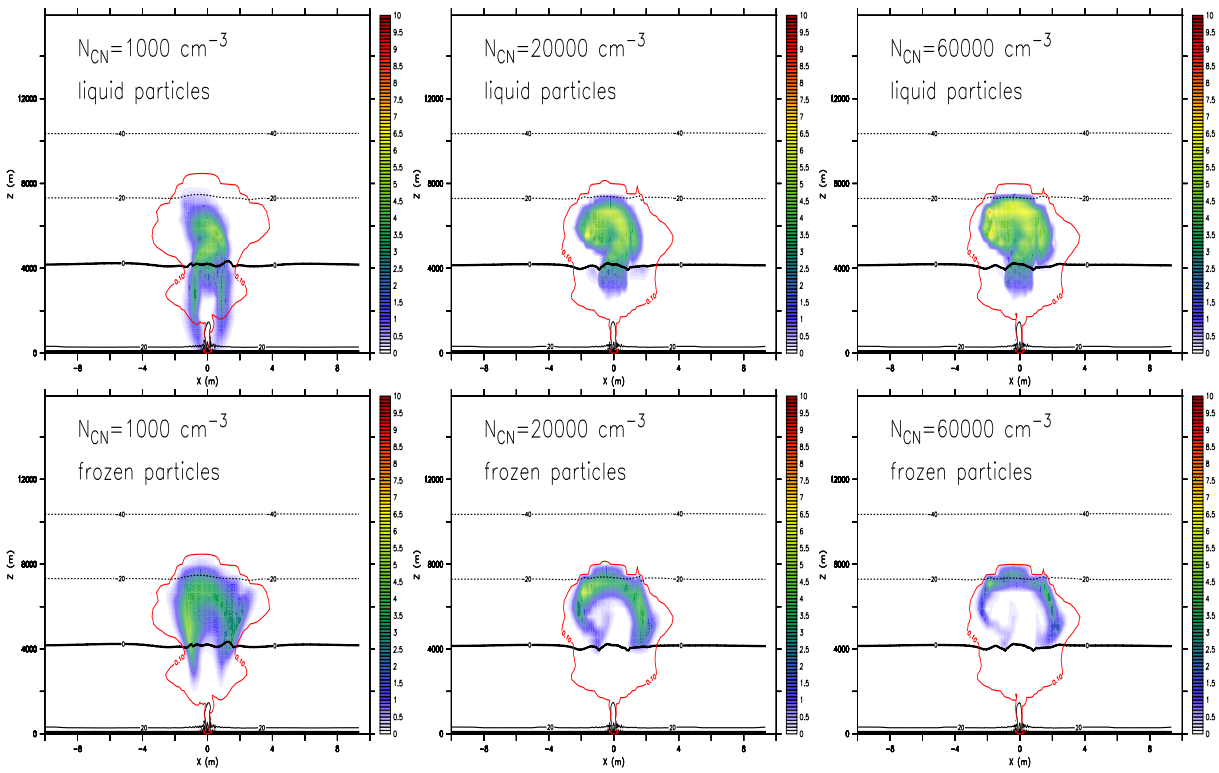

Figure 4.13: *Same as Fig. 4.12 but for (top) total liquid water content in* $\mathrm{g\,kg^{-1}}$ *and (bottom) total frozen water content in* $\mathrm{g\,kg^{-1}}$.

With increasing aerosol concentration the cloud top height is decreasing from 8300 m for $N_{CN} = 1000\,\mathrm{cm^{-3}}$ to 8100 m for $N_{CN} = 60000\,\mathrm{cm^{-3}}$. The distribution of the total hydrometeor water content is also changing with the aerosol concentration. In the case of $N_{CN} = 1000\,\mathrm{cm^{-3}}$ the maximum water content is $8\,\mathrm{g\,kg^{-1}}$, whereas the maximum water content for $N_{CN} = 60000\,\mathrm{cm^{-3}}$ is $10\,\mathrm{g\,kg^{-1}}$. The most significant difference is that in the clean case precipitating rain is already reaching the ground. In the intermediate case, the cloud is starting to precipitate indicated by the fringed area in the lower parts of the cloud, while the cloud in the strongly polluted case shows almost no signs of precipitation after 26 minutes.

In Fig. 4.13 the distribution of the liquid and frozen phase in the cloud is shown. The amount of liquid water in the cloud is increasing and the amount of frozen water is decreasing with increasing aerosol concentration. Hence, in the clean case of $N_{CN} = 1000\,\mathrm{cm^{-3}}$ significantly more water is transferred to the frozen phase compared to the highly polluted case of $N_{CN} = 60000\,\mathrm{cm^{-3}}$. This leads to more latent heat release by freezing in the clean case, which then induces a higher updraft velocity resulting

in a higher cloud top height as shown in Fig. 4.12. The deformation of the $-20°$ C isotherm shows the strength of the temperature anomalies, which induces a higher updraft velocity in the center of the cloud. Influence of particle number, size and hygroscopicity on the activation of cloud condensation nuclei (CCN)

The liquid phase in the cloud is divided into the two hydrometeor classes *cloud water* and *rain water*. The spatial distribution of these two classes is shown in Fig. 4.14. The results show that the amount of cloud water is increasing with increasing aerosol concentration. Also the maximum values of cloud water are increasing with the aerosol concentration from $4.5\,\mathrm{g\,kg^{-1}}$ in the case of $N_{CN} = 1000\,\mathrm{cm^{-3}}$ to $9\,\mathrm{g\,kg^{-1}}$ in the case of $N_{CN} = 60000\,\mathrm{cm^{-3}}$. Contrarily, the volume mean radius is strongly decreasing with increasing aerosol concentration, as expected. The high number concentration of aerosol particles in the intermediate and even more in the strongly polluted case and the high cloud base updraft velocities of around $18\,\mathrm{m\,s^{-1}}$ (not shown) lead to high concentrations of cloud droplets, which compete for a limited amount of water. Therefore, the cloud droplet radius is decreasing with increasing aerosol concentration. In the clean case ($N_{CN} = 1000\,\mathrm{cm^{-3}}$) the maximum volume mean radius is $22\,\mu$m, for the intermediate case ($N_{CN} = 20000\,\mathrm{cm^{-3}}$) the maximum radius is reduced to $10\,\mu$m and for the strongly polluted case ($N_{CN} = 60000\,\mathrm{cm^{-3}}$) the maximum radius is $5\,\mu$m.

The small cloud droplets in the intermediate and strongly polluted cases are the reason that after 26 minutes almost no rain has formed. To form warm rain two cloud droplets have to collide and form a new droplet with a radius larger than $40\,\mu$m. This process is called autoconversion (see Figs. 4.2 and 4.3). A crucial factor for the autoconversion is the collision efficiency, which describes how efficient two water droplets of certain sizes collide with each other. This efficiency is increasing with increasing droplet size, because the probability of the collision of two small droplets is very low but is increasing with droplet size (Pinsky et al. (2001)). Therefore, the ability to form larger cloud droplets and eventually rain droplets is strongly reduced in the case of higher aerosol concentrations ($N_{CN} = 20000\,\mathrm{cm^{-3}}$ and $N_{CN} = 60000\,\mathrm{cm^{-3}}$). Only in the clean case ($N_{CN} = 1000\,\mathrm{cm^{-3}}$) a significant amount of rain droplets are formed after 26 minutes. These rain droplets are already large enough to sediment out of the cloud and reach the ground.

The ice phase is divided into four classes, namely ice crystals, snow particles, graupel and hail (see Fig. 4.3). Not only the amount of frozen water is sensitive to the aerosol concentration (see Fig. 4.13), but also the composition. Figure 4.15 shows the water content for ice water, snow, graupel and hail, respectively. The ice and snow water

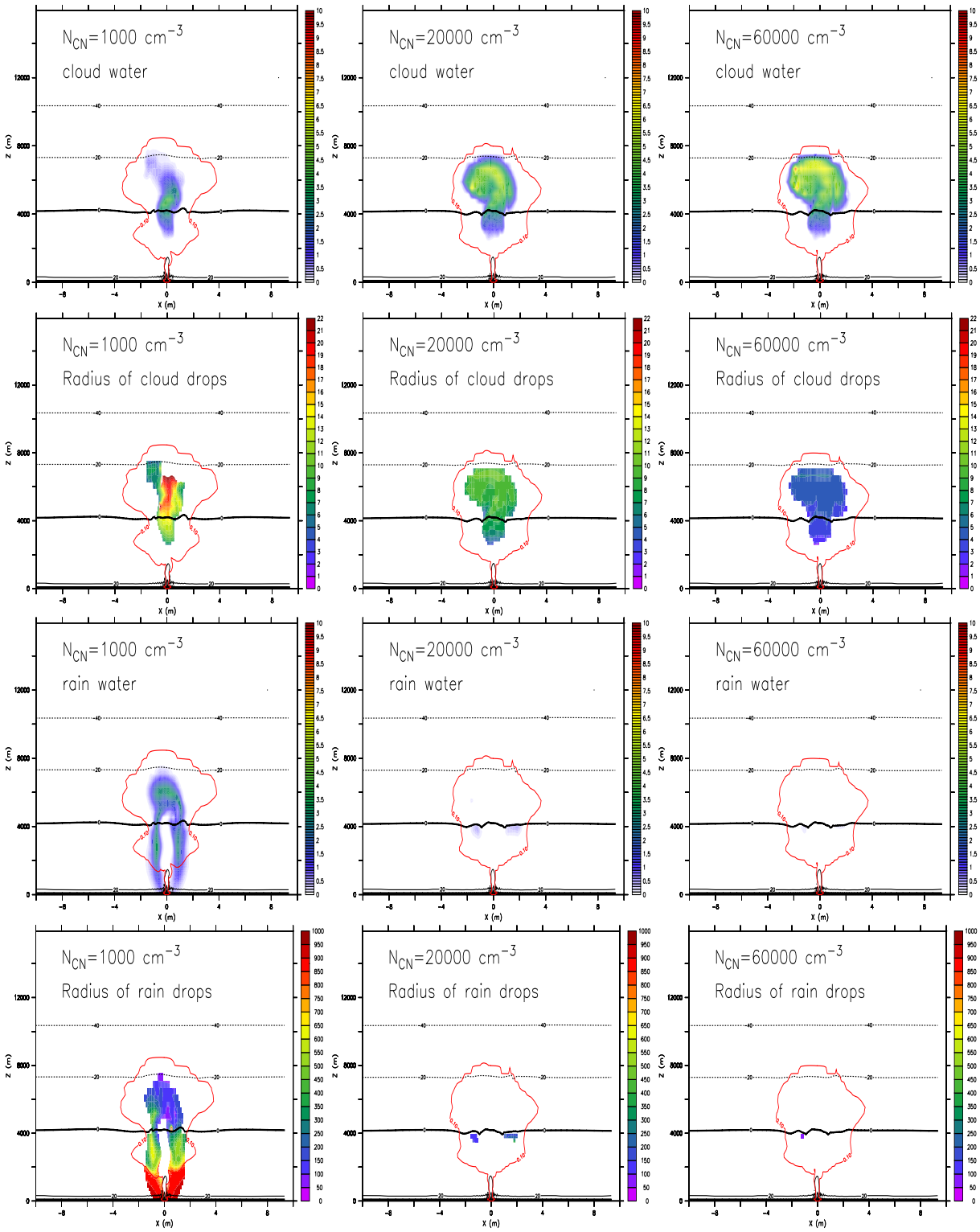

Figure 4.14: *For first and third row same as Fig. 4.12 but for (first row) the cloud water content in* $\mathrm{g\,kg^{-1}}$ *and (third row) the rain water content in* $\mathrm{g\,kg^{-1}}$*. Second and fourth rows show the volume mean radius of the cloud and rain particles in* μm *for the three aerosol concentrations, respectively.*

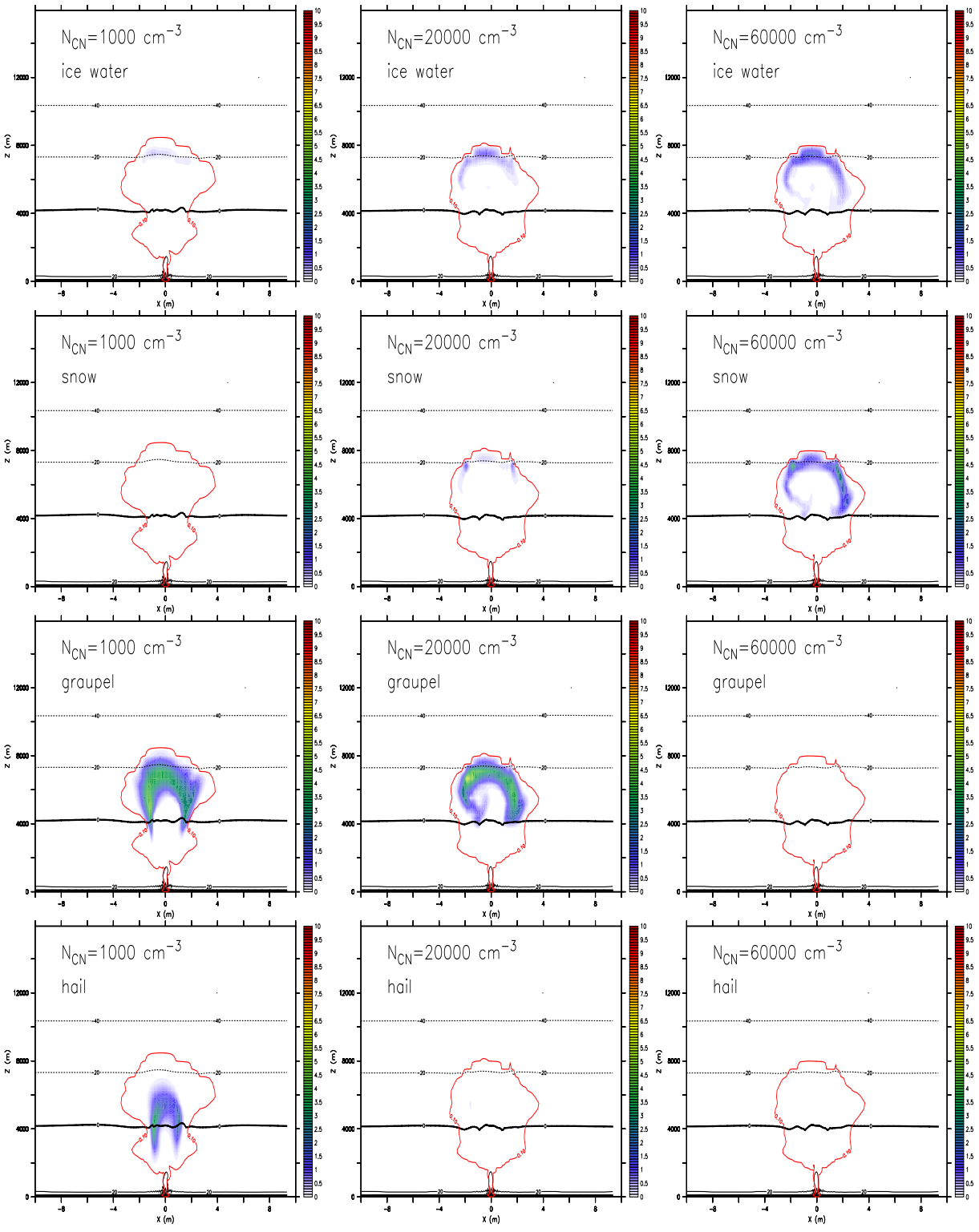

Figure 4.15: *Same as Fig. 4.12 but for (first row) ice water content in* $\mathrm{g\,kg^{-1}}$*, (second row) snow water content in* $\mathrm{g\,kg^{-1}}$*, (third row) graupel water content in* $\mathrm{g\,kg^{-1}}$*, and (fourth row) hail water content in* $\mathrm{g\,kg^{-1}}$*.*

content increase with increasing aerosol concentration, where in contrast the graupel and hail water content decrease with the aerosol concentration.

In the first place ice crystals are formed through freezing of cloud droplets, after that they can grow by deposition of water vapor and by riming of cloud droplets. Because the amount of cloud water is reduced by the autoconversion to rain, the amount of ice crystals is very low for the clean case of $N_{CN} = 1000\,\mathrm{cm}^{-3}$. On the other hand much more cloud water is left in the intermediate and strongly polluted case, therefore more cloud water is transferred to the ice crystal class. In the clean case almost no ice particles can be found and hence no significant information of the volume mean radius can be given. For the intermediate and strongly polluted case the mean volume radii of the ice crystals are up to $60\,\mu$m.

As for the ice crystals the amount of snow water content is also increasing with the aerosol concentration. Snow flakes are formed by the aggregation of ice crystals, which means that two ice crystals collide and form a larger snow flake. The growth of snow flakes happens by the aggregation of ice crystals and by riming of cloud and rain droplets. Therefore, the amount of snow is largest for the strongly polluted case, because here the largest amount of ice crystals and cloud droplets are available to form and grow snow flakes. In contrast, almost no snow is produced for the clean case because the amount of ice crystals is much lower compared to the more polluted cases and hence the formation of snow is strongly reduced. The largest volume mean radii can be found for the strongly polluted case, where the largest snow particles have a radius of $500\,\mu$m.

In contrast to the snow flakes the amount of graupel water is decreasing with increasing aerosol concentration. Graupel is mainly formed by the freezing of small rain droplets and through riming of ice crystals and snow flakes by particles of the liquid phase. When the complete ice crystal or snow flake is covered by a sphere of water it is moved to the graupel class. The growth of graupel is done by aggregation of cloud ice and snow and by riming of cloud and rain droplets. The riming by rain droplets is more effective, because they deliver more water for the growth of the graupel. Therefore, in the clean case where the largest amount of rain water can be found the amount of graupel water also is largest. The biggest graupel particles can be found in the center of the updraft region with a maximum volume mean radius of $1500\,\mu$m. In the intermediate case of $N_{CN} = 20000\,\mathrm{cm}^{-3}$ graupel is also formed by freezing rain droplets and the riming of cloud droplets on ice and snow particles. Because of the smaller liquid droplets in this case the graupel particles are significantly smaller

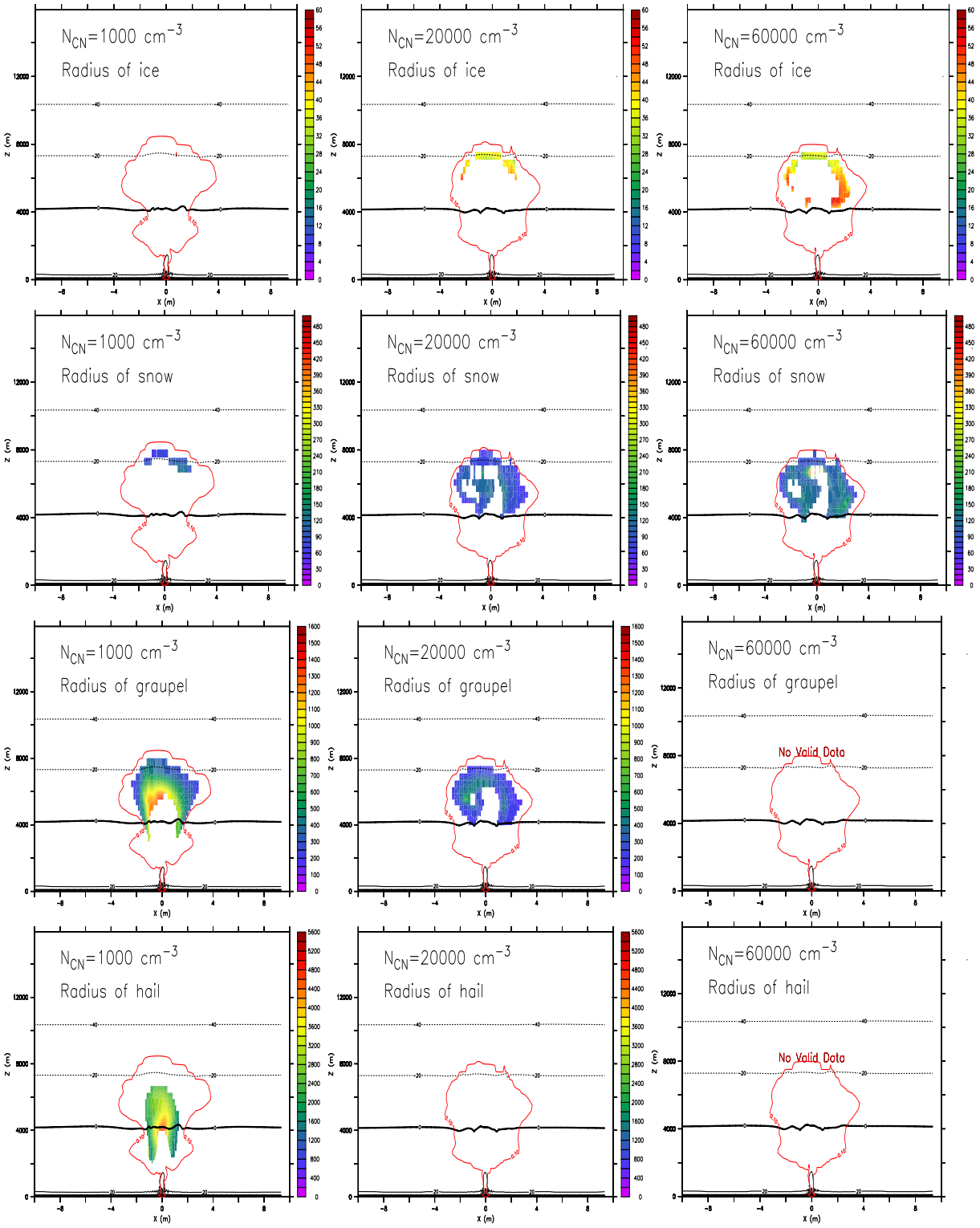

Figure 4.16: *Same as Fig. 4.12 but (first row) the volume mean radius of ice water in μm, (second row) the volume mean radius of snow in μm, (third row) the volume mean radius of graupel μm, and (fourth row) the volume mean radius of hail μm.*

compared to the clean case. The maximum volume mean radius is 700 μm. For the intermediate case, the falling graupel which is melting below the height of the 0° C isotherm produces the rain droplets indicated by the deformation of this isotherm (see also Fig. 4.14).

However, in the strongly polluted case, no significant graupel formation can be seen after 26 minutes, although a large amount of snow flakes and ice crystals are available. The reason for this is that the formation of graupel strongly depends on the size of the ice and snow particles. As it is described in Seifert and Beheng (2006a), a rimed ice or snow particle becomes a graupel particle as soon as the collected mass fills up the enveloping sphere, thus the sphere associated with the maximum diameter of the ice or snow particle. Because the volume of a sphere grows with the third power of the radius, it takes much longer for the large snow flakes in the polluted case to form graupel. Also no significant amount of rain droplets is available to freeze.

After 26 minutes a significant amount of hail is only produced in the clean case. Hail is formed in the first place by the freezing of large rain droplets and then grows by riming of cloud and rain droplets and aggregation of ice and snow particles. At this time of the cloud evolution, only in the clean case enough rain droplets are available to produce hail particles. The largest hail particles are found in the updraft region of the pyro-convective cloud and reach radii of 5000 μm. Next to the updraft region the hail particles already start to fall out of the cloud and are melting on their way to the ground. In the intermediate case hail formation is just starting. In the strongly polluted case ($N_{CN} = 60000\,\mathrm{cm}^{-3}$) no rain droplets are available to freeze and form hail.

It can be concluded that after 26 minutes of model integration, the aerosol concentration has indeed an influence on the dynamical evolution and microphysical structure of a pyro-convective cloud. In the case of a high aerosol concentration the cloud top altitude is slightly reduced. Also the amount of frozen water is decreasing with increasing aerosol concentration and also the composition of the ice phase differs. In the liquid phase, the onset of rain formation begins later with increasing aerosol concentration. Hence, only for the clean case precipitation can be observed at this time instant.

In the next section, the results after 60 minutes of model simulation will be presented and discussed.

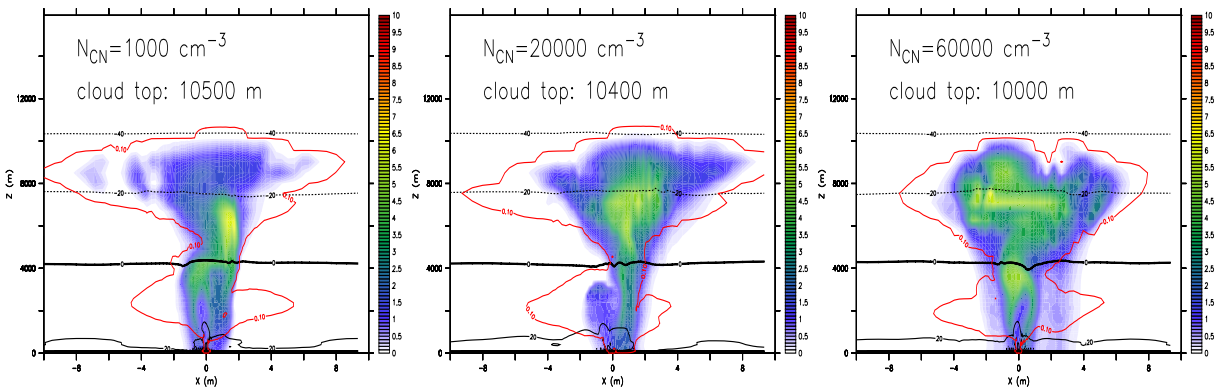

Figure 4.17: *X-Z cross section of the total hydrometeor water content after* 60 *minutes of the simulation in* $\mathrm{g\,kg^{-1}}$ *for (left)* $N_{CN} = 1000\,\mathrm{cm^{-3}}$*, (middle)* $N_{CN} = 20000\,\mathrm{cm^{-3}}$ *and (right)* $N_{CN} = 60000\,\mathrm{cm^{-3}}$*. The black lines denote the* 0° C, −20° C *and* −40° C *isotherms, respectively. The red line shows the* $0.1\,\mu\mathrm{g\,kg^{-1}}$ *isoline of the interstitial aerosol, which describes the shape of the smoke plume.*

Results after 60 minutes of model simulation

Figure 4.17 shows that after 60 minutes of the simulation the influence of the aerosol concentration still exists, but is reduced compared to the situation after 26 minutes. First, the results, which are similar to the findings after 26 minutes, are listed. In a second step, the differences between the results after 60 and 26 minutes are discussed in more detail.

Compared to the results after 26 minutes, the output after 60 minutes shows the same behaviour for the

- cloud top height, which decreases with increasing aerosol concentration (10500 m for the clean case and (10000 m for the strongly polluted case, Fig. 4.17).
- mean volume radius of the cloud droplets, which is decreasing with the aerosol concentration (Fig. 4.19). The reason for this is that new particles are constantly formed in the updraft regions of the cloud by the activation of aerosol particles.
- amount of ice crystals, which is lowest for the clean case and increasing with the aerosol concentration (Fig. 4.20). The maximum mean volume radii are in the same order of magnitude (Fig. 4.21).
- amount and size of snow, which is increasing with the aerosol concentration (Fig. 4.20 and 4.21).

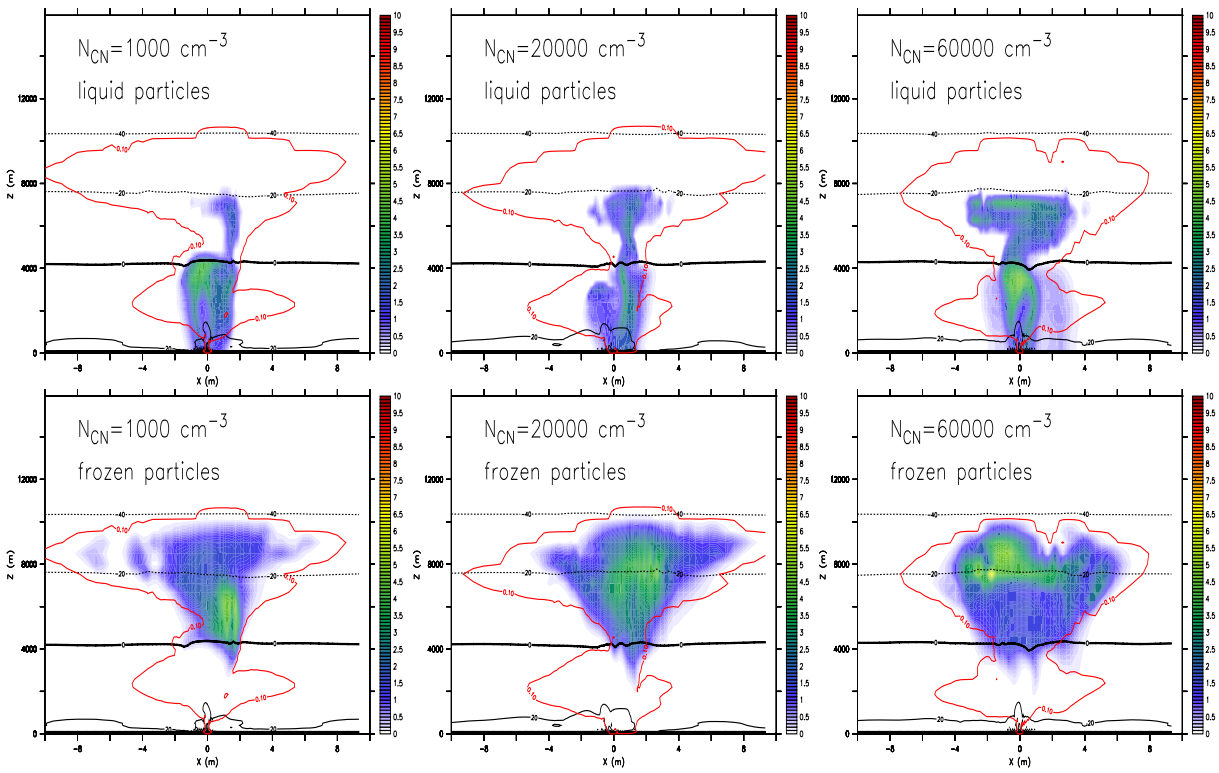

Figure 4.18: *Same as Fig. 4.17 but for (top) the total liquid water content in* $\mathrm{g\,kg^{-1}}$ *and (bottom) the total frozen water content in* $\mathrm{g\,kg^{-1}}$.

This shows that the influence of the aerosol concentration for the small frozen hydrometeor classes (ice and snow) as well for the size of the cloud droplets is to some degree constant with time. Nevertheless, after 60 minutes the vertical extension of the cloud increased and hence the distribution of the water in the cloud changed which effects the microphysical structure of the clouds.

Figure 4.17 shows that, in contrast to the results after 26 minutes, the amount of water in the cloud increases with increasing aerosol concentration. The reason for this is that in the clean case the most amount of water is removed by precipitation. Therefore, the strongly polluted case shows the largest amount of water, because the rain formation is delayed by the large amount of small cloud droplets.

In Fig. 4.18 the results are shown for the liquid and frozen phase after 60 minutes. In contrast to the results after 26 minutes, the distribution of the liquid water is changing with the aerosol concentration. After 26 minutes all three cases showed a large amount of liquid water above the freezing level. Contrarily, in the clean and intermediate case only a small amount of liquid water is found above the freezing level after 60 minutes.

The strongly polluted case shows the largest amount of liquid water with a significant portion above the freezing level.

Another difference to the results after 26 minutes is the amount of frozen water, which increases now after 60 minutes with the aerosol concentration, which is shown in the bottom row of Fig. 4.18. Due to the smaller droplets in the polluted case after 26 minutes, the formation of frozen water is delayed in this case. After 60 minutes enough time passed in order to allow the formation of frozen water.

Figure 4.19 shows the result for the two liquid categories (cloud and rain droplets) and their mean volume radius. As mentioned before, the sensitivity of cloud droplet radius to the aerosol concentration after 60 minutes is similar to the results after 26 minutes. On the other side, the distribution of the cloud water changed from the results after 26 minutes. With increasing aerosol concentration the amount of cloud water above the freezing level is increasing, because the larger cloud droplets in the clean case have a higher possibility to form rain droplets by autoconversion or to be collected by falling hydrometeors like rain, graupel or hail. Thus, the cloud droplets in the clean case are removed more effective before they can reach higher altitudes in the cloud. Therfore, almost all cloud droplets in the strongly polluted case are transported above the freezing level, where they form ice crystals or riming on other frozen particles occur.

The differences in the amount of rain water after 26 minutes are vanished after 60 minutes. After 60 minutes rain water can be found in all three cases in the same order of magnitude. The reason for this is that in the more polluted cases the rain formation by frozen particles (melting of snow, graupel and hail) becomes very efficient after 60 minutes. Hence, differences in the distribution of the rain water between the three cases are rather small. For the mean volume radii of the rain droplets only small differences can be seen. The largest rain droplets are always around 900 μm. The strongly polluted case shows the largest amounts of large rain droplets. These results indicate that the autoconversion of cloud droplets to rain droplets plays only a minor role after 60 minutes of model integration. Hence, the formation of rain by frozen particles, thus melting of snow, graupel and hail is more important.

The results for the graupel water content after 60 minutes are clearly different compared to the results after 26 minutes. In the early stage of the cloud after 26 minutes, graupel was formed only for the clean case and the intermediate case, where the clean case produced more than the intermediate (see Fig. 4.15). In the strongly polluted case no graupel was formed at that time. In contrast, after 60 minutes the

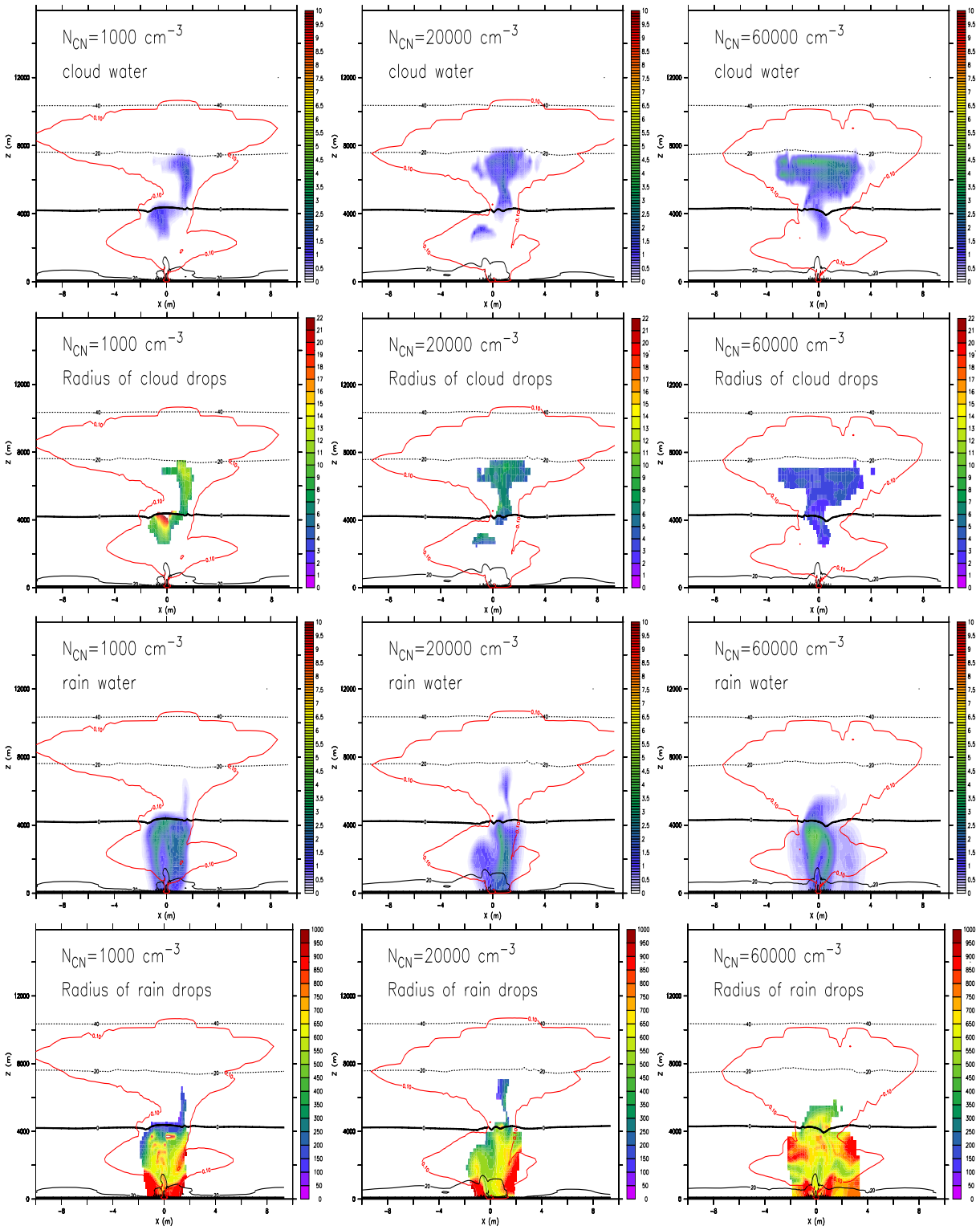

Figure 4.19: *For first and third row same as Fig. 4.17 but (first row) the cloud water content in* $\mathrm{g\,kg^{-1}}$ *and (third row) the rain water content in* $\mathrm{g\,kg^{-1}}$*. Second and fourth rows show the volume mean radius of the cloud and rain particles in* μm *for the three aerosol concentrations, respectively.*

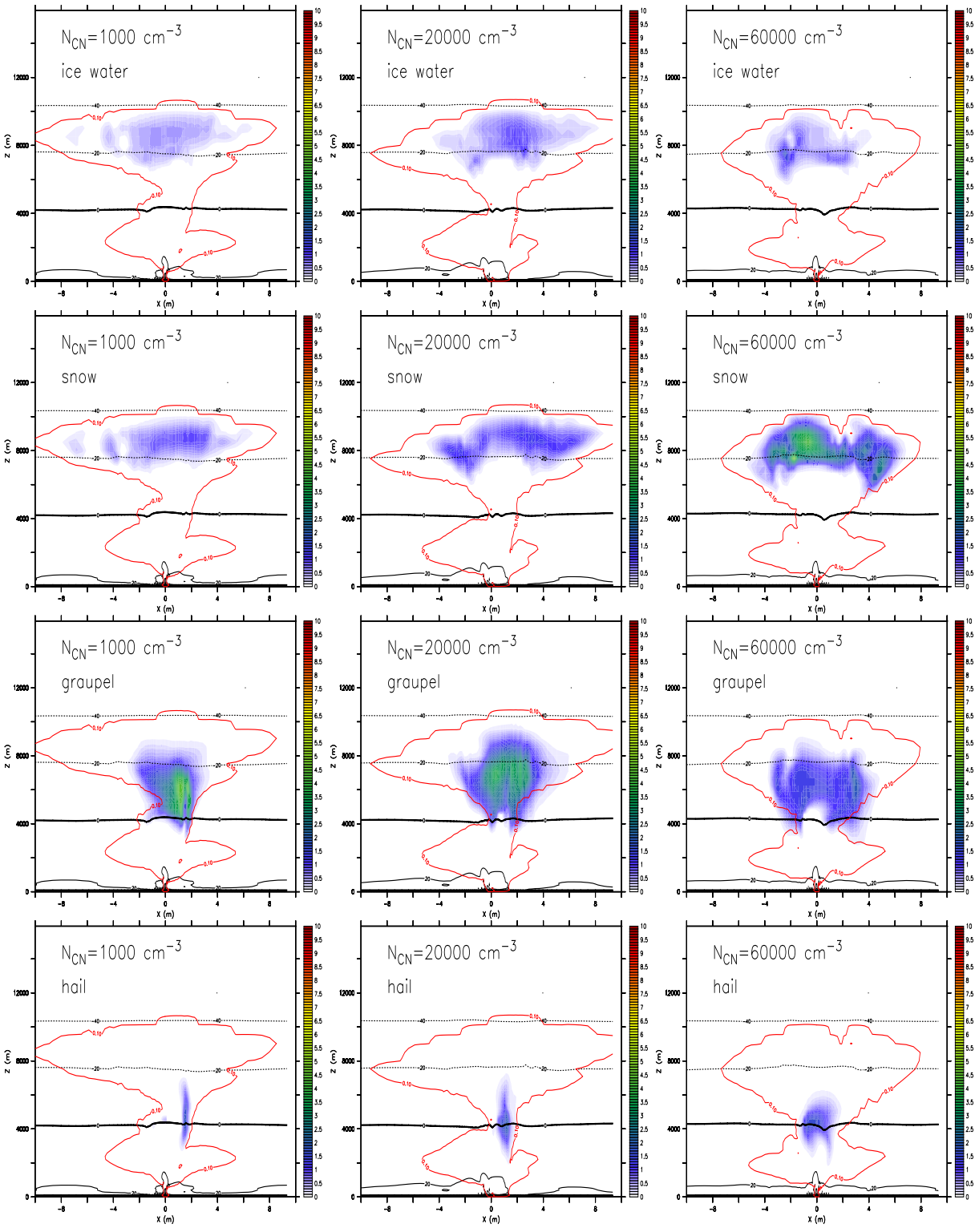

Figure 4.20: *Same as Fig. 4.17 but (first row) ice water content in* $\mathrm{g\,kg^{-1}}$*, (second row) snow water content in* $\mathrm{g\,kg^{-1}}$*, (third row) graupel water content in* $\mathrm{g\,kg^{-1}}$*, and (fourth row) hail water content in* $\mathrm{g\,kg^{-1}}$.

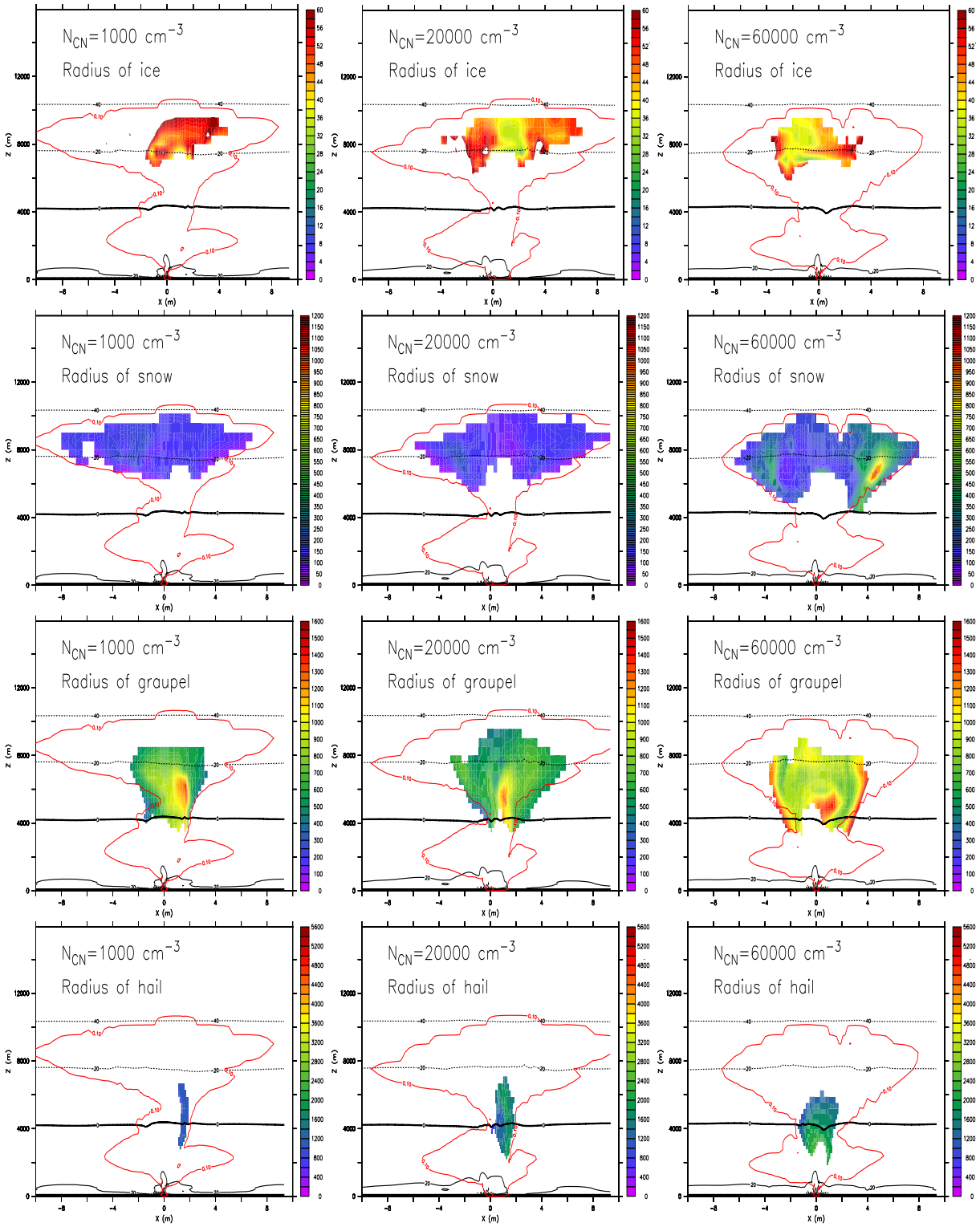

Figure 4.21: *Same as Fig. 4.17 but (first row) the volume mean radius of ice water in μm, (second row) the volume mean radius of snow in μm, (third row) the volume mean radius of graupel μm, and (fourth row) the volume mean radius of hail μm.*

amount of graupel is in the same order of magnitude for all three cases. Nevertheless, in the clean case the amount of graupel is concentrated on a smaller region of the cloud, while this region is larger for the higher aerosol concentrations. Figure 4.21 shows that the mean volume radius is largest for the strongly polluted case with the maximum mean volume radius of 1500 μm. The maximum value in the clean case is also 1500 μm, for the intermediate case it is lower (1300 μm).

Also for hail, the results strongly differ after 26 and 60 minutes. After 26 minutes, hail was formed only for the clean case. After 60 minutes hail is found for all cases, but is most abundant for the strongly polluted case. In the other two cases, a large part of the hail already fell out of the cloud as precipitation and was therefore removed from the atmosphere (see Fig. 4.11). Because of this, the polluted cloud shows the largest hydrometeor water content (see Fig. 4.17). The produced hail in the three cases after 60 minutes is clearly smaller (mean volume radii between 1000 and 2400 μm) compared to the sizes for the clean case after 26 minutes (mean volume radii up to 4500 μm), because more water is transferred to graupel than to hail.

Conclusions

In this section the influence of the aerosol concentration on the dynamical and microphysical structure of a pyro-convective cloud has been studied for a clean, intermediate polluted and strongly polluted atmosphere. While the influence of the aerosol concentration on the dynamics is rather weak as far as the cloud top height is concerned the impact on the microphysics shows interesting features. Each case shows a different way of development.

In Fig. 4.22 the temporal evolution of the number of grid points can be seen, which is a measure for the size of the cloud. This picture shows that the growth of a pyro-convective cloud depends on the aerosol concentration. The more aerosol particles that are available, the more the growth of the cloud is delayed. This will be discussed in the following.

In the clean case after the rapid formation of rain by autoconversion of cloud droplets, graupel and hail are formed within a short time period. This means that already at an early stage of the cloud evolution a significant amount of water is transferred to the frozen phase. This leads to a strong release of latent heat resulting in a rapid evolution of the cloud. Hence, the number of cloudy grid points shows a strong increase for the clean case already after 700 s. On the other hand, the rain droplets,

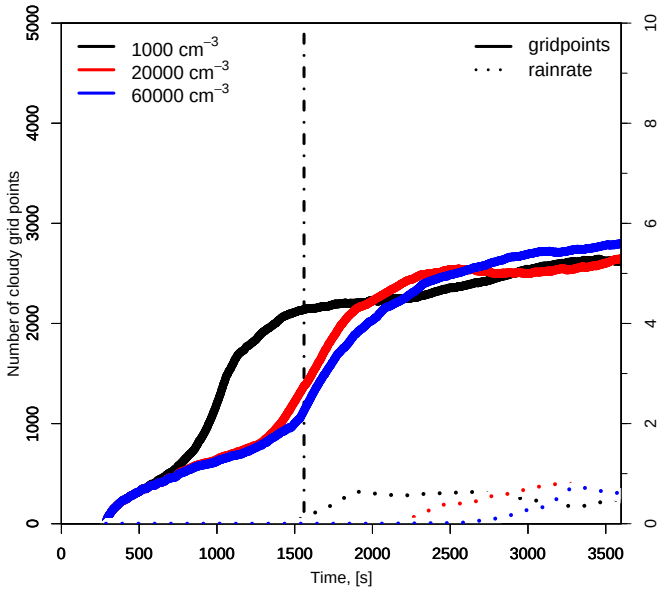

Figure 4.22: *Temporal evolution of the number of cloudy grid points for aerosol concentrations of (black)* $N_{CN} = 1000\,\mathrm{cm}^{-3}$*, (red)* $N_{CN} = 20000\,\mathrm{cm}^{-3}$ *and (blue)* $N_{CN} = 60000\,\mathrm{cm}^{-3}$ *and (dashed) for the rain rate in* $\mathrm{kg\,m}^{-2}, \mathrm{s}^{-1}$ *of the three specified aerosol concentrations. The vertical black line denotes the results after* 26 *minutes, the time axis ends after* 60 *minutes.*

graupel and hail particles grow rapidly and soon start to fall out. For hail a large amount of particles have fallen out after 45 minutes. This means that a lot of water is removed from the atmosphere. This explains why the increase in the number of cloudy grid points is strongly reduced for the clean case after 30 minutes. Interestingly, cloud ice and snow particles play a minor role for the cloud in the clean case, because graupel and hail are the dominant frozen hydrometeor classes, which depend mainly on the rapid formation of large rain droplets.

In the intermediate case the formation of rain is slower compared to the clean case, because the cloud droplets are smaller. Therefore, the formation of ice crystals and snow flakes becomes more important for the formation of graupel. In this case the freezing of water is delayed and hence the release of latent heat is also delayed. This explains why the rapid increase of the number of cloudy grid points begins later than for the clean cloud. Because the formation of hail depends on the freezing of large rain droplets, evolution of hail is also delayed.

In the strongly polluted case the formation of rain, graupel and hail is even more delayed compared to the previous case, because of the very small size of the cloud

droplets in this case. After 26 minutes only cloud droplets, ice crystals and snow flakes can be seen with a significant amount. Therefore, the rapid increase of the number of cloudy grid points by the release of latent heat occurs later than in the other cases. After 60 minutes, the strongly polluted case is the case with the largest amount of hail, because its formation is much more delayed.

To conclude it can be stated that the aerosol concentration has a small influence on the size of a pyro-convective cloud, but is very important for its microphysical evolution. One important result is that the onset of precipitation is delayed with increasing aerosol concentration. This can be seen in Fig. 4.22, where the rain rate is shown for the three cases. The onset of precipitation reaching the ground starts later with increasing aerosol concentration. This is described as the indirect aerosol effect but is shown here for the first time for a pyro-convective cloud with aerosol concentrations up to $N_{CN} = 60000\,\mathrm{cm}^{-3}$.

Interestingly, with proceeding time the differences in the microphysical structure are getting smaller and similar amounts of precipitation are formed, but with a strongly differing microphysical origin.

Nevertheless, various studies show the different microphysical evolution of clouds for different aerosol concentrations in observational data (e.g. Costa et al. (2000), Andreae et al. (2004)) and in model studies (e.g. Khain et al. (2005), Seifert and Beheng (2006b), Diehl et al. (2007), Tao et al. (2007)), which support the findings of this study. However, in the 3D model simulations (Khain et al. (2005), Seifert and Beheng (2006b), Tao et al. (2007)) the sensitivity of the aerosol concentration on the evolution of clouds was studied in a range between $N_{CN} = 100\,\mathrm{cm}^{-3}$ and $N_{CN} = 2500\,\mathrm{cm}^{-3}$ with the assumption of a model salt like the very hydrophilic sodium chloride ($\kappa = 1.28$). This is very unrealistic, because during a biomass burning event a high number of less hydrophilic particles ($\kappa < 0.6$) are emitted. Admittedly, the sensitivity on the aerosol concentration is larger, when more hydrophilic particles like sodium chloride are used. Therefore, the effects of the pollution on the evolution of a cloud with lower aerosol concentrations but higher hygroscopicity is an approximation of the conditions presented in this thesis. Hence, for the first time the sensitivity of the aerosol concentration on the evolution of pyro-convective clouds were studied with a realistic description of the activation of cloud droplets from clean to strongly polluted conditions through the look-up table with the results from Chapter 2.

4.5 Further sensitivity studies

4.5.1 Sensitivity to ice nucleation ability

In this section the influence of ice nucleation ability on the development of a pyro-convective cloud is investigated. The ice nucleation efficiency $B_{h,i}$ in cm^{-3} describes the ability of an insoluble particle per unit volume of liquid to freeze a cloud droplet by immersion freezing (Diehl et al. (2007)). The more efficiently a particle can act as an immersion freezing nucleus (IN), the higher the value of $B_{h,i}$. If $B_{h,i}$ is set to zero it is assumed that no heterogeneous freezing occurs. The cloud droplets will then freeze only by homogeneous freezing at significantly lower temperatures compared to the immersion freezing, which delays the glaciation of a cloud.

The default value of $B_{h,i}$ in the microphysical scheme of ATHAM is set to $1 \cdot 10^{-4}\,\mathrm{cm}^{-3}$, which is characteristic for mineral particles. However, in a biomass burning cloud a high concentration of biological particles, which act very efficiently as IN, are emitted through the fire and transported to the atmosphere. Hence, for all simulations in Section 4.4 (4.5.2 and later) the default value of $B_{h,i}$ was increased by a factor of $1 \cdot 10^3$, which is characteristic for leaf litter. Note that in the current setup of the microphysical scheme no information of the number of IN is available. Muhlbauer and Lohmann (2009) presented a new approach of the calculation of the ice nucleation ability $B_{h,i}$ including the aerosol number concentration. This parameterization takes the number of IN into account that are available for the glaciation of a cloud. It is suggested that this approach should be included in forthcoming versions of this model.

In this section the sensitivity of the result for the strongly polluted case ($N_{CN} = 60000\,\mathrm{cm}^{-3}$) from Section 4.4 is investigated for $B_{h,i} = 0\,\mathrm{cm}^{-3}$, $B_{h,i} = 1 \cdot 10^{-4}\,\mathrm{cm}^{-3}$ and $B_{h,i} = 1 \cdot 10^{-1}\,\mathrm{cm}^{-3}$.

Figure 4.23 shows the temporal evolution of the number of cloudy grid points for the three different IN concentrations and the corresponding rain rate. It can be seen that the evolution of the cloud is faster when the ice nucleation ability is high, because the onset of freezing starts earlier compared to the cases with lower efficiencies. When the freezing starts earlier, also the release of latent heat happens earlier and hence stronger updraft velocities occur. Finally, the onset of precipitation reaching the ground happens earlier, when the freezing starts earlier. The cases with zero ability and with using the default value for non-pyro clouds ($B_{h,i} = 1 \cdot 10^{-4}\,\mathrm{cm}^{-3}$) show only minor differences.

In Fig. 4.24 the temporal evolution of the averaged water content for the three

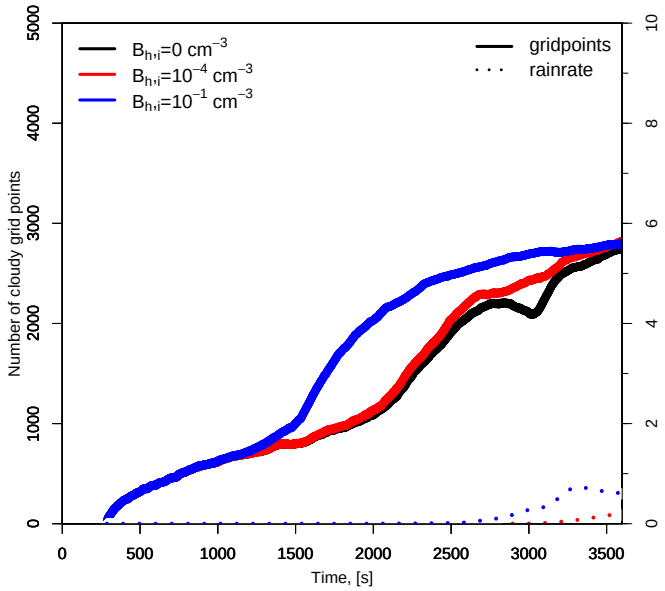

Figure 4.23: *Temporal evolution of the number of cloudy grid points for (black) an ice nucleation ability of* $B_{h,i} = 0\,\mathrm{cm}^{-3}$*, (red)* $B_{h,i} = 1 \cdot 10^{-4}\,\mathrm{cm}^{-3}$ *and (blue)* $B_{h,i} = 1 \cdot 10^{-1}\,\mathrm{cm}^{-3}$ *for an aerosol concentration of* $N_{CN} = 60000\,\mathrm{cm}^{-3}$ *and (dashed) for the rain rate in* $\mathrm{kg\,m}^{-2}, \mathrm{s}^{-1}$ *of the three specified aerosol concentrations. The time axis ends after* 60 *minutes.*

different ice nucleation abilities with an aerosol concentration of $N_{CN} = 60000\,\mathrm{cm}^{-3}$ can be seen. In the right panel of this picture the results with an ice nucleation ability of $B_{h,i} = 1 \cdot 10^{-1}\,\mathrm{cm}^{-3}$ can be seen, which is the value chosen for all previous model runs, shown here again as the reference case.

In the case $B_{h,i} = 0\,\mathrm{cm}^{-3}$, which means with no heterogeneous freezing, the formation of ice crystals is very weak compared to the reference case, because only the cloud droplets in the upper parts of the cloud are cold enough for homogeneous freezing. The same observations is true for the snow flakes, because they depend on the formation of ice crystals. Also, the formation of graupel and hail is much more delayed compared to the reference run.

For an ice nucleation ability of $B_{h,i} = 1 \cdot 10^{-4}\,\mathrm{cm}^{-3}$ the results are similar to the no ability case. The formation of ice crystals and snow flakes starts at the same time compared to the no ability case, but the increase of the ice crystal and snow water content is stronger, because the freezing temperature is now higher. This means that a larger area of the cloud has the sufficient freezing temperature for the formation of ice crystals.

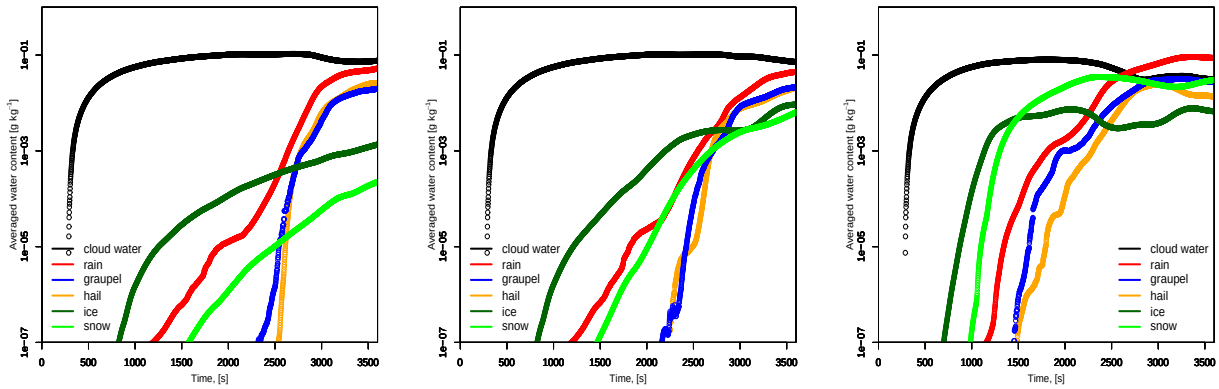

Figure 4.24: *Temporal evolution of the averaged water content in* $\mathrm{g\,kg^{-1}}$ *in the model domain for the six hydrometeor classes (black) cloud water, (red) rain water, (blue) graupel, (orange) hail, (dark green) ice and (green) snow for an aerosol concentration of* $N_{CN} = 60000\,\mathrm{cm^{-3}}$ *for (left)* $B_{h,i} = 0\,\mathrm{cm^{-3}}$ *no IN ability, (middle)* $B_{h,i} = 1 \cdot 10^{-4}\,\mathrm{cm^{-3}}$ *default value of microphysical scheme and (right)* $B_{h,i} = 1 \cdot 10^{-1}\,\mathrm{cm^{-3}}$ *value used for all calculations in this study. The time axis ends after* 60 *minutes.*

Despite these differences, the characteristic behaviour of the microphysics for the strongly polluted case, namely the formation of precipitation by the ice particles and snow flakes, can be seen for all studied ice nucleation abilities.

These results show that the ice nucleation ability plays an important role for the onset time and strength of the ice formation and has therefore a great influence on the temporal evolution of a cloud. More information of the spatial distribution and composition of IN in pyro-convective clouds would be needed to obtain more accurate results.

4.5.2 Sensitivity to the atmospheric background profile

To study the influence of the atmospheric background profile on the results from Section 4.4 simulations with a tropical US standard atmosphere (Fig. 4.25 right) have also been conducted. The other model parameters stayed the same as described in Section 4.4.1. The differences between the two atmospheric profiles are that the tropical atmosphere is more humid (mixing ration of $16.8\,\mathrm{g\,kg^{-1}}$ at the surface) compared to the mid-latitude atmosphere (mixing ration of $11.8\,\mathrm{g\,kg^{-1}}$ at the surface). Also the tropopause is significantly higher in the tropics. Therefore, it is interesting to investigate the influence of more humid atmosphere on the results from Section 4.4.

Figure 4.26 shows the averaged water content per cloudy grid point after 60 minutes of model integration for the three different aerosol concentrations $N_{CN} = 1000\,\mathrm{cm^{-3}}$,

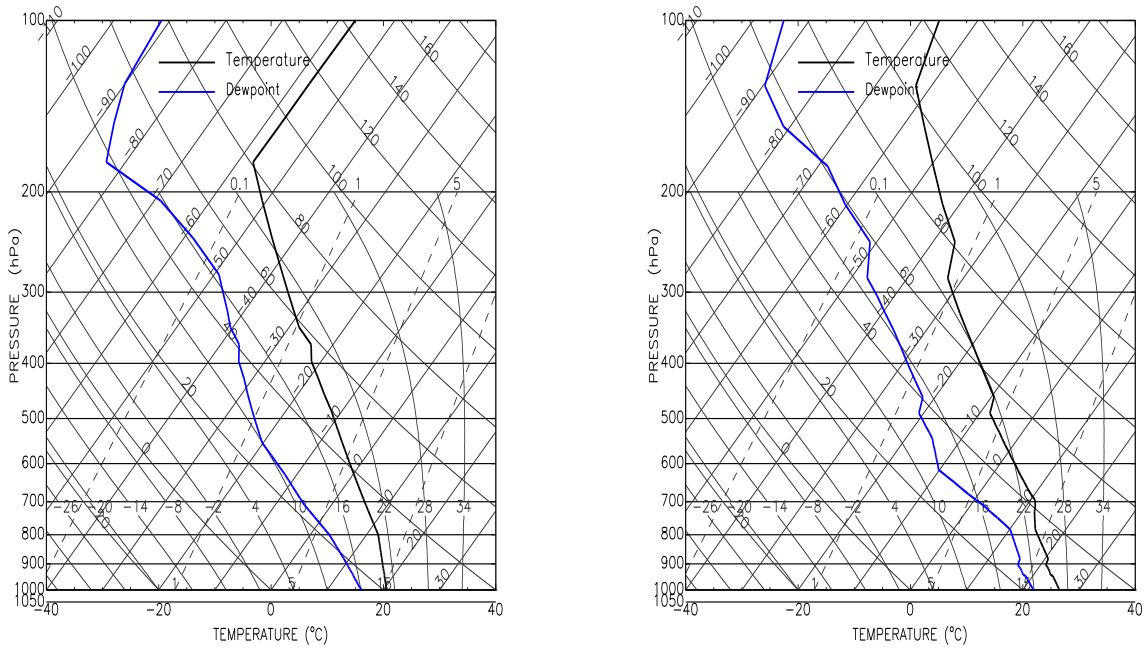

Figure 4.25: *Skew-T log-p diagram of (left) the mid-latitude and (right) the tropical US standard atmosphere.*

$N_{CN} = 20000\,\mathrm{cm}^{-3}$ and $N_{CN} = 60000\,\mathrm{cm}^{-3}$ and can be compared to the results with the mid-latitude US standard atmosphere in Fig. 4.11.

The results for the clean case are very similar for the mid-latitude and the tropical profiles. The rain formation in the tropical clean case starts almost at the same time compared to the mid-latitude case. After that cloud ice is forming, followed by graupel, snow and hail during a short period of time. After 60 minutes graupel and rain are the largest hydrometeor classes. In contrast, the amount of ice crystals and snow flakes is significantly higher in the tropical compared to the mid-latitude case. This can be explained by the higher updraft velocities and larger updraft region in the tropical case, which transport more liquid water to higher altitude, where freezing can take place. This is shown in Fig. 4.27, where the updraft velocity for the mid-latitude and tropical atmospheric profile with an exemplary aerosol concentration of $N_{CN} = 20000\,\mathrm{cm}^{-3}$ after 16 minutes is presented. Note that the updraft velocity for the clean and strongly polluted case shows a very similar behaviour, therefore only the intermediate case is shown.

Nevertheless, the main feature of the clean case that significant rain formation occurs before the formation of graupel and the minor importance of ice crystals and snow is independent of the atmospheric profile.

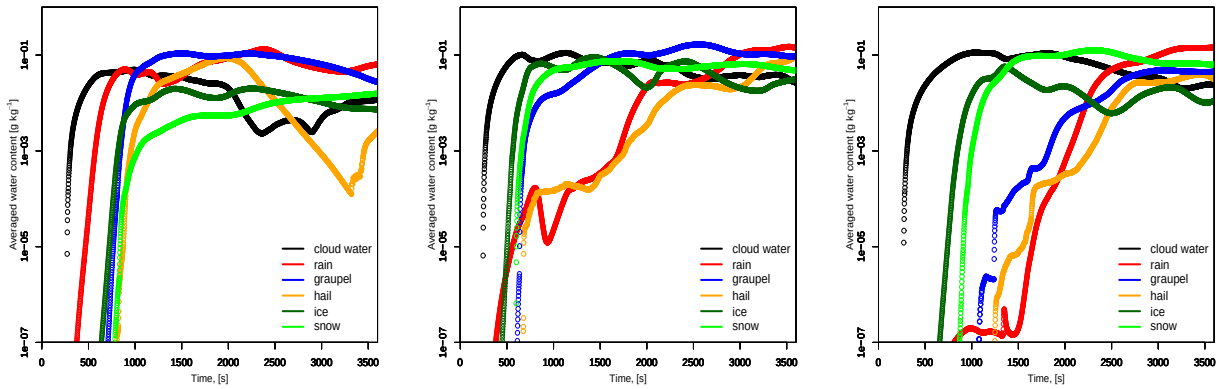

Figure 4.26: *Temporal evolution of the averaged water content in* $\mathrm{g\,kg^{-1}}$ *in the model domain for the six hydrometeor classes (black) cloud water, (red) rain water, (blue) graupel, (orange) hail, (dark green) ice and (green) snow for (left) the clean case with* $N_{CN} = 1000\,\mathrm{cm^{-3}}$*, (middle) the intermediate case with* $N_{CN} = 20000\,\mathrm{cm^{-3}}$ *and (right) the strongly polluted case with* $N_{CN} = 60000\,\mathrm{cm^{-3}}$ *calculated with a tropical atmospheric profile. The time axis ends after 60 minutes.*

For the intermediate case of aerosol concentration ($N_{CN} = 20000\,\mathrm{cm^{-3}}$) a distinct difference in the amount of rain during the evolution of the cloud can be seen when using the tropical instead of the mid-latitude profile. However, the evolution of the intermediate polluted tropical cloud shows a similar behaviour compared to the mid-latitude cloud for an intermediate pollution. Soon, after the first occurance of small amounts of rain, the formation of ice, snow and graupel become more important, which is in agreement with the results for the mid-latitude profile. Nevertheless, the significant production of rain and hail is clearly delayed compared to the other hydrometeors. However, after 60 minutes of model simulation the results for the intermediate polluted case shows the same characteristics in both studied atmospheres.

The results for the strongly polluted case calculated with a tropical atmosphere show the same behaviour as for the mid-latitude polluted case. The formation of ice and snow particles is the first microphysical process which comes into play. But again, the amount of ice and snow flakes is larger in the tropical case due to the larger updraft velocities. After the ice and snow formation a very small amount of rain water is produced, which is enough to trigger the formation of graupel and hail, similar to the mid-latitude polluted case. After 60 minutes, rain is again the dominant hydrometeor class and no hail is precipitating.

It can be concluded that the influence of the aerosol concentration on the development of a pyro-convective cloud shows a similar behaviour, when the atmospheric profile is changed from the mid-latitudes to the tropics. Apparently, the warmer and

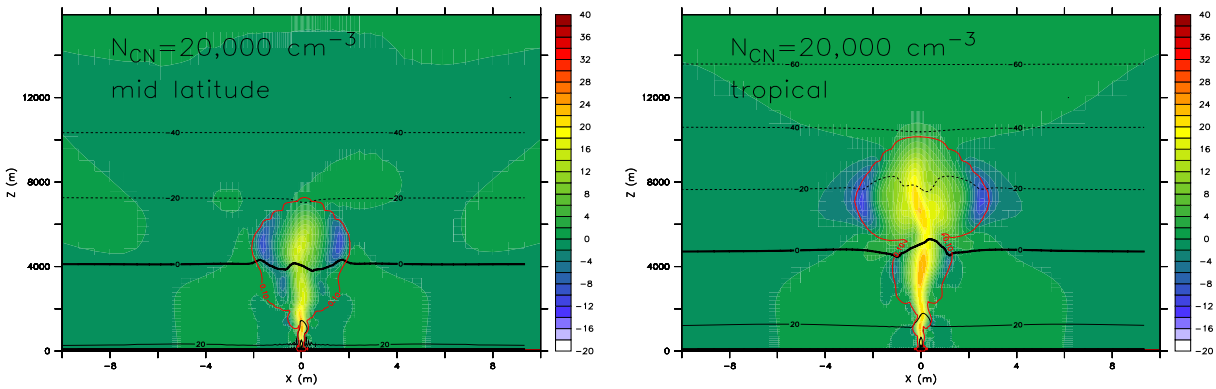

Figure 4.27: *X-Z cross sections of the vertical velocity for an aerosol concentration of* $N_{CN} = 20000\,\mathrm{cm}^{-3}$ *for (left) the mid-latitude and (right) the tropical atmospheric profile after* 16 *minutes. The horizontal black lines denote the* 0° C, −20° C *and* −40° C *isotherms, respectively. The other black line shows the* $0.1\,\mu\mathrm{g\,kg}^{-1}$ *isoline of the interstitial aerosol, which describes the shape of the smoke plume.*

more humid atmosphere in the tropics leads to a stronger updraft velocity and more water is available in higher altitudes to freeze which then has an impact on the ratio between liquid and frozen water. It seems that the atmospheric background profile does not significantly change the sensitivity of the aerosol concentration on the development of the pyro-convective cloud. Nevertheless, future investigations should focus on the atmospheric background profiles from different seasons in both the mid-latitude and the tropics to estimate the range of sensitivity of the aerosol concentration on cloud dynamics and microphysics.

4.5.3 Sensitivity to the fire forcing

The previous results have been obtained by using the fire forcing as specified in Section 4.4.1. Apparently, the fire forcing determines the release of sensible heat from the fire and hence the strength of the updraft velocity above the fire. Therefore the question arises, how the fire forcing is influencing the presented results. To address this question, model simulations using the US standard atmosphere for the tropics (see Fig. 4.25) and varying the fire forcing between 10 and $1000\,\mathrm{kW\,m}^{-2}$ have been conducted.

The left panel on Fig. 4.28 shows the influence of the fire forcing on the cloud top altitude after 60 minutes of model integration. It can be clearly seen that the fire forcing is governing the cloud top height. Especially for values below $200\,\mathrm{kW\,m}^{-2}$ it is important to know the exact value of the fire forcing for an accurate simulation of real

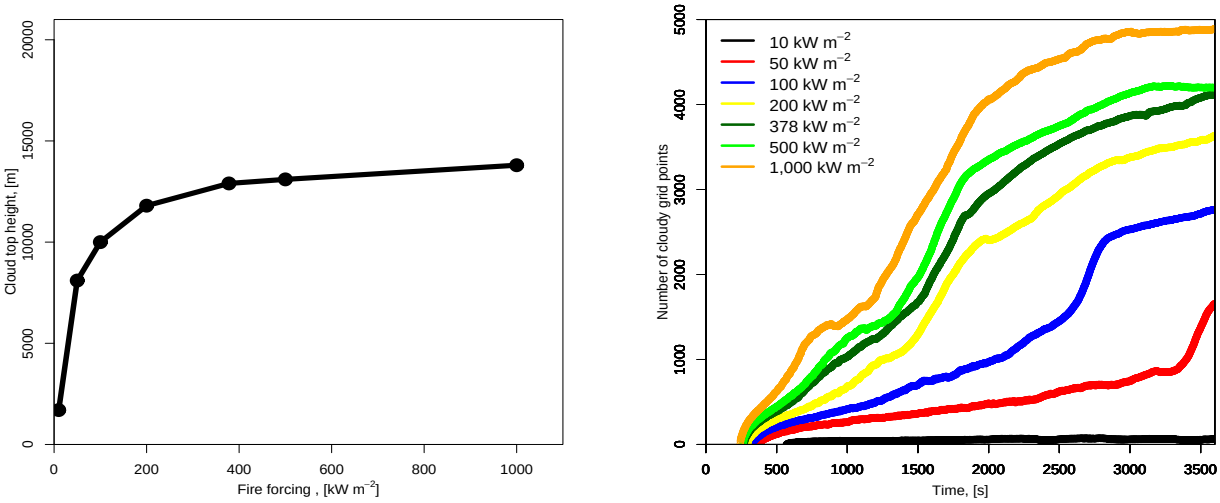

Figure 4.28: *Dependency of (left) cloud top altitude after a model integration of* 60 *minutes and (right) temporal evolution of the number of cloudy grid points on the fire forcing.*

cases. Around a fire forcing of 378 kW m^{-2}, which is the value used for all the studies presented before, a saturation of the dependency of the cloud top height on the fire forcing can be observed due to the tropopause.

The right panel of Fig. 4.28 shows the temporal evolution of the number of cloudy grid points and supports the conclusion from the analysis of the cloud top height. It can be clearly seen that for weak forcings, a small increase leads to a strong increase in the number of cloudy grid points and hence the size of the pyro-convective cloud. The figure also shows that the onset of freezing is delayed with decreasing fire forcing, which can be identified by the kink in each curve. The onset of freezing with a fire forcing of 100 kW m^{-2} is around 2, 500 s, while the onset of freezing with a fire forcing of 1000 kW m^{-2} is around 1000 s. In the case of a fire forcing of 10 kW m^{-2} no freezing occurs, consistent with the lowest cloud top altitude for all cases.

Figure 4.29 shows the difference in the temporal evolution of the hydrometeor classes for different fire forcings. In Fig. 4.29 a) the result for a fire forcing of 10 kW m^{-2} shows that only a small cloud is produced that only contains cloud water. This is because of the low updraft velocities in this case, which inhibit the cloud to reach the freezing level.

An increase of the fire forcing from 10 to 50 kW m^{-2} leads to the formation of all hydrometeor classes, but clearly delayed compared to the results for a fire forcing of 378 kW m^{-2}. Nevertheless, the behaviour is nearly the same, namely that the formation of ice crystals and snow starts before the significant formation of the other hydromete-

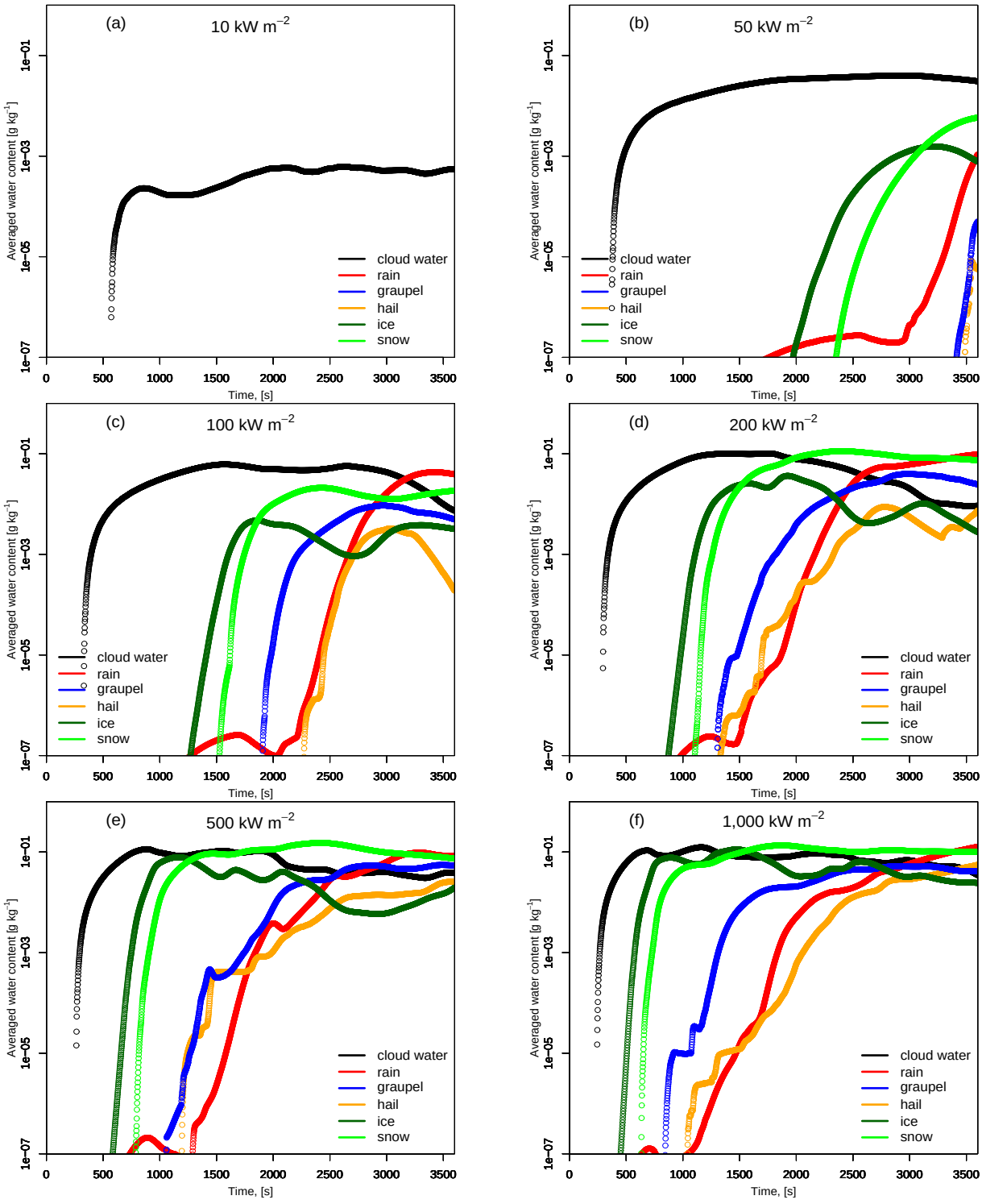

Figure 4.29: *Temporal evolution of the hydrometeor classes for six different fire forcings, namely (top left)* 10 kW m^{-2}, *(top right)* 50 kW m^{-2}, *(middle left)* 100 kW m^{-2}, *(middle right)* 200 kW m^{-2}, *(bottom left)* 500 kW m^{-2} *and (bottom right)* 1000 kW m^{-2}.

ors. However, in the case of $50\,\mathrm{kW\,m^{-2}}$ the significant formation of rain starts before the formation of graupel. The reduced updraft velocity by the weaker fire forcing leads to a delayed formation of graupel.

With increasing fire forcing there is an earlier onset of ice and snow formation. Also the other hydrometeors appear earlier, while now the graupel plays a more important role prior to the significant formation of rain.

It can be concluded that the fire forcing has a very important effect on the dynamical evolution of a pyro-convective cloud. The more heat is emitted by a fire, the higher and larger the cloud. On the other hand, the characteristic evolution of the hydrometeor classes is unchanged, as long as the fire forcing is above a certain threshold.

This indicates that the dynamical evolution of a pyro-convective cloud depends more on the fire forcing, while the microphysical structure is strongly sensitive to the aerosol concentration.

4.6 First 3D results

In order to support the results from the 2D studies from Section 4.4 3D model runs for the three aerosol concentrations ($N_{CN} = 1000\,\mathrm{cm^{-3}}$, $N_{CN} = 20000\,\mathrm{cm^{-3}}$ and $N_{CN} = 60000\,\mathrm{cm^{-3}}$) were conducted.

The 3D model runs were initialized with a mid-latitude US standard atmosphere (see Fig. 4.25). The model domain was set to 40 km x 30 km x 20 km with 110 x 80 x 55 grid boxes in the x-y-z-directions, respectively. The minimum horizontal grid box size was set to 50 m and the minimum vertical grid box size to 100 m.

The size of the fire front was set to 300 m x 300 m. The energy release from the fire was calculated based on a fuel loading of $9\,\mathrm{kg\,m^{-2}}$ and a value of $18,700\,\mathrm{kJ\,kg^{-1}}$ for the heat combustion. This converts to a fire forcing of $378\,\mathrm{kW\,m^{-2}}$. Because of the increased entrainment in 3D simulations (Petch et al. (2008)), the fuel loading was doubled compared to the 2D simulations in order to create comparable updraft regions.

Figure 4.30 shows the temporal evolution of the averaged water content for the three different aerosol concentrations, which can be compared to the results of Fig. 4.11. For the clean case ($N_{CN} = 1000\,\mathrm{cm^{-3}}$) some of the results are similar to the results from the clean case of the 2D runs. The rapid rain formation starts almost at the same time in both cases. Nevertheless, in the 3D runs this rain formation goes along with the formation of cloud ice, snow and graupel while in the 2D runs the formation of frozen particles starts with a delay of several minutes. Also, after the first rapid formation the

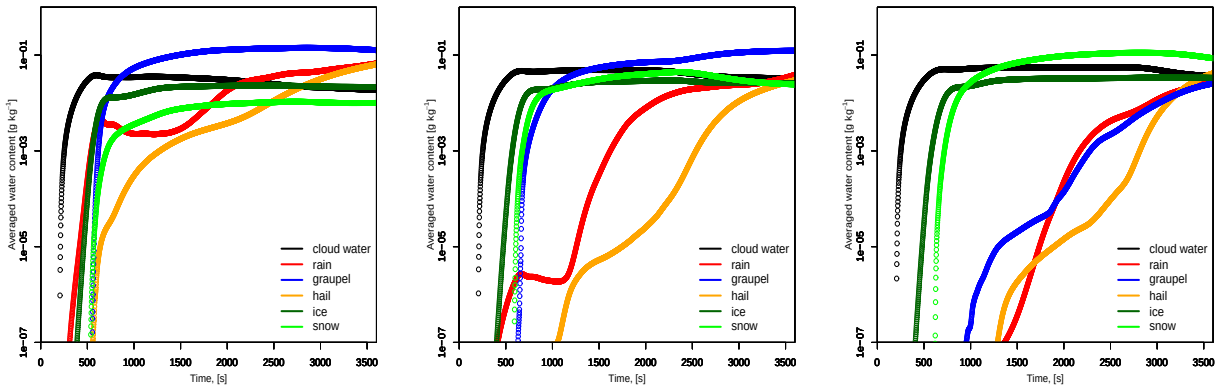

Figure 4.30: *Temporal evolution of the averaged water content in* $\mathrm{g\,kg^{-1}}$ *in the model domain for the six hydrometeor classes (black) cloud water, (red) rain water, (blue) graupel, (orange) hail, (dark green) ice and (green) snow for (left) the clean case with* $N_{CN} = 1000\,\mathrm{cm^{-3}}$*, (middle) the intermediate case with* $N_{CN} = 20000\,\mathrm{cm^{-3}}$ *and (right) the strongly polluted case with* $N_{CN} = 60000\,\mathrm{cm^{-3}}$ *for the 3D simulation. The time axis ends after 60 minutes.*

averaged rain water content is decreasing during the first production of hail particles. This feature is indicated in the 2D case only by a very small decrease during a short period of time. After 60 minutes the largest differences between the 2D and the 3D cases are visible for the averaged hail water content. In the 2D case most of the hail has been fallen out of the cloud while in the 3D case the hail water content is still increasing after 60 minutes.

In the intermediate polluted case ($N_{CN} = 20000\,\mathrm{cm^{-3}}$) the results between the 3D and 2D cases are more similar then in the clean case. In both intermediate cases the delay of the rain formation and the combined formation of ice, snow and graupel can be observed. However, the formation of the frozen particles starts significantly earlier in the 3D case and also the delay of the rain formation is more pronounced in the 3D case.

The comparison of the 2D and 3D simulation of the strongly polluted case ($N_{CN} = 60000\,\mathrm{cm^{-3}}$) shows the largest agreement. In the beginning in both cases only ice and snow is formed due to the large amount of small cloud droplets. After that the formation of rain, graupel and hail is setting in. Nevertheless, in the 3D case the formation of ice and snow starts significantly earlier compared to the 2D case. Also the time gap between the formation of the small frozen hydrometeor classes (ice and snow) and the formation of rain, graupel and hail is larger and more pronounced in the 3D simulations.

In Fig. 4.31 the temporal evolution of the number of cloudy grid points and the

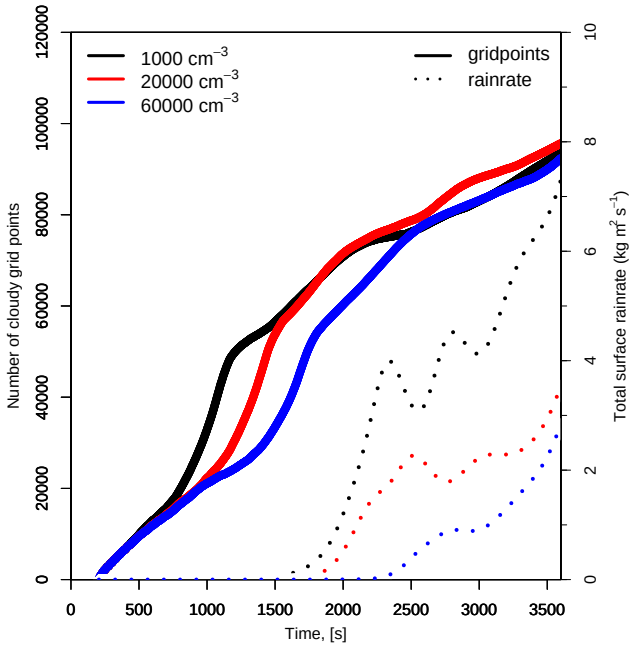

Figure 4.31: *Temporal evolution of (solid) the number of cloudy grid points for (black) an aerosol concentration of* $N_{CN} = 1000\,\mathrm{cm}^{-3}$*, (red)* $N_{CN} = 20000\,\mathrm{cm}^{-3}$ *and (black)* $N_{CN} = 60000\,\mathrm{cm}^{-3}$ *and (dashed) for the rain rate of the three specified aerosol concentrations. The time axis ends after* 60 *minutes.*

total surface rain rate for the three aerosol concentrations calculated with the 3D setup of ATHAM can be seen and compared to the 2D results (Fig. 4.22). Note that the absolute numbers of the grid points and rain rate are larger in the 3D case due to the larger model domain. Nevertheless, the comparison between the 2D and 3D results show a similar behaviour of the pyro-convective clouds. The rapid evolution of the cloud in the clean case starts first in both model setups and is followed by the intermediate polluted case. After 60 minutes the different polluted pyro-convective clouds show the same size of about 3000 grid points in the 2D case and 100000 grid points in the 3D case. Also the rain rate shows a similar behaviour in the 2D and 3D cases. Accordingly to the growth of the clouds the first precipitation reaching the ground can be observed in the clean case, followed by the intermediate and strongly polluted case. In contrast to the 2D case, where the rain rate is in the same order of magnitude after 60 minutes, the rain rate for the 3D clean case is twice as large compared to the more polluted cases.

Overall, the dependency of a pyro-convective cloud on the aerosol concentration is similar in the 2D and 3D setup of ATHAM. For low aerosol concentrations the

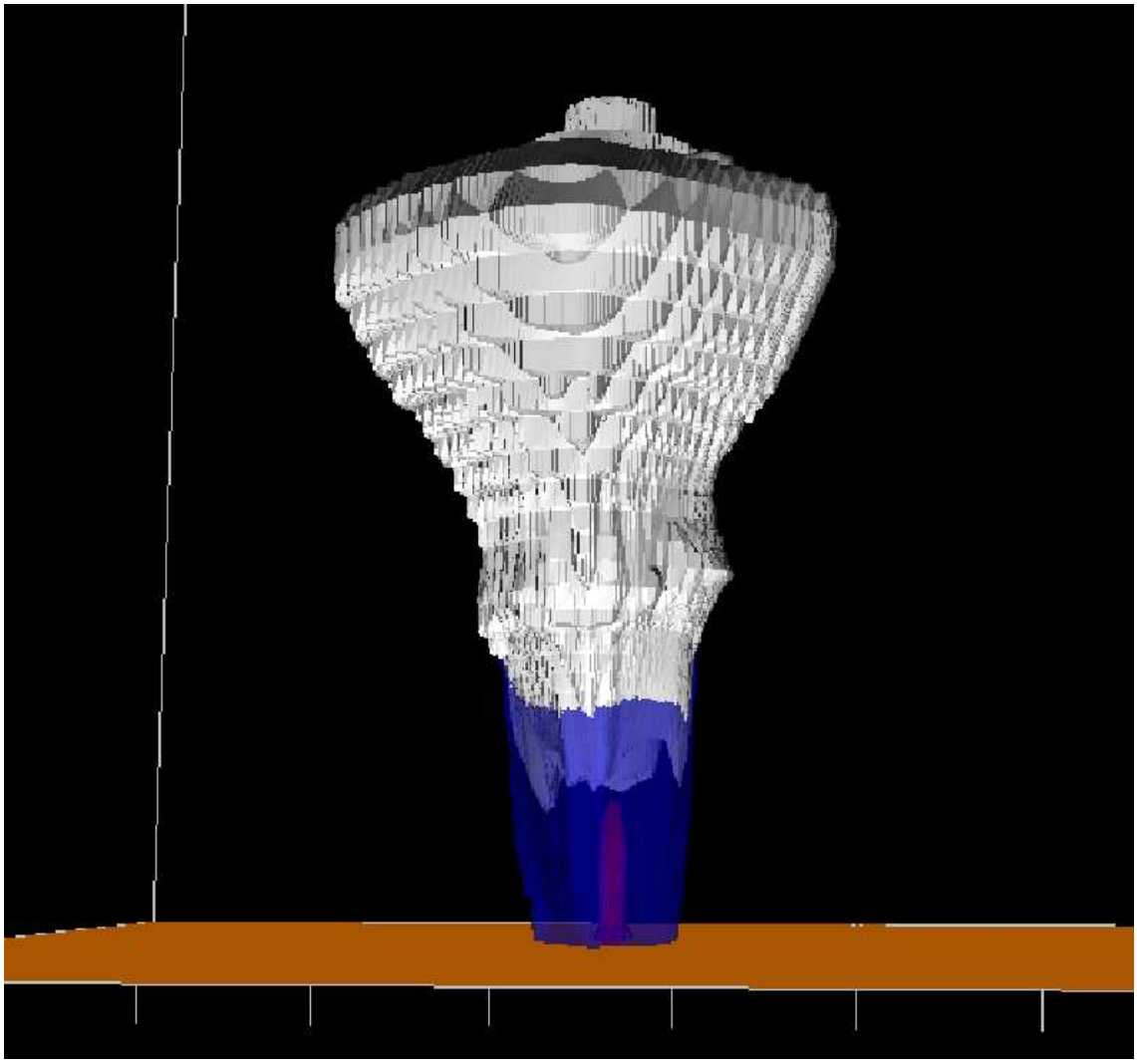

Figure 4.32: *3D model output after* 60 *minutes of model simulation for a mid-latitude US standard atmosphere with (white) the* $0.1\,\mathrm{g\,kg^{-1}}$ *isosurface of the hydrometeor content without rain, (blue) the* $0.1\,\mathrm{g\,kg^{-1}}$ *isoline of the rain water content and (red) the* 25° C *isosurface of the temperature indicating the location of the fire. The horizontal ticks are drawn every* 2 km.

contribution of warm microphysical processes is most important. The formation of rain for higher aerosol concentrations is delayed and the formation of ice and snow becomes more important for the evolution of the pyro-convective cloud. Nevertheless, 3D simulations should always be preferred and it is recommended to repeat all other sensitivity studies with a 3D setup of ATHAM.

Finally, Fig. 4.32 shows the 3D output of ATHAM for the strongly polluted case after 60 minutes calculated with the mid-latitude US standard atmosphere, which gives an impression of the distribution of the hydrometeors and precipitation of this pyro-convective cloud. Note, that the 3D results after 60 minutes of the other aerosol concentrations show a similar cloud, which is also indicated in Fig. 4.31.

4.7 Conclusions

In this Chapter the influence of the aerosol concentration on the dynamical and microphysical evolution of a pyro-convective cloud has been investigated. Therefore, a new two-moment microphysical scheme (Seifert (2002)) has been implemented into ATHAM. To study the influence of different aerosol concentrations on pyro-convective clouds a look-up table was included into the microphysical scheme based upon the results obtained from the parcel model in Chapter 2.

Sensitivity studies have been conducted with three different aerosol concentrations, namely a clean case ($N_{CN} = 1000\,\mathrm{cm}^{-3}$), an intermediate case ($N_{CN} = 20000\,\mathrm{cm}^{-3}$) and a strongly polluted case ($N_{CN} = 60000\,\mathrm{cm}^{-3}$). After 60 minutes of model integration the influence of the aerosol concentration on the dynamical evolution of a pyro-convective cloud is rather weak as far the cloud top height is concerned. In contrast, the aerosol concentration has a significant impact on the microphysical evolution of pyro-convective clouds. In the clean case rain forms rapidly by autoconversion of cloud droplets. Due to the low number concentration of aerosol particles and the high supersaturation produced by the strong updraft of a pyro-convective cloud, the cloud droplets are large and hence the autoconversion is an efficient process for rain formation. After that graupel and hail are formed within a short period of time. Hence, already at an early stage of the cloud life cycle a significant amount of water is transferred to the frozen phase, which leads to an additional release of latent heat that further intensifies the strong updraft region. The rain droplets, hail stones and graupel particles are growing fast and soon start to fall out. This precipitation processes is most pronounced for hail. This means that after 60 minutes of model integration a

large amount of water has been removed from the atmosphere.

In the intermediate pollution case the formation of rain is slower compared to the clean case. This is due to the fact that the higher aerosol concentration leads to more but smaller cloud droplets which reduces the effectivity of the autoconversion. Therefore, the formation of ice crystals and snow flakes becomes more important for the eventual formation of graupel, rain and hail. Compared to the clean case the freezing of water is delayed and therefore, also the rapid growth of the cloud. Nevertheless, hail starts to precipitate almost at the same time compared to the clean case.

In the strongly polluted case the formation of rain, graupel and hail is even more delayed compared to the previous case, because of the very small size of the cloud droplets in this case. After 26 minutes only cloud droplets, ice crystals and snow flakes can be seen with a significant amount. This leads to the latest formation of rain, graupel and hail in all three cases.

It can be concluded that the aerosol concentration has a small influence on the size of a pyro-convective cloud, but is very important for its microphysical evolution. For example, the onset of precipitation is delayed with increasing aerosol concentration. These results agree with the findings of other studies (e.g. Khain et al. (2005), Seifert and Beheng (2006b), Tao et al. (2007)). However, for the polluted cases in these previous studies an aerosol concentration not larger than $N_{CN} = 2500\,\mathrm{cm}^3$ using a model salt like sodium chloride was used. Although the combination of an aerosol concentration of $N_{CN} = 2500\,\mathrm{cm}^3$ with a model salt is an approximation for more polluted conditions, the result from this thesis are obtained by a realistic activation of aerosol particles to cloud droplets. Nevertheless, with proceeding time the differences in the microphysical structure are getting smaller and similar amounts of precipitation are formed, but with differing microphysical histories.

The influence of the ice nucleation ability plays an important role for the temporal evolution of a pyro-convective cloud. When the ability is zero, which means that only homogenous freezing is taken into account, the development of the cloud is clearly delayed because of the delay in the release of latent heat and hence the formation of precipitation. When the ice nucleation ability for mineral dust is used the differences in the results compared to the zero ability case are only small. However, for the ice nucleation ability of leaf litter, which is used for all other model runs in this chapter, the freezing and hence the formation of precipitation start much earlier.

The results of the sensitivity studies for three different aerosol concentrations have been repeated with a tropical US standard atmosphere and compared to the results

with a mid-latitude US standard atmosphere. It has been shown that the influence of the aerosol concentration on the development of a pyro-convective cloud is similar for both atmospheric profiles. In all simulations, the warmer and more humid atmosphere in the tropics leads to a stronger updraft velocity and more water is available in higher altitudes to freeze.

The sensitivity of the results to the strength of the fire has also been investigated. It can be concluded that the fire forcing has an important impact on the temporal evolution of a pyro-convective cloud. If the fire forcing is too weak only a small and thin cumulus cloud is forming that only contains cloud droplets. When the fire forcing is increased the size of the cloud is increased and the onset of freezing starts earlier. Above a certain threshold for the fire forcing, the microphysical structure of the pyro-convective clouds is very similar.

3D simulations of the influence of the aerosol concentration on the development on pyro-convective clouds using a mid-latitude atmospheric background profile support the results from the 2D simulations. The warm microphysical processes are more important for lower aerosol concentrations. For the stronger polluted cases the formation of rain is delayed and the formation of ice and snow becomes more important for the evolution of a pyro-convective cloud.

To conclude, the microphysical structure of a pyro-convective cloud is sensitive to the aerosol concentration in the atmosphere. A delay of precipitation occurs with increasing pollution. On the other side the size and the maximum altitude of these clouds are more sensitive to the atmospheric profile and the fire forcing than to the aerosol concentration.

Chapter 5

Conclusion and Outlook

The major goal of this thesis was to investigate, understand and quantify the influence of the aerosol concentration on the development of a pyro-convective cloud. Only few earlier studies did investigate cloud formation with exceptional high aerosol concentrations of up to $N_{CN} = 100000\,\mathrm{cm}^{-3}$. The results have been obtained using a hierarchy of numerical models. Therefore, this work was divided into three parts:

1. Study of the activation of aerosol particles to cloud droplets at the cloud base depending on the aerosol concentration, hygroscopicity of the particles, the size distribution and the updraft velocity (Chapter 2). These results were obtained by parcel model calculations and focused only on the activation processes at the cloud base.

2. Investigation of the microphysical processes within the smoky updraft region of a pyro-convective cloud. Therefore, a new technic was introduced, which couples the parcel model to the results of a 3D model (Chapter 3).

3. Detailed analysis of the dynamical and microphysical structure of pyro-convective clouds depending on the aerosol concentration, ice nucleation ability, atmospheric profile and emission of heat by the fire (Chapter 4). The Active Tracer High resolution Atmospheric Model (ATHAM), which is able to simulate eruptive events like a pyro-convective cloud, was used for 2-dimensional (preliminary 3-dimensional) model runs.

In Chapter 2 the initial cloud droplet number concentrations (N_{CD}) for a wide range of constant updraft velocities ($w = 0.25 - 20\,\mathrm{m\,s}^{-1}$) and aerosol particle number concentrations ($N_{CN} = 200 - 10^5\,\mathrm{cm}^{-3}$) at the cloud base were calculated. The

results can be classified into three regimes depending on the ratio between updraft velocity and aerosol number concentration (w/N_{CN}): (1) an aerosol-limited regime (high w/N_{CN}), (2) an updraft-limited regime (low w/N_{CN}) and (3) the transitional regime (intermediate w/N_{CN}). The results suggest that the variability of initial cloud droplet number concentration in (pyro-) convective clouds is mostly dominated by the variability of updraft velocity and aerosol particle number concentration in the accumulation mode. Coarse mode particles and the variability of particle composition expressed through the hygroscopicity parameter κ appear to play important roles only at very low supersaturation in the updraft-limited regime.

In Chapter 3 a new model approach was developed. The cloud parcel model from Chapter 2 was used to calculate a complete ascent of an air parcel over a wildland fire. The boundary conditions were obtained by model results using the 3D model ATHAM, which is developed to simulate eruptive events like wildland fires with a very high temporal and spatial resolution. This model approach allows to study the microphysical processes within the smoky updraft region of a pyro-convective cloud. It was shown that the cloud droplet number concentration is increasing with increasing aerosol number concentration, according to the results from Chapter 2. On the other hand, the size of the cloud droplets are decreasing with increasing aerosol concentration. The spectrum broadening, which means the growth of cloud droplets with height by coalescence and condensation of water vapor, is reduced when the aerosol concentration is increased, which is in agreement with measurements.

In Chapter 4 ATHAM was used to study the influence of the aerosol particle concentration on a pyro-convective cloud taking all microphysical processes into account. A state-of-the-art two-moment microphysical scheme (Seifert (2002)) was implemented in ATHAM and was expanded by a look-up table containing the results from the activation studies in Chapter 2. For a mid-latitude US standard atmosphere the dependence of a pyro-convective cloud on three different aerosol concentrations was investigated with 2-dimensional simulations. While the aerosol concentration plays only a minor role for the cloud top height and the size of the cloud, the microphysical structure clearly depends on the aerosol concentration. For clean conditions ($N_{CD} = 1000\,\mathrm{cm}^{-3}$) a rapid rain formation is followed by the appearance of graupel and hail. For intermediate conditions ($N_{CD} = 20000\,\mathrm{cm}^{-3}$) the formation of rain is slower, because the efficiency of the autoconversion is reduced by the smaller cloud droplets. This leads to an earlier formation of ice crystals and snow flakes, which is important for the formation of the larger frozen particles (graupel and hail) and rain. Compared to the previous

cases, the strongly polluted case ($N_{CD} = 60000\,\mathrm{cm}^{-3}$) shows the latest formation of rain, graupel and hail due to the very small size of the cloud droplets, leading to a delay in the onset of freezing. The results suggest that the aerosol concentration has an influence on how precipitation is formed. This sensitivity study was repeated with the 3-dimensional setup of ATHAM, which support results of the 2-dimensional simulations. With increasing aerosol concentration the onset of precipitation is delayed. This is also in agreement with other studies regarding aerosol-cloud-interactions. However, this is the first investigation of aerosol-cloud-interactions in pyro-convective clouds with the realistic activation of cloud droplets in situations of exceptional high aerosol number concentrations. Nevertheless, the number concentration is only one parameter of the aerosol particle composition. Other sensitivity studies regarding the influence of the size distribution and the hygroscopic composition will give additional insight into the overall effect of the aerosol particles on the dynamical and microphysical evolution of pyro-convective clouds. To do so, additional look-up tables created by the parcel model from Chapter 2 can be obtained.

Due to the high computational costs all following results are obtained with the 2-dimensional version of ATHAM. An important aspect of the development of a pyro-convective cloud is the freezing of water droplets. When leaf litter is assumed to act as an ice nucleation (IN), which is applicable for pyro-convective clouds, ice formation occurs much earlier compared to heterogeneous freezing with mineral dust aerosols or homogeneous freezing. The microphysical scheme, which was implemented into ATHAM, is a state-of-the-art two-moment microphysics with six different hydrometeor classes. Nevertheless, there are still uncertainties in many microphysical processes, especially the ice phase. For example the assumption of only one IN species is rather coarse and more information on the number and composition of IN is needed for a more accurate description of pyro-convective clouds. Therefore, additional studies of the freezing mechanism regarding the composition and number concentration of IN are suggested.

It is important to note that in the current version of ATHAM the aerosol number concentration is only used for the activation of cloud droplets. After the activation of the cloud droplets, it is assumed that the aerosol particles still remain in the atmosphere and not in the newly formed cloud droplet. Therefore, the aerosol number concentration is not reduced by microphysical processes and hence the scavenging of aerosol particles by the activation of cloud droplets and precipitation can not be investigated in this model version. However, this mechanism plays an important role for the distribution

of smoke in the atmosphere in biomass burning regions and should be included in upcoming model versions.

The studies on the sensitivity of pyro-convective clouds on the aerosol concentration were repeated for a tropical US standard atmosphere, which led to similar conclusions compared to the results obtained with a mid-latitude US standard atmosphere.

Also the influence of the strength of fire was investigated by varying the fire forcing between 10 and 1000 $\mathrm{kW\,m^{-2}}$. The fire forcing has a strong influence on the dynamical evolution of a pyro-convective cloud. For weak fire forcings only shallow convection is formed whereas for increasing fire forcings the cloud top height and size of the cloud is increasing and the onset of freezing and precipitation starts earlier. Nevertheless, the microphysical structure shows only a small dependency on the fire forcing.

The results presented in this study suggest that the aerosol concentration has a strong influence on the microphysical structure of pyro-convective clouds. This leads to a delayed formation of precipitation with increasing pollution. A temporal change of the formation of precipitation can also be caused by different ice nucleation abilities, which leads to a change in the onset of freezing. On the other side, the effect on the dynamical structure by the aerosol concentration and ice nucleation ability, as far the cloud top height and the size of the pyro-cloud is concerned, is only of minor importance. Here these two parameters are only important for the temporal evolution. For higher aerosol concentrations and lower ice nucleation abilities the growth of a pyro-convective cloud is delayed, but reaches the same dimensions later. For the dynamical structure the fire forcing as well as the atmospheric background profile is more important.

Nevertheless, more realistic conditions both in the tropics and mid-latitudes will be required to further quantify the relevance of the findings for pyro-convection in the real atmosphere.

Appendix A

Cloud Parcel Model

This appendix provides a brief description of the cloud parcel model by Martin Simmel (IfT Leipzig, Germany, Simmel et al. (2002), Simmel and Wurzler (2006), Diehl et al. (2006), Diehl et al. (2007)). Using a spectral microphysical scheme, this model is able to simulate microphysical processes within an ascending air parcel.

A well known handicap of this kind of model is the lack of the description of any form of precipitation. It would be possible to calculate the amount of particles falling out of the parcel but there is no information about particles falling into the parcel. Therefore the presented parcel model stops whenever particles fall out of the parcel. Nevertheless, for the activation studies in Chapter 2 that focus on the processes at the cloud base, this issue is not influencing the results.

A.1 Setup of the parcel model

The code of the parcel model can be found in the folder qu_mxd_vs2. It is written in the Fortran 90 language. Also an additional folder named *Rundir* is needed, containing the namelist and the model output. When starting a new model simulation, the main changes are required in the namelist file *initial* and in the running script mk_laufe_schieb which are described in the following.

A.1.1 Namelist

In the namelist file *initial* different setups of the model can be chosen by changing the corresponding parameters. The most important parameters are described here with exemplary values:

```
DELTAT   = 0.1D0
```

is the timestep in seconds;

```
TIMMAX   = 9500.D0,
```

the maximum run time. If the air parcel stops ascending before TIMMAX is reached, the run is halted.

```
INCOUT   = 20.D0
```

is the time increment for the input and output which are controlled by the routines read_write.f90 and print.f90 respectively.

```
DELT0  = 3.0D0
```

denotes the temperature difference between the air parcel and the environment at the beginning of a run. This temperature difference leads to a positive buoyancy and therefore to an upward motion of the air parcel. For model runs of the activation study (Chapter 2) this value was set to zero, because the updraft velocity was prescribed in the script *mk_laufe_schieb*.

```
iread  = 0
```

is used if a new run is started, for iread = 1 the data from a previous run is used as the initial conditions. The parameters

```
iap_p  = 8
iap_e  = 9
```

determine the aerosol size distribution, which is specified in the file *ap_new.f*90, where the letter p denotes the aerosol distribution of the parcel and e of the environment. For

```
ientr  = 0
```

no entrainment is calculated during the model run, for a value of 1 full entrainment is assumed and for a value of 2 only detrainment of particles larger than $1 \cdot 10^{-6}\,\mu$m is considered.

`icond = 4`

determines what kind of Köhler scheme is used. This is one of the most important parameters for the studies on the activation of CCN. The most detailed Köhler scheme with the osmotic coefficient (OS) model (see Section 2.2.2) is used by setting icond = 1. For this scheme, the equilibrium water vapor saturation ratio has the form

$$s_{eq} = \exp\left(\frac{2 \cdot (a_{sig} + B \cdot \mathfrak{M})}{\rho_w \cdot R_w \cdot T \cdot r_{wet}} - \left(\mathfrak{M} \cdot \nu \cdot \frac{M_w}{1000} \cdot \Phi_s\right)\right) - 1, \tag{A.1}$$

with a_{sig} the temperature dependent surface tension, B the specific surface tension coefficient ($0.67 \cdot 10^{-3}$ for ammonium sulfate and $1.64 \cdot 10^{-3}$ for sodium chloride, see eq 5-19 in Pruppacher and Klett (1997)), $\mathfrak{M}$ the molality, $\rho_w = 1000\,\mathrm{kg\,m^{-3}}$ the density of water, $R_w = 461.5\,\mathrm{J\,kg^{-1}\,K^{-1}}$ the specific gas constant for water, T the absolute temperature, r_{wet} the radius of the droplet, ν the stoichiometric dissociation number (the number of ions, into which a salt molecule dissociates), $M_w = 18.015 \cdot 10^{-3}\,\mathrm{kg\,mol^{-1}}$ the molecular weight of water and Φ_s the osmotic coefficient. The osmotic coefficient is set through *iideal* (see below). If icond = 4 the κ-Köhler scheme is used in the following form

$$s_{eq} = \left(\exp\left(\frac{2 \cdot (a_{sig} + B \cdot \mathfrak{M})}{\rho_w \cdot R_w \cdot T \cdot r_{wet}}\right) - \left(1 + \kappa \frac{V_s}{V_w}\right)^{-1}\right) - 1, \tag{A.2}$$

where κ and V_s are the effective hygroscopicity parameter and the volume of dry particulate matter ($V_s = \frac{4}{3}\pi r_s^3$, with r_s the radius of the particles) respectively and V_w is the volume of water in the aqueous particle/droplet ($V_w = \frac{4}{3}\pi r_w^3$, with r_w the radius of the wet fraction).

`ikoll = 0`

indicates that no collision of particles within the air parcel are assumed. For the activation studies in Chapter 2 the influence of collision-coalescence was very small and therefore was neglected. The switch

`iideal`

determines whether an ideal solution is assumed (which leads to $\Phi_s = 1$ for iideal = 0) or whether Φ_s is calculated by equation 4-70 and table 4.2 in Pruppacher and Klett (1997) for $iideal = 1$ or by equation A16 in Rose et al. (2008a) for $iideal = 2$.

For a description of all namelist parameters see the file $info.txt$.

A.1.2 Execution of the parcel model

To obtain the results for Chapter 2 a large number of model runs had to be conducted. Therefore the model has been installed on the Linux cluster at the University of Mainz. To run the model wolke.x a shell script in the following form has been used:

```
 #!/bin/bash
for WIND in 0.5 0.75 1.0 1.25 1.5 1.75 2.0 2.25 2.5 2.75 3.0
  do
  for AP in 200 400 800 1000 2000 3000 4000 5000
    do
    for KAPPA_K in 0.1 0.2 0.3 0.4 0.5
      do

echo  $WIND $AP $KAPPA_K submitted
mkdir ${WIND}_${AP}_${KAPPA_K}}
cp ~/MODELS/MOSI/qu_mxd_vs2/wolke.x  ${WIND}_${AP}_${KAPPA_K}
cp ~/MODELS/MOSI/Rundir/initial  ${WIND}_${AP}_${KAPPA_K}
cd ${WIND}_${AP}_${KAPPA_K}
bsub -q short -W 3:00 -e error.err -o info.inf wolke.x $WIND $AP $KAPPA_K
cd ..

      done
   done
done
```

This exemplary script shows three loops over the parameters $WIND$ corresponding to the constant updraft velocity w, AP corresponding to the number of aerosol particles N_{CN} and $KAPPA\_K$ denoting the κ value. For each model run a directory is created where the output is saved.

A.2 Sensitivity on numerical parameters

The results of numerical models are typically sensitive to the choice of different numerical parameters such as temporal and spatial resolution. Therefore the ideal setup for each investigation has to be found by varying these parameters. In the case of this cloud parcel model the important parameters are

- time step Δt
- bin resolution
- weighting coefficient wei_q.

In the following, the results of each sensitivity study are discussed.

A.2.1 Sensitivity on timestep Δt

The timestep Δt determines the length of the integration time. The longer the timestep, the less integration steps are required for one parcel model run. On the one side the advantage is that less rounding errors are made. On the other side it is possible that due to the coarse temporal resolution important features are missed or not properly resolved, for instance rapid processes at the cloud base in the case of high updraft velocities. It also has to be kept in mind that a small timestep will lead to higher computational costs, which becomes important if a lot of model runs are required (as it is the case in Chapter 2).

The sensitivity study of the cloud droplet number concentration N_{CD} on the the timestep ΔT showed, that the results are rather robust in the range of 0.005 and 0.1. Thus it was decided that for the activation studies in Chapter 2 a timestep of 0.01 s is used in order to have a sufficiently small timestep to properly cover the processes at the cloud base.

A.2.2 Sensitivity on number of size bins

The number and width of the size bins also has an influence on the results, as shown in Fig. A.1. The black solid line shows the number of cloud droplets as a function of the number of bins for a constant vertical velocity of $w = 3.0\,\mathrm{m\,s^{-1}}$ and an aerosol number concentration of $N_{CN} = 3000\,\mathrm{cm^{-3}}$. A weak minimum can be seen at 528 bins, whereas the highest cloud droplet concentration can be found for the lowest resolution with 66 bins. The blue dashed line shows the result for a constant updraft velocity of $w = 6.0\,\mathrm{m\,s^{-1}}$ and an aerosol number concentration of $N_{CN} = 30000\,\mathrm{cm^{-3}}$. The sensitivity in this case is much more pronounced compared to the clean case described before. Again, the minimum of the cloud droplet concentration can be found for 528 bins. To have an adequate spectral resolution without paying the price of high computational costs, it was decided to use 264 bins, which leads to cloud droplet activation close to the mean value of the performed sensitivity studies.

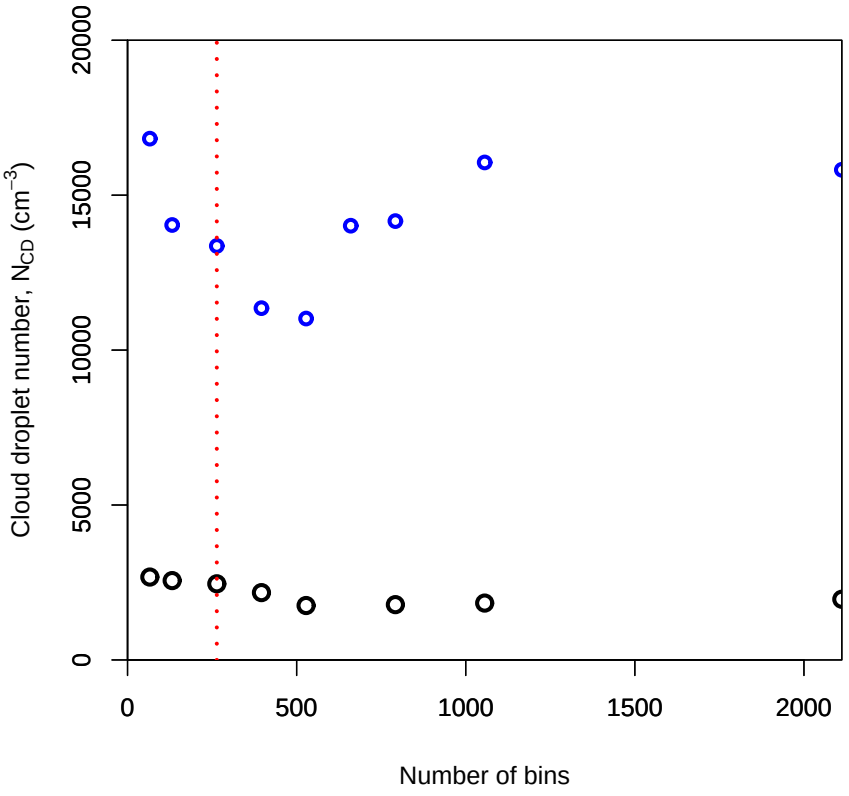

Figure A.1: *Sensitivity of cloud droplet number concentration N_{CD} on the number of size bins for a constant vertical velocity of (black) $w = 3.0\,\mathrm{m\,s^{-1}}$ and an aerosol number concentration of $N_{CN} = 3000\,\mathrm{cm^{-3}}$ and (blue) $w = 6.0\,\mathrm{m\,s^{-1}}$ and an aerosol number concentration of $N_{CN} = 30000\,\mathrm{cm^{-3}}$. For both cases the hygroscopicity parameter κ was set to 1.28 representing sodium chloride. The aerosol size distribution is the same as specified by Segal and Khain (2006). The red dotted line marks the number of bins used for the activation study in Chapter 2.*

A.2.3 Sensitivity on weighting coefficient wei_q

The weighting coefficient is a determines in which way particulate mass is shifted to the next bin during the growth or shrinking of the particles. In the calculation presented in Chapter 2 all particles are classified according to their water mass on a fixed grid (Eulerian approach). A particle with the mass x will be in bin k if

$$x_k \leq x \leq x_{k+1} \tag{A.3}$$

with $x_{k+1} = px_k$, where p denotes the grid resolution factor (bin width). For the presented studies it was set to $2^{\frac{1}{4}}$. The first bin starts at $x_1 = (\frac{4}{3})\pi r_1^3 \rho_1$ with $r_1 = 1\,\mathrm{nm}$ and $\rho_1 = 1000\,\mathrm{kg\,m^{-3}}$ (Simmel and Wurzler, 2006).

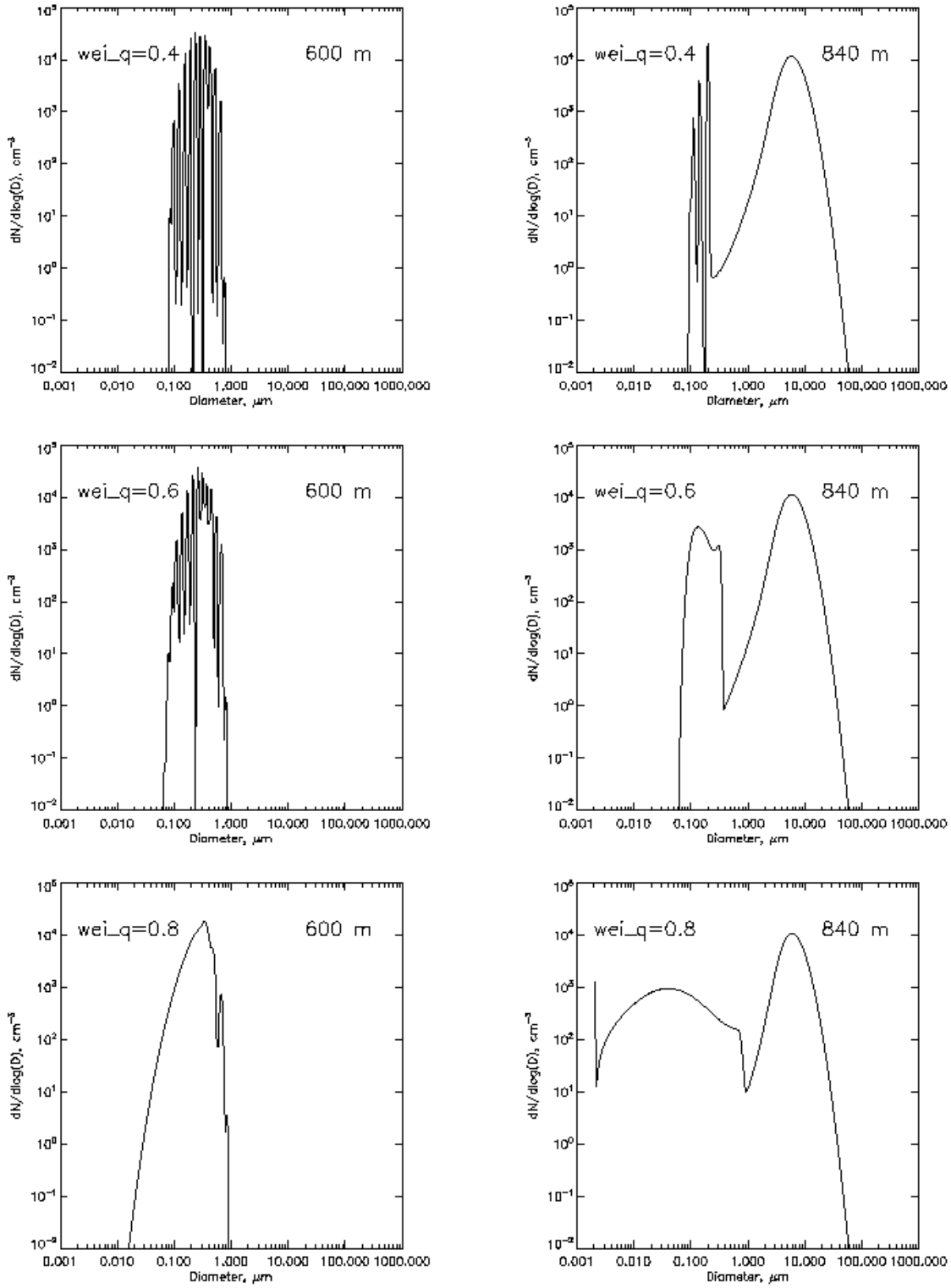

Figure A.2: *Sensitivity of the evolution of the particle number size distribution to the weighting coefficient wei_q. The pictures at the top are for $wei_q = 0.4$, in the middle for $wei_q = 0.6$, and at the bottom for $wei_q = 0.8$. The left and right columns show the particle size distribution after the initialization of the model at a height of* 600 m *and at a height of* 840 m *within the cloud, respectively. The results were obtained with a timestep of* $\Delta t = 0.01$ s *and* 264 *bins for a constant vertical velocity of* $w = 3.0\,\mathrm{m\,s^{-1}}$ *and an aerosol number concentration of* $N_{CN} = 3000\,\mathrm{cm^{-3}}$. *The hygroscopicity parameter* κ *and the aerosol size distribution are the same as used in Fig. A.1.*

The basic equation for the prognostic variables *particle mass* and *water mass* can be described as the 0th and 1st moments of the distribution function $n(x,t)$ in bin k defined as

$$M_k^l = \int_{x_k}^{x_{k+1}} x^l n(x,t) \mathrm{d}x \text{ with } l = 0, 1. \tag{A.4}$$

The soluble and total aerosol masses are evaluated as well in each size bin and are treated as passive tracers. These two passive tracers can be treated in different ways, where two limiting cases appear.

The first limiting case is to shift the particulate (soluble or total aerosol) mass proportionally to the water mass, which corresponds to the assumption of a constant particulate mass concentration within the bin.

The second limiting case is obtained by shifting the particulate mass proportionally to the number concentration which corresponds to a constant mass of each particle.

As mentioned by Simmel and Wurzler (2006) there are no physical arguments to decide between these two limiting cases. Therefore a linear superposition with the weighting factor $0 \leq wei_q \leq 1$ was introduced in the model to cover the range between the limiting cases. For larger wei_q more particulate mass is shifted proportionally to the water mass. This parameter is set in the file *konst.f*90.

This weighting factor wei_q has an important effect on the results for the presented activation studies. Therefore a sensitivity study was conducted to evaluate the effects and to determine the best choice for the requirements of the study. Figure A.2 shows the influence of wei_q on the evolution of the particle number size distribution with height.

For $wei_q = 0.4$ it can be seen, that the initialization of the size distribution (top left) shows oscillations. As discussed by Simmel and Wurzler (2006) these oscillations occur only in the non-activated part of the spectrum and are due to overestimating the concentration gradient within the bins. This effect is largest for high spectral resolution and small wei_q, which is the case here. For the particle size distribution within the cloud (top right) the oscillation is only visible for the non-activated particles.

The results for $wei_q = 0.6$ in the middle of Fig. A.2 show also the oscillations right after the initialization, but with a smaller amplitude. For the particle size distribution within the cloud no oscillation can be observed.

For $wei_q = 0.8$ (Fig. A.2 bottom) almost no oscillations occur during the initialization and within the cloud. However, it can be seen that the particle size distribution

is growing to smaller particles, which is not physical because there are no processes enabled in this model run that could explain this feature.

Based on this sensitivity analysis a weighting coefficient of $wei_q = 0.6$ was chosen for all model runs.

A.2.4 Final setting of numerical parameters

Table A.1 shows the range of the tested parameters and the optimum choice, which was used for the simulations in this study.

	Tested range		best choice
	from	to	
timestep Δt	0.0001 s	0.1 s	**0.01 s**
number of bins	66	2112	**264**
wei_q	0.4	0.8	**0.6**

Table A.1: *Summary of the tested numerical parameters of the parcel model. The best choice values are used for the model runs in this study.*

Appendix B

ATHAM

During the implementation of the two-moment microphysical scheme by Axel Seifert (see Section 4.3) several problems and caveats were found. In the following the proceeding for some issues are shown.

B.1 Fire emissions

In the default version of the model the fire emissions of heat, water vapor and aerosol mass started with full intensity at the very first timestep. Since the initial state of the atmosphere does not include the fire effects, this implementation of the fire forcing creates very strong horizontal and vertical gradients right at the beginning of the model run. In order to allow for a more subtle model initialization, the fire emissions were strongly increased during the first model time steps. This was realized by introducing a timestep dependent coefficient *ramp* that acts as a factor for all fire emissions

$$ramp = \mathrm{MIN}\left(\frac{timestep}{\tau_{fire}}, 1\right). \tag{B.1}$$

Here *timestep* is the number of the current time steps and τ_{fire} the time step, after which the fire emissions operate with full intensity. For example a value of $\tau_{fire} = 80$ means that the fire emissions of heat, water vapor and aerosol are increased during the first 80 time step after the model start. Figure B.1 shows the effect of the *ramp* coefficient for the heat flux per second in the center of the fire and with $\tau_{fire} = 80$. The choice of 80 time step is more or less arbitrary.

With this ramp coefficient, the startup of the fire and its corresponding emissions is now represented in a more subtle way.

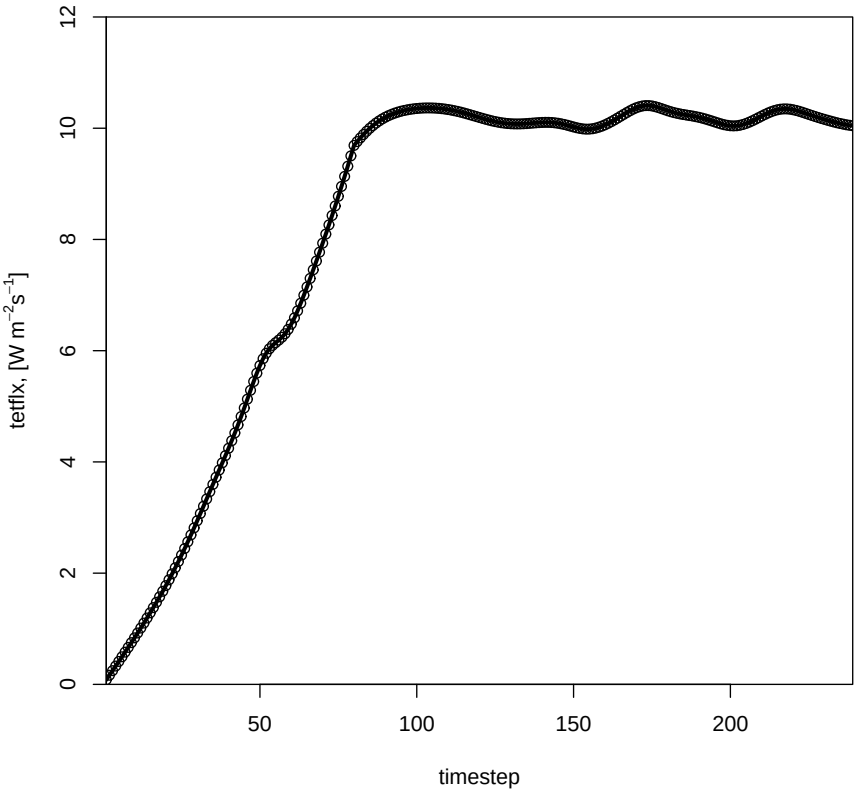

Figure B.1: *Development of the heat emission in the center of the fire with time with* $\tau_{fire} = 80$. *Tetflx is representing the emission of potential temperature per second and kg fuel burned.*

B.2 Undershoot of temperature next to the fire

In the first 2D test runs a problem occurred on the first model levels in the vicinity of the fire. After the first few timesteps cloud water formed at the grid points to the left and right of the center of the fire. The cause of this problem is shown in Fig. B.2 (a). The fire creates a strong horizontal temperature gradient on the lower model levels. Due to this strong gradient, the advection scheme produces undershoots of the temperature in the surrounding of the fire. These undershoots in the temperature field are so large that supersaturation occurs leading to the activation of cloud droplets. The vertical velocity in this area is weakly positive or even negative (downward motion). Because the activation rate of the Seifert scheme is proportional to the updraft velocity only a minimum value of cloud droplets are activated. The few cloud droplets are growing quite fast and even form rain droplets, which are transported into the region of high

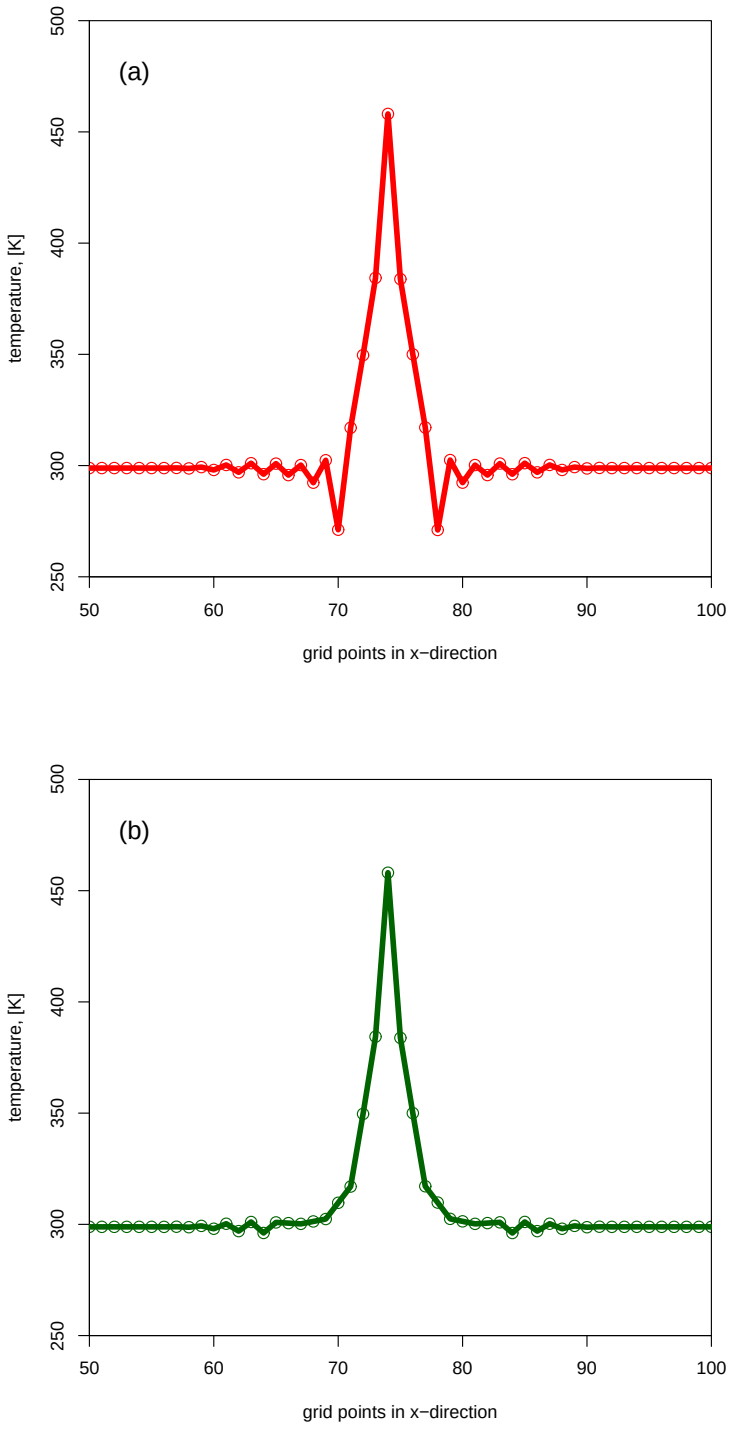

Figure B.2: *Cross section of temperature T in K on the second model level for (a) without temperature smoothing and (b) with temperature smoothing. The peak of the temperature represents the center of the fire emissions.*

updraft velocities.

This unrealistic behaviour of the model was avoided by scanning the temperature field for negative anomalies. A grid point is recognized as an undershoot when the temperature at this grid point is lower than 3 K compared to the neighboring grid points. If this is the case the temperature value is replaced by the mean value calculated from the neighboring grid points. The result of this smoothing can be seen in Fig. B.2 (b). The procedure is only done for temperature undershoots, which means that high temperatures near the fire are not effected .

The smoothing is done in every time step before the calculation of the microphysical processes. Thereafter, the temperature is set to the original values.

B.3 A problem with the saturation adjustment in the old two-moment scheme

After the implementation of the Seifert scheme into ATHAM, it was compared to the old two-moment scheme. When the problems with the undershooting temperature in the Seifert scheme were solved, the old and new schemes agreed well in the location and shape of the cloud. Figure B.3 shows the resulting contour lines of $0.001\,\mathrm{g\,kg^{-1}}$ of liquid water content for both schemes after five minutes of simulation time and one minute of cloud life time. It can be seen that the shape of the cloud matches almost perfectly.

Unfortunately, the comparison between the two different microphysical schemes regarding the total liquid water content showed large differences. The liquid water content is a very useful variable to compare two different microphysical schemes because at the beginning of a developing cloud only cloud droplets are existing. Independent of the cloud droplet concentration, in the early stage of a cloud the amount of liquid water in the cloud droplet class should be of comparable magnitude for both schemes.

Figures B.4 and B.5 show the liquid water content in $\mathrm{g\,kg^{-1}}$ of the cloud calculated with the Seifert and the old two-moment scheme, respectively. The old scheme has a significant higher liquid water content of up to 30 % already after a cloud life time of about one minute.

The reason for this large difference is a problem with the saturation adjustment in the old scheme. The saturation adjustment is always the last step within a microphys-

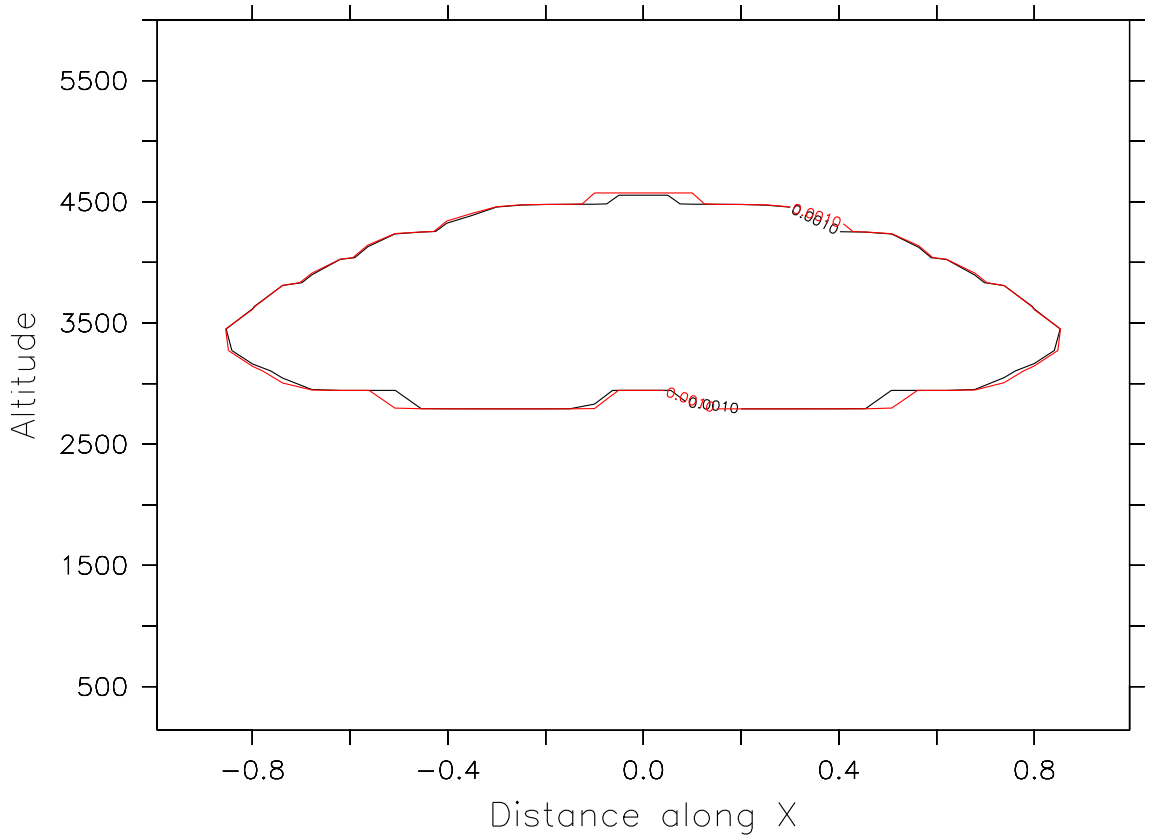

Figure B.3: *Contour line of* $0.001\,\mathrm{g\,kg^{-1}}$ *liquid water content for (black) Seifert scheme and (red) old two-moment scheme after 5 minutes of simulation time.*

ical scheme and it sets the relative humidity to 100 % within clouds. This means that for a supersaturated grid point at the end of the microphysical module the remaining water vapor is added to the water mass in the cloud droplet class. For subsaturated cloudy grid points the cloud water is evaporated until a relative humidity of 100 % is reached.

In Fig. B.6 the temporal evolution of the supersaturation is shown for the two different microphysical schemes at one exemplary grid point in the cloud. In black the results of the Seifert scheme are shown where the solid line denotes the supersaturation at the beginning of the timestep and the dashed line the supersaturation after the microphysics subroutine. It can be clearly seen that the supersaturation is reduced to zero after each timestep which is the expected effect of the saturation adjustment.

In contrast, the red lines corresponding to the saturation adjustment of the old microphysical scheme show a quite different behaviour. Again the solid line corresponds to the supersaturation at the beginning of the microphysical module. In this case the

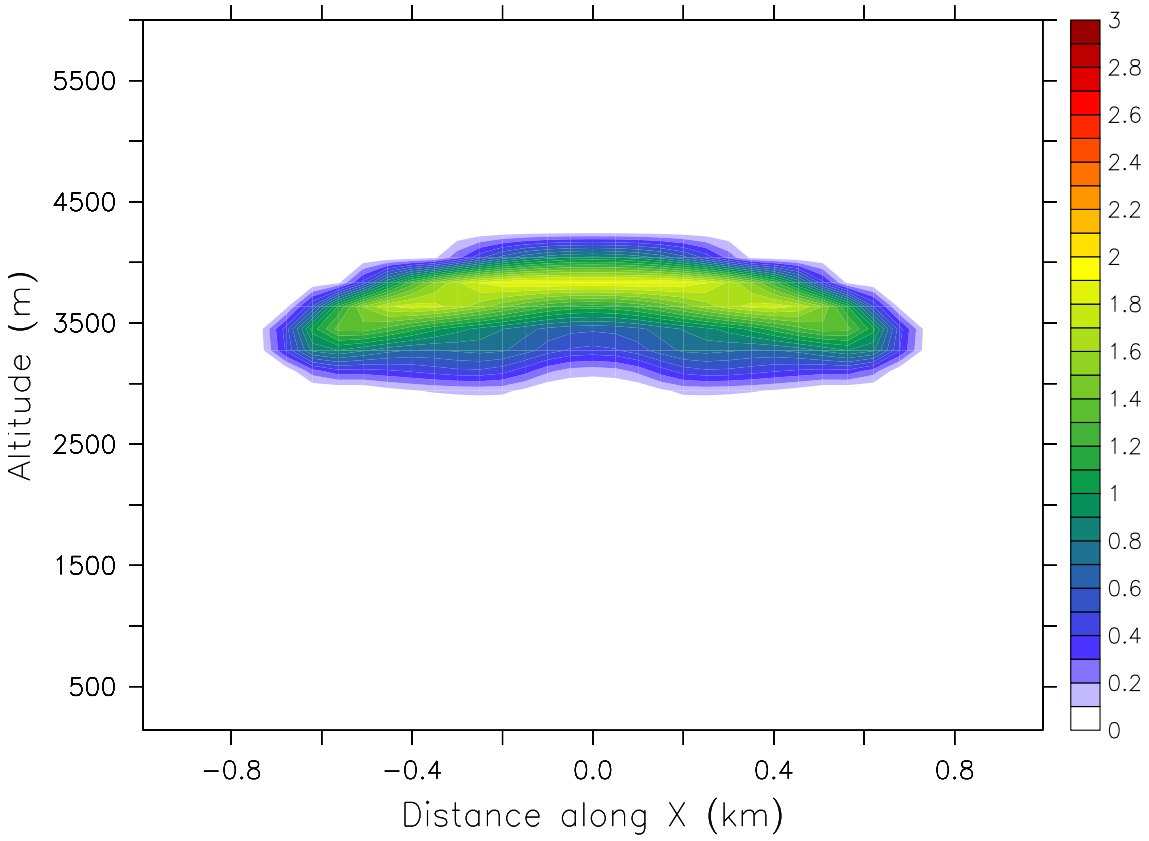

Figure B.4: *X-Z cross section of the liquid water content in* $\mathrm{g\,kg^{-1}}$ *calculated with the Seifert scheme after 5 minutes of model integration.*

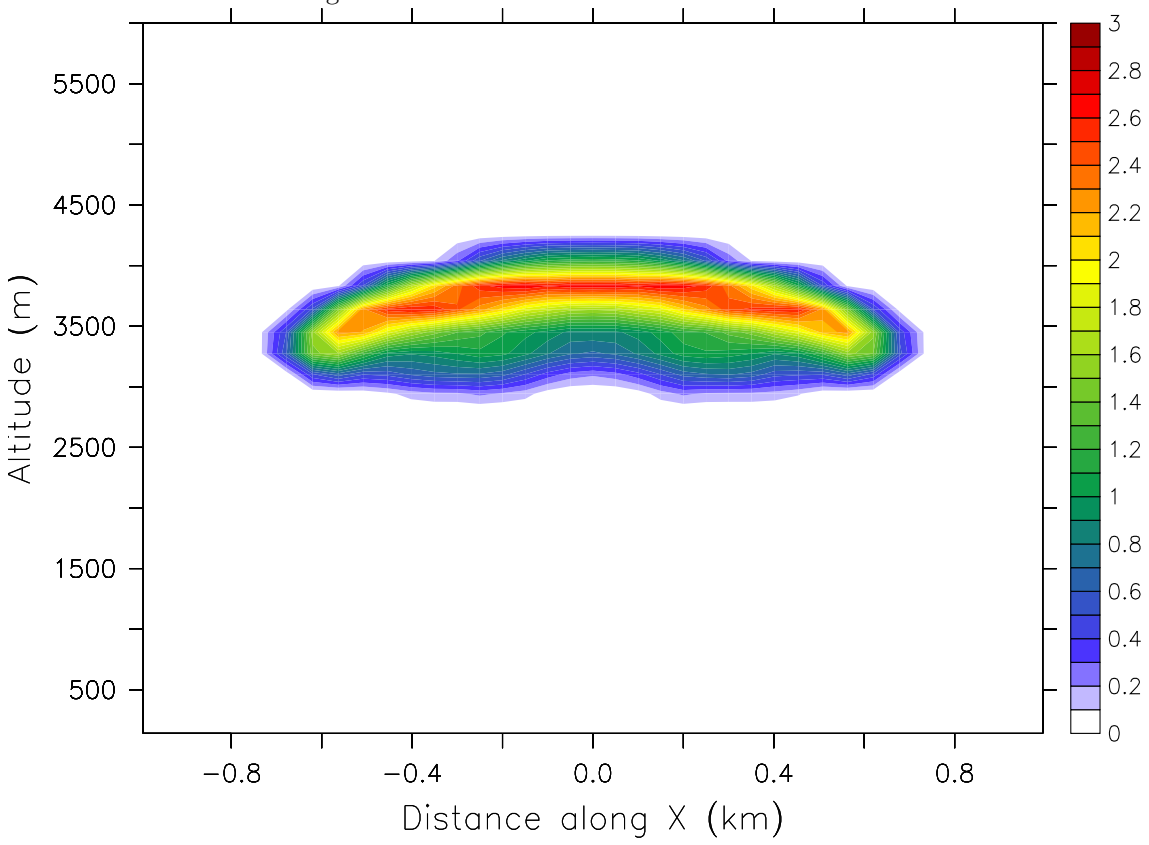

Figure B.5: *X-Z cross section of the liquid water content in* $\mathrm{g\,kg^{-1}}$ *calculated with the old two-moment scheme after 5 minutes of model integration.*

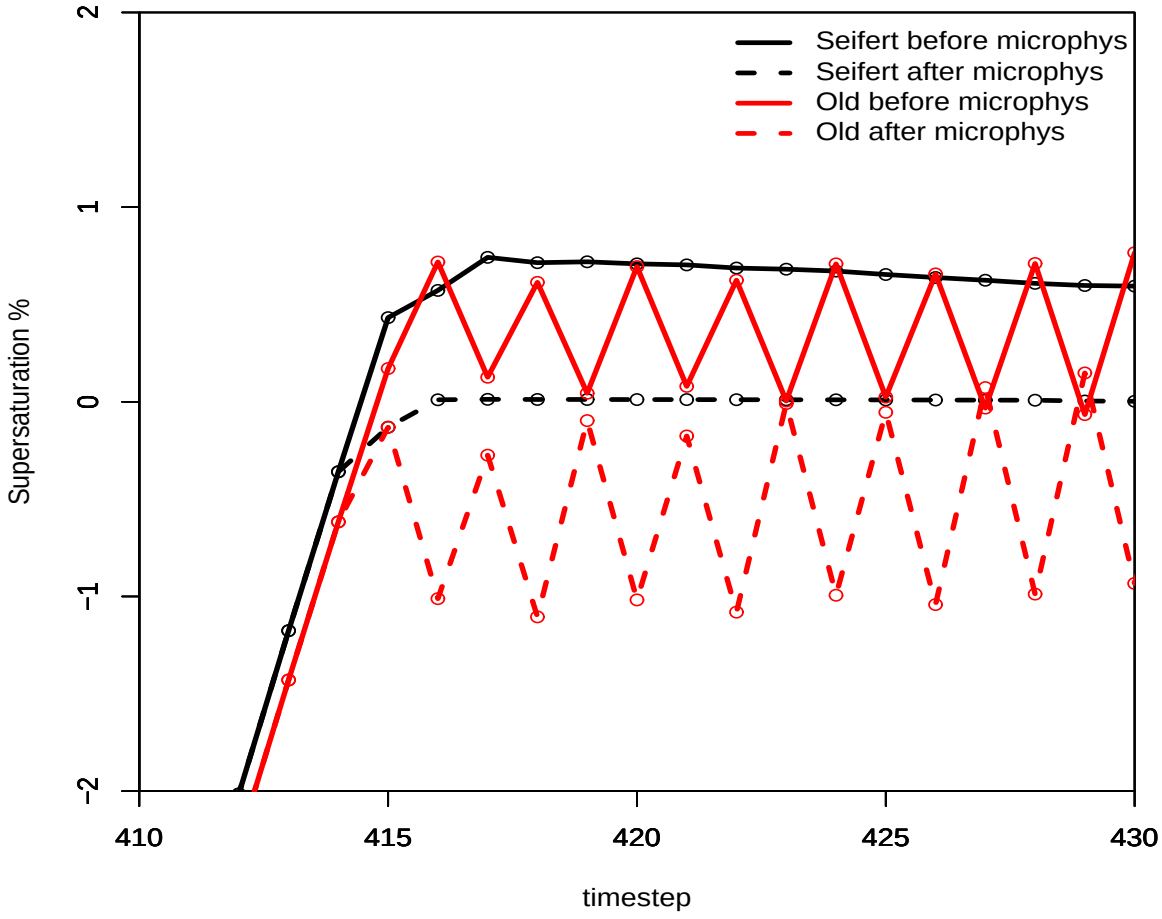

Figure B.6: *Time-series of supersaturation at an exemplary grid point in % (solid) at the beginning and (dashed) at the end of the microphysical model for (black) the Seifert scheme and (red) the old two-moment scheme.*

values of the supersaturation are oscillating with each timestep. The reason for this unrealistic description of the supersaturation lies in the saturation adjustment at the end of the old two-moment scheme module, because it is reducing the supersaturation too strongly. The difference between the supersaturation at the beginning and at the end is transferred as liquid water to the cloud droplet class. Due to the overestimated reduction of the supersaturation, the cloud calculated with the old scheme is producing too much liquid water, which can be seen in Fig. B.5.

The oscillating behaviour of the old scheme in Fig. B.6 also has its origin in the overestimated reduction of the supersaturation. When the supersaturation is wrongly

adjusted the very same grid point is only slightly supersaturated in the next timestep. Because the error in the reduction is proportional to the supersaturation at the beginning, the error is smaller after that timestep which leads again to a higher supersaturation in the following. This leads to the observed oscillation of the supersaturation.

Due to the reasons listed in Section 4.2.2 the correction of the saturation adjustment of the old two-moment scheme was omitted and all further simulations in this study are conducted using the Seifert scheme.

List of Figures

Bibliography

Altaratz, O., Koren, I., Reisin, T., Kostinski, A., Feingold, G., Levin, Z., and Yin, Y.: Aerosols' influence on the interplay between condensation, evaporation and rain in warm cumulus cloud, Atmos. Chem. Phys., 8, 15–24, 2008.

Andreae, M. O. and Rosenfeld, D.: Aerosol-cloud-precipitation interactions, Part 1: The nature and sources of cloud-active aerosols, Earth Sci. Rev., 89, 13–41, doi: 10.1016/j.earscirev.2008.03.001, 2008.

Andreae, M. O., Artaxo, P., Fischer, H., Freitas, S. R., Gregoire, J.-M., Hansel, A., Hoor, P., Kormann, R., Krejci, R., Lange, L., Lelieveld, J., Lindinger, W., Longo, K., Peters, W., de Reus, M., Scheeren, B., Silva Dias, M. A. F., Ström, J., van Velthoven, P. F. J., and Williams, J.: Transport of biomass burning smoke to the upper troposphere by deep convection in the equatorial region, Geophys. Res. Lett., 28, 951–954, 2001.

Andreae, M. O., Rosenfeld, D., Artaxo, P., Costa, A. A., Frank, G. P., Longo, K. M., and Silva-Dias, M. A. F.: Smoking Rain Clouds over the Amazon, Science, 303, 1337–1342, 2004.

Arakawa, A. and Lamb, V. R.: Computational design of the basic dynamical processes of the ucla general circulation model, in *General circulation models of the atmosphere*, pp. 173-265, Academic Press, New York, 1977.

Asa-Awuku, A., Engelhart, G. J., Lee, B. H., and Pandis, S. N.: Relating CCN activity, volatility, and droplet growth kinetics of β-caryophyllene secondary organic aerosol, Atmos. Chem. Phys., 9, 895–812, 2009.

Bigg, E. K.: The formation of atmospheric ice crystals by the freezing of droplets, Q. J. R. Meteorol. Soc., 79, 510–519, 1953.

Cammas, J.-P., Brioude, J., Chaboureau, J.-P., Duron, J., Maril, C., Mascart, P., Nedelec, P., Smit, H., Pätz, H.-W., Volz-Thomas, A., Stohl, A., and Fromm, M.: Injection in the lower stratosphere of biomass fire emissions followed by long-range transport: a MOZAIC case study, Atmos. Chem. Phys., 9, 5829—5846, 2009.

Chuang, C. C., Penner, J. E., and Edwards, L. L.: Nucleation Scavenging of Smoke Particles and Simulated Drop Size Distributions over Large Biomass Fires, J. Atmos. Sci., 49, 1264–1275, 1992.

Costa, A. A., de Oliveira, C. J., de Oliveira, J. C. P., and da Costa Sampaio, A. J.: Microphysical observations of warm cumulus clouds in Ceara, Brazil, Atmos. Res., 54, 167–199, 2000.

Cubison, M. J., Ervens, B., Feingold, G., Docherty, K. S., Ulbrich, I. M., Shields, L., Prather, K., Hering, S., and Jimenez, J. L.: The influence of chemical composition and mixing state of Los Angeles urban aerosol on CCN number and cloud properties, Atmos. Chem. Phys., 8, 5649–5667, 2008.

Cunningham, P. and Reeder, M. J.: Severe convective storms initiated by intense wildfires: Numerical simulations of pyro-convection and pyro-tornadogenesis, Geophys. Res. Lett., 36, doi:10.1029/2009GL039262, 2009.

Diehl, K., Simmel, M., and Wurzler, S.: Numerical sensitivity studies on the impact of aerosol properties and drop freezing modes on the glaciation, microphysics, and dynamics of clouds, J. Geophys. Res., 111, D07202, doi:10.1029/2005JD005884, 2006.

Diehl, K., Simmel, M., and Wurzler, S.: Effects of drop freezing on microphysics of an ascending cloud parcel under biomass burning conditions, Atmos. Environ., 41, 303–314, 2007.

Dusek, U.: Size matters more than chemistry for cloud nucleating ability of aerosol particles, Science, 312, 1375 – 1378, 2006.

Ekman, A. M. L., Krejci, R., Engstrom, A., Ström, J., de Reus, M., Williams, J., and Andreae, M. O.: Do organics contribute to small particle formation in the Amazonian upper troposphere?, Geophys. Res. Lett., 35, doi:10.1029/2008GL034970, 2008.

Engelhart, G. J., Asa-Awuku, A., Nenes, A., and Pandis, S. N.: CCN activity and droplet growth kinetics of fresh and aged monoterpene secondary organic aerosol, Atmos. Chem. Phys., 8, 3937–3949, 2008.

Ervens, B., Feingold, G., and Kreidenweis, S. M.: The influence of water soluble organic car-bon on cloud drop number concentration, J. Geophys. Res., 110, D18211, doi: 10.1029/2004JD005634, 2005.

Feingold, G.: Modeling of the first indirect effect: Analysis of measurement requirements, Geophys. Res. Lett., 30(19), doi:10.1029/2003GL017967.

Feingold, G. and Siebert, H.: Cloud-aerosol interactions from the micro to cloud scale, edited by: Heintzenberg K. and Charslon, R. J., MIT Press Cambridge, pp. 319–338, 2009.

Fromm, M., Alfred, J., Hoppel, K., Hornstein, J., Bevilacqua, R., Shettle, E., Servranckx, R., Li, Z., and Stocks, B.: Observations of boreal forest fire smoke in the stratosphere by POAM III, SAGE II, and lidar in 1998, Geophys. Res. Lett., 27, 1407–1410, 2000.

Fromm, M., Bevilacqua, R., Servranckx, R., Rosen, J., Thayer, J. P., Herman, J., and Larko, D.: Pyro-cumulonimbus injection of smoke to the stratosphere: Observations and impact of a super blowup in northwestern Canada on 3–4 August 1998, J. Geophys. Res., 110, D08205, doi:10.1029/2004JD005350, 2005.

Fromm, M., Tupper, A., Rosenfeld, D., Servranckx, R., and McRae, R.: Violent pyro-convective storm devastates Australia's capital and pollutes the stratosphere, Geophys. Res. Lett., 33, L05815, doi:10.1029/2005GL025161, 2006.

Fromm, M. D. and Servranckx, R.: Transport of forest fire smoke above the tropopause by supercell convection, Geophys. Res. Lett., 30, 1542, doi:10.1029/2002GL016820, 2003.

Graf, H.-F., Herzog, M., Oberhuber, J. M., and Textor, C.: The effect of environmental conditions on volcanic plume rise, J. Geophys. Res., 104, 24 309–24 320, 1999.

Gunthe, S., Su, H., and Pöschl, U.: Aerosol- and updraft-limited regimes of CCN activation over blue and green oceans, in preparation, 2009a.

Gunthe, S. S., King, S. M., Rose, D., Chen, Q., Roldin, P., Farmer, D. K., Jimenez, J. L., Artaxo, P., Andreae, M. O., Martin, S. T., and Pöschl, U.: Cloud condensation nuclei in pristine tropical rainforest air of Amazonia: size-resolved measurements and modeling of atmospheric aerosol composition and CCN activity, Atmos. Chem. Phys. Discuss., 9, 3811–3870, 2009b.

Haywood, J. and Boucher, O.: Estimates of the direct and indirect radiative forcing due to tropospheric aerosols: A review, Rev. Geophys., 38, 513–543, 2000.

Hegg, D. A.: Dependence of marine stratocumulus formation on aerosols, Geophys. Res. Lett., 26, 1429–1432, 1999.

Herzog, M., Graf, H.-F., Textor, C., and Oberhuber, J. M.: The effect of phase changes of water on the development of volcanic plumes, J. Volcanol. Geotherm. Res, 87, 55–74, 1998.

Herzog, M., Oberhuber, J. M., and Graf, H.-F.: A Prognostic Turbulence Scheme for the Nonhydrostatic Plume Model ATHAM, J. Atmos. Sci., 60, 2783–2796, 2003.

Hjelmfelt, M. R., Farley, R. D., and Chen, P. C. S.: A preliminary numerical study into the effects of coal development on cloud and precipitation processes in the northern Great Plains, J. Appl. Meteorol., 17, 846–857, 1978.

Hudson, J. G.: Variability of the relationship between particle size and cloudnucleating ability, Geophys. Res. Lett., 34, doi:10.1029/2006GL028850, 2007.

IAPSAG: WMO/IUGG International Aerosol Precipitation Science Assessment Group (IAPSAG) Report: Aerosol Pollution Impact on Precipitation: A Scientific Review, World Meteorological Organisation. Geneva, 2007.

Janhäll, S., Andreae, M. O., and Pöschl, U.: Biomass burning aerosol emissions from wildfires: particle number and mass emission factors and size distributions, to be submitted, 2009.

Jiang, H. J., Wang, B., Goya, K., Hocke, K., Eckermann, S. D., Ma, J., Wu, D., and Read, W. G.: Geographical distribution and interseasonal variability of tropical deep convection: UARS MLS observations and analyses, J. Geophys. Res., 109, D03111, doi:10.1029/2003JD003756, 2004.

Johnson, B. T., Shine, K. P., and Forster, P. M.: The semi-direct aerosol effect: Impact of absorbing aerosols on marine stratocumulus, Q. J. R. Meteorol. Soc., 130, 1407–1422, 2004.

Kandler, K. and Schütz, L.: Climatology of the averagewater-soluble volume fraction of atmospheric aerosol, Atmos. Res., 83, 77 – 92, 2007.

Kessler, E.: On the distribution and continuity of water substances in atmospheric circulations, Meteor. Monogr. 32, Boston: Amer. Meteor. Soc., p. 88, 1969.

Khain, A., Rosenfeld, D., and Pokrovsky, A.: Aerosol impact on the dynamics and microphysics of deep convective clouds, Q. J. R. Meteorol. Soc., 131, 2639–2663, 2005.

Khain, A. P., BenMoshe, N., and Pokrovsky, A.: Factors determining the impact of aerosols on surface precipitation from clouds: An attempt at classification, J. Atmos. Sci., 65, 1721–1748, 2008.

Kivekas, N., Kerminen, V. M., Anttila, T., Korhonen, H., Lihavainen, H., Komppula, M., and Kulmala, M.: Parameterization of cloud droplet activation using a simplified treatment of the aerosol number size distribution, J. Geophys. Res., 113, doi:10.1029/2007JD009485, 2008.

Koren, I., Kaufman, Y. J., Rosenfeld, D., Remer, L. A., and Rudich, Y.: Aerosol invigoration and restructuring of Atlantic convective clouds, Geophys. Res. Lett., 32, L14828, doi:10.1029/2005GL023187, 2005.

Kreidenweis, S. M., Petters, M. D., and Chuang, P. Y.: Cloud particle precursors, in: Clouds in the perturbed climate system – their relationship to energy balance, atmospheric dynamics, and precipitation, edited by: J. Heintzenberg and R. J. Charlson, MIT Press, Cambridge, pp. 291–317, 2009.

Laaksonen, A., Vesala, T., Kulmala, M., Winkler, P. M., and Wagner, P. E.: Commentary on cloud modelling and the mass accommodation coefficient of water, Atmos. Chem. Phys., 5, 461–464, 2005.

Lance, S., Nenes, A., and Rissmann, T. A.: Chemical and dynamical effects on cloud droplet number: Implications for estimates of the aerososl indirect effect, J. Geophys. Res., 109, D22208, doi:10.1029/2004JD004596, 2004.

Lavoué, D., Liousse, C., Cachier, H., Stocks, B. J., and Goldammer, J. G.: Modeling of carbonaceous particles emitted by boreal and temperate wildfires at northern latitudes, J. Geophys. Res., 105, 26 871–26 890, 2000.

Liu, S., Hu, M., Wu, Z., Wehner, B., Wiedensohler, A., and Cheng, Y.: Aerosol number size distribution and new particle formation at a rural / costal site in Pear River Delta (PRD) of China, Atmos. Environ., 42, 6275–6283, 2009.

Lohmann, U. and Feichter, J.: Global indirect aerosol effects: a review, Atmos. Chem. Phys., 5, 715–737, 2005.

Luderer, G.: Modeling of Deep-Convective Transport of Forest Fire Smoke into the Upper Troposphere and Lower Stratosphere, Ph.D. thesis, University of Mainz, 2007.

Luderer, G., Trentmann, J., Winterrath, T., Textor, C., Herzog, M., Graf, H.-F., and Andreae, M. O.: Modeling of Biomass Smoke Injection into the Lower Stratosphere (Part II): Sensitivity Studies, Atmos. Chem. Phys., 6, 5261–5277, 2006.

Luderer, G., Trentmann, J., and Andreae, M. O.: The role of fire-released moisture on the dynamics of atmospheric pyro-convection, Int. J. Wildland Fire, 18, 554–562, 2009.

McFiggans, G., Artaxo, P., Baltensperger, U., Coe, H., Facchini, M. C., Feingold, G., Fuzzi, S., Gysel, M., Laaksonen, A., Lohmann, U., Mentel, T. F., Murphy, D. M., O'Dowd, C. D., Snider, J. R., and Weingartner, E.: The effect of physical and chemical aerosol properties on warm cloud droplet activation, Atmos. Chem. Phys., 6, 2006.

Mikhailov, E., Vlasenko, S., Martin, S. T., Koop, T., and Pöschl, U.: Amorphous and crystalline aerosol particles interacting with water vapour – Part 1: porous and gel-like microstructures, surface and bulk uptake, phase transitions, hygroscopic growth and kinetic limitations, Atmos. Chem. Phys., to be submitted, 2009.

Molina, L. T., Kolb, C. E., de Foy, B., Lamb, B. K., Brune, W. H., Jimenez, J. L., Ramos-Villegas, R., Sarmiento, J., Paramo-Figueroa, V. H., Cardenas, B., Gutierrez-Avedoy, V., and Molina, M. J.: Air quality in North America's most populous city; overview of the MCMA-2003 campaign, Atmos. Chem. Phys., 7, 2447–2473, 2007.

Mönkkönen, P., Koponen, I. K., Lethinen, K. E. J., Hämeri, K., Uma, R., and Kulmala, M.: Measurements in highly polluted Asian mega city: observations of aerosol number size distribution modal parameters and nucleation events, Atmos. Chem. Phys., 5, 57–66, 2005.

Muhlbauer, A. and Lohmann, U.: Aerosol-cloud-precipitation interactions in mixed-phase orographic clouds, submitted to J. Atmos. Sci., 2009.

Murphey, H. V., Wakimoto, R. M., Flamant, C., and Kingsmill, D. E.: Dryline on 19 June 2002 during IHOP. Part I: Airborne doppler and LEANDRE II analyses of the thin line structure and convection initiation, Mon. Wea. Rev., 134, 406–430, 2006.

Nenes, A., Ghan, S., Abdul-Razzak, H., Chuang, P. Y., and Seinfeld, J. H.: Kinetic limitations on cloud droplet formation and impact on cloud albedo, Tellus, 53B, 133–149, 2001.

Oberhuber, J. M., Herzog, M., Graf, H.-F., and Schwanke, K.: Volcanic plume simulation on large scales, J. Volcanol. Geotherm. Res, 87, 29–53, 1998.

Penner, J. E., Haselman, Jr., L. C., and Edwards, L. L.: Smoke-Plume Distribution above Large-Scale Fires: Implications for Simulations of "Nuclear Winter", J. Climate and Appl. Meteorol., 25, 1434–1444, 1986.

Penner, J. E., Dong, X., and Chen, Y.: Observational evidence of a change in radiative forcing due to the indirect aerosol effect, Nature, 427, 231–234, 2004.

Petch, J. C., Blossey, P. N., and Bretherton, C. S.: Differences in the lower troposphere in two- and three-dimensional cloud-resolving model simulations of deep convection, Q. J. R. Meteorol. Soc., 134, 1941–1946, 2008.

Petters, M. D. and Kreidenweis, S. M.: A single parameter representation of hygroscopic growth and cloud condensation nucleus activity, Atmos. Chem. Phys., 7, 1961–1971, 2007.

Pinsky, M., Khain, A., and Shapiro, M.: Collision efficiency of drops in a wide range of reynolds numbers: Effects of pressure on sprectrum evolution, J. Atmos. Sci., 58, 742–764, 2001.

Pöschl, U., Rudich, Y., and Amman, M.: Kinetic model framework for aerosol and cloud surface chemistry and gas-particle interactions – Part 1: General equations, parameters, and terminology, Atmos. Chem. Phys., 7, 5989–6023, 2007.

Pöschl, U., Rose, D., and Andreae, M. O.: Climatologies of cloud-related aerosols - Part 2: Particle hygroscopiciy and cloud condensation nucleus activity, in: Clouds in the perturbed climate system - their relationship to energy balance, atmospheric dynamics and precipitation, edited by Heintzenberg, J. and Charslon, R. J., MIT Press, Cambridge, pp. 57–72, 2009.

Potter, B. E.: The role of released moisture in the atmospheric dynamics associated with wildland fires, Int. J. Wildland Fire, 14, 77–84, 2005.

Pruppacher, H. R. and Klett, J. D.: Microphysics of Clouds and Precipitation, Kluwer Academics Publishers, 1997.

Ramanathan, V., Crutzen, P. J., Kiehl, J. T., and Rosenfeld, D.: Aerosols, Climate, and the Hydrological Cycle, Science, 294, 2119–2124, 2001a.

Ramanathan, V., Crutzen, P. J., and Lelieveld, J.: Indian Ocean Experiment: An integrated analysis of the climate forcing and effects of the great Indo-Asian haze, J. Geophys. Res., 106, 28 731–28 398, 2001b.

Reid, J. S., Koppmann, R., Eck, T. F., and Eleuterio, D. P.: A review of biomass burning emissions part II: intensive physical properties of biomass burning particles, Atmos. Chem. Phys., 5, 799–825, 2005.

Reutter, P., Trentmann, J., Su, H., Simmel, M., Rose, D., Wernli, H., Andreae, M. O., and Pöschl, U.: Aerosol- and updraft-limited regimes of cloud droplet formation: influence of particle number, size and hygroscopicity on the activation of cloud condensation nuclei (CCN), Atmos. Chem. Phys., 9, 7067—7080, 2009.

Rissmann, T. A., Nenes, A., and Seinfeld, J. H.: Chemical amplification (or dampening) if the Twomey effect: Conditions derived from droplet activation theory, J. Atmos. Sci., 61, 919–930, 2007.

Rose, D., Gunthe, S. S., Mikhailov, E., Frank, G. P., Dusek, U., Andreae, M. O., and Pöschl, U.: Calibration and measurement of a continuous-flow cloud condensation nuclei counter (DMT-CCNC): CCN activation of ammonium sulphate and sodium chloride aerosol particles in theory and experiment, Atmos. Chem. Phys., 8, 1153–1179, 2008a.

Rose, D., Nowak, A., Achtert, P., Wiedensohler, A., Hu, M., Shao, M., Zhang, Y., Andreae, M. O., and Pöschl, U.: Cloud condensation nuclei in polluted air and biomass burning smoke near the mega-city Guangzhou, China - Part 1: Size-resolved measurements and implications for the modeling of aerosol particle hygroscopicity and CCN activity, Atmos. Chem. Phys. Discuss., 8, 17 343–17 392, 2008b.

Rosenfeld, D.: Aerosols, clouds, and climate, Science, 312, 1429–1432, doi: 10.1126/science.1128972, 2006.

Rosenfeld, D. and Woodley, W. L.: Deep convective clouds with sustained supercooled liquid water down to −37.5°C, Nature, 405, 440–442, 2000.

Rosenfeld, D., Fromm, M., Trentmann, J., Luderer, G., Andreae, M. O., and Servranckx, R.: The Chisholm firestorm: observed microstructure, precipitation and lightning activity of a pyro-cumulonimbus, Atmos. Chem. Phys., 7, 645–659, 2007.

Rosenfeld, D., Lohmann, U., Raga, G. B., O'Dowd, C. D., Kulmala, M., Fuzzi, S., Reissell, A., and Andreae, M. O.: Flood or drought: How do aerosols affect precipitation?, Science, 321, 1309–1313, 2008.

Ruehl, C. R., Chuang, P. Y., and Nenes, A.: How quickly do cloud droplets form on atmospheric particles?, Atmos. Chem. Phys., 8, 1043–1055, 2008.

Segal, Y. and Khain, A.: Dependence of droplet concentration on aerosol conditions in different cloud types: Application to droplet concentration parameterization of aerosol conditions, J. Geophys. Res., 111, D15204, doi:10.1029/2005JD006561, 2006.

Seifert, A.: Parameterisierung wolkenmikrophysikalischer Prozesse und Simulation konvektiver Mischwolken, Ph.D. thesis, University of Karlsruhe, 2002.

Seifert, A. and Beheng, K. D.: A two-moment cloud microphysics parameterization for mixed-phase clouds. Part 1: Model description, Meteorol. Atmos. Phys., 92, 45–66, doi:10.1007/s00703-005-0112-4, 2006a.

Seifert, A. and Beheng, K. D.: A two-moment cloud microphysics parameterization for mixed-phase clouds. Part 2: Maritime vs. continental deep convective storms, Meteorol. Atmos. Phys., 92, 67–82, doi:10.1007/s00703-005-0113-3, 2006b.

Seinfeld, J. H. and Pandis, S. N.: Atmospheric Chemistry and Physics: From Air Pollution to Climate Change, John Wilsey & Sons, Inc., 2006.

Simmel, M. and Wurzler, S.: Condensation and activation in sectional cloud microphysical models, Atmos. Res., 80, 218–236, 2006.

Simmel, M., Trautmann, T., and Tetzlaff, G.: Numerical solution of the stochastic collection equation - comparison of the Linear Discrete Method with other methods, Atmos. Res., 61, 135–148, 2002.

Solomon, S., Qin, D., Manning, M., Chen, Z., Marquis, M., Averyt, K., Tignor, M., and Miller, H. L., eds.: Climate Change 2007: The Physical Science Basis. Contribution of Working Group I to the Fourth Assessment Report of the Intergovernmental Panel on Climate Change, Cambridge University Press, Cambridge, United Kingdom and New York, NY, USA, 2007.

Su, H., Reutter, P., Trentmann, J., Rose, D., Gunthe, S., Simmel, M., Nowak, A., Wiedensohler, A., Achtert, P., Hu, M., Shao, M., Zhang, Y. H., Zhu, T., and Pöschl, U.: Cloud parcel modelling of CCN activation in megacity air based on observations from Beijing, Geophysical Research Abstracts, Vol. 11, EGU2009-0, 2009.

Tao, W., Li, X., Khain, A., Matsui, T., Lang, S., and Simpson, J.: Role of atmospheric aerosol concentration on deep convective precipitation: Cloud-resolving model simulations, J. Geophys. Res., 112, doi:10.1029/2007JD008728, 2007.

Textor, C.: Numerical Simulation of scavenging processes in explosive volcanic eruption clouds, Ph.D. thesis, University Hamburg, 1999.

Textor, C., Graf, H.-F., Herzog, M., and Oberhuber, J. M.: Injection of gases into the stratosphere by explosive volcanic eruptions, J. Geophys. Res., 108, 4606, doi: 10.1029/2002JD002987, 2003.

Textor, C., Graf, H. F., Herzog, M., Oberhuber, J. M., Rose, W. I., and Ernst, G. G. J.: Volcanic particle aggregation in explosive eruption columns. Part I: Parameterization of the microphysics of hydrometeors and ash, J. Volcanol. Geotherm. Res, 150, 359–377, 2006.

Trentmann, J., Luderer, G., Winterrath, T., Fromm, M. D., Servranckx, R., Textor, C., Herzog, M., Graf, H.-F., and Andreae, M. O.: Modeling of Biomass Smoke Injection into the Lower Stratosphere (Part I): Reference Simulation, Atmos. Chem. Phys., 6, 5247–5260, 2006.

Twomey, S.: Atmospheric Aerosols, Elsevier Scientific Pub., p. 320pp, 1977.

Wallace, J. M. and Hobbs, P. V.: Atmospheric Science: an introductory survey, Elsevier Inc., 2006.

Wang, C.: A modeling study of the response of tropical deep convection to the increase of cloud condensation nuclei concentration: 1. Dynamics and microphysics, J. Geophys. Res., 110, D21211, doi:10.1029/2004JD005720, 2005.

Wang, P. K.: Moisture plumes above thunderstorm anvils and their contributions cross-tropopause transport of water vapor in midlatitudes, J. Geophys. Res., 108, 4194, doi:10.1029/2002JD002581, 2003.

Ward, R. D.: Cumulus clouds over a fire, Mon. Wea. Rev., 26, 104 – 105, 1898.

Wiedensohler, A., Cheng, Y. F., Nowak, A., Wehner, B., Achtert, P., Berghof, M., Birmili, W., Wu, Z. J., Hu, M., Zhu, T., Takegawa, N., Kita, K., Kondo, Y., Lou, S. R., Hofzumahaus, A., Holland, F., Wahner, A., Gunthe, S. S., Rose, D., and Pöschl, U.: Rapid Aerosol Particle Growth and Increase of Cloud Condensation Nucleus (CCN) Activity by Secondary Aerosol Formation: a Case Study for Regional Air Pollution in North Eastern China,, J. Geophys. Res., accepted, 2009.

Zhang, Y. H., Hu, M., Zhong, L. J., Wiedensohler, A., Liu, S. C., Andreae, M. O., Wang, W., and Fan, S. J.: Regional integrated experiments on air quality over Pear River delta 2004 (PRIDE-PRD2004): Overview, Atmos. Environ., 42, 6157–6173, 2008.